Alma Mater Studiorum – Università di Bologna

DOTTORATO DI RICERCA IN

CHIMICA

Ciclo XXVIII

Settore Concorsuale di afferenza: 03/B1

Settore Scientifico disciplinare: CHIM/03

Implantable Organic Transistors on Biodegradable Scaffolds for the Treatment of the Spinal Cord Injury

Presentata da: Alessandra Campana

Coordinatore Dottorato
Prof. Aldo Roda

Relatore
Prof. Francesco Zerbetto

Co-Relatori

Prof. Fabio Biscarini
Dr. Tobias Cramer

Esame finale anno 2016

Table of Contents

Table of Contents I

Keywords V

List of abbreviations VII

-Chapter 1 Spinal Cord Injury 1

1.1 Introduction 2
1.2 Spinal Cord Anatomy 2
1.3 Spinal Cord Injury 5
1.4 SCI Conventional and Experimental Treatments 9
1.4.1 Spinal Cord Plasticity 9
1.5 Electrical Stimulation and SCI 10
Bibliography 16

-Chapter 2 Methods, Devices and Materials 21

2.1 Introduction 22
2.2 Basic Concepts of Extracellular Recording and Stimulation 23
2.2.1 Electrode/Electrolyte/Cell interfaces 25
2.3 Multi (or Micro) Electrodes Arrays (MEAs) 28
2.4 Organic Field Effect Transistors (OFETs) 30
2.4.1 What an OFET is 31
2.4.2 How an OFET works 32
2.4.3 Current Voltage Characteristics 34
2.4.4 Electrical Characterization and Transport Parameters Extraction 35
2.4.5 OFETs as Interfacial Sensors Devices 37
2.5 OFETs in Water 39
2.5.1 Electrolyte Gated OFETs 39
2.5.2 EGOFETs as Biosensors
2.6 Implantable devices 46
2.6.1 Foreign Body Reaction 46
2.6.2 Materials 49
2.7 The i-ONE Project and the Scope of the Thesis 51
Bibliography 54

-Chapter 3 Electrolyte Gated Field Effect Transistors on Biodegradable substrate: a Facile Maskless Fabrication 61

3.1 Introduction 62
3.2 Laser Ablation Protocol: EGOFET on Quartz 63
3.2.1 EGOFET on Quartz: Electrical Performances 66
3.3 Laser Ablation onto Soft Scaffold: EGOFET on PLGA 67
3.3.1 EGOFET onto PLGA: Electrical Performances 69
3.4 Conclusions on EGOFET by Direct Fabrication 71
3.5 EGOFET on PLGA by Inverse Fabrication 72
3.5.1 EGOFET on PLGA by IF: Electrical Characterization 76
3.6 Conclusions on EGOFET on PLGA by IF 77
Bibliography 78

-Chapter 4 Organic Electrochemical Transistor Fabricated on Biodegradable Scaffold: Electrocardiographic Recording 81

4.1 Introduction 82
4.2 Easy Fabrication of an OECT on PLGA 82
4.3 OECTs fabricated on PLGA: electrical performances 84
4.4 ECG Recording by means of an OECT on PLGA 87
4.5 Conclusions 89
Bibliography 90

-Chapter 5 *In vitro* Extracellular Electrical Stimulation with Biodegradable OECTs 91

5.1 Introduction 92
5.2 Experimental Section 94
5.2.1 Fabrication of the Stimulating OECTs 94
5.2.2 Device Holder 95
5.2.3 Setup: Microscope, SMU and Software 96
5.2.4 Stimulation Protocols 99
5.3 ES Activity onto Primary Neurons 101
5.3.1 Primary Neurons Culturing 101
5.3.2 Results and Discussions 103
5.3.3 Conclusions 111
5.4 ES Activity onto Reactive Macrophages 113
5.4.1 Macrophages Culturing 114
5.4.2 Results and Discussions 115
5.4.3 Conclusions 117
Bibliography 118

-Chapter 6 Fabrication and Characterization of the implantable device 121

6.1 Introduction 122
6.2 Experimental Section 124
6.2.1 AMID Fabrication Strategy 126
6.2.2 AMID Electrical Characterization 137
6.2.3 Stimulation Protocol 139
6.3 Conclusions 140
Bibliography 141

-Chapter 7 In vivo Acute Stimulation and Subacute AMID Integration 143

7.1 In vivo Electrical Stimulation in Acute: an Introduction 144
7.1.1 Stimulation of the Rat SC in Acute, Experimental Section 148
7.1.2 Conclusions Part I 154
7.2 In vivo Subacute AMID Integration: an Introduction 155
7.2.1 Subacute AMID Implantation on Rats, Experimental Section 156
7.2.2 Conclusions Part II 160
Bibliography 161

-Chapter 8 General Conclusions 163

List of publications a

Acknowledgments d

Keywords:

Spinal Cord Injury

Biocompatible

Biodegradable

Implantable

Organic Field Effect Transistors

Organic Bioelectronics

List of abbreviations:

AFM: Atomic Force Microscopy
AMID: Active Multifunctional Implantable Device
AP: Action Potential
APTES: (3-aminopropyl)-trietoxysilane
BMS: Basso Mouse Scale
BSB: Blood-Spinal Cord Barrier
CAD: Computer-Aided Design
CNS: Central Nervous System
CPG: Central Pattern Generator
CSF: Cerebrospinal Fluid
DH: Device Holder
ECG: Electrocardiogram
EDL: Electrical Double Layer
EES: Epidural Electrical Stimulation
EGOFET: Electrolyte Gated Organic Field Effect Transistor
EMG: Electromyography
ENG: Electroneurography
eEMC: Electrically Enabled Motor Control
ER: Early Response
ES: Electrical Stimulation
FBR: Foreign Body Reaction
FDA: Food and Drug Administration
FES: Functional Electrical Stimulation
FET: Field Effect Transistor
GUI: General User Interface
GM: Gastrocnemius Medialis
IF: Inverse Fabrication
IHP: Inner Helmholtz Plane
I-One: Implantable Organic Nano Electronics
ISS: Intraspinal Stimulation
LFP: Local Field Potential
LR: Late Response
MN: Motoneuron
MOSFET: Metal Oxide Semiconductor Field Effect Transistor
MEA: Micro (or Multi) Electrode Array

mlR: Medium Latency Response
MP: Macrophage
MPX: Multiplexer
MR: Medium Response
MUX: Multiplexer
NP: Neuroprostheses
NPC: Neural Progenitor Cells
OECT: Organic Electrochemical Transistor
OFET: Organic Field Effect Transistor
OHP: Outer Helmholtz Plane
PAA: Poly(acrylicacid)
PBS: Phosphate Buffer Solution
PCR: Polymerase Chain Reaction
PEDOT:PSS: (poly(3,4-ethylenedioxythiophene) polystyrene sulfonate
PDMS: Polydimethylsiloxane
PI: Polyimide
PI: Propidium Iodide
PLGA: poly(lactic-co-glycolic) acid
PNS: Peripheral Nervous System
Silquest: 3-glycidoxypropyltrimethoxysilane
SC: Spinal Cord
SCI: Spinal Cord Injury
SCS: Spinal Cord Stimulation
slR: Short Latency Response
SMU: Source Measure Unit
SN: Sciatic Nerve
TA: Tibialis Anterior
TP: Test Pattern
VGCC: Voltage Gated Calcium Channel
VGIC: Voltage Gated Ion Channel
VGSC: Voltage Gated Sodium Channel
ZIF: Zero Insertion Force

chapter 1

Spinal Cord Injury

In this first chapter the spinal cord anatomy is described and spinal cord injury pathology introduced. The main physiological processes are described and an overview of the current therapies is given. The openings provided by the usage of electrical stimuli towards functional recovery of spinal cord activity are described.

1.1 Introduction

Spinal Cord Injury (SCI) is a severe insult of the spinal cord (SC). It can be caused by traumatic or non-traumatic events. Sport injuries, automobile or motorcycle accidents and falls are common causes of traumatic SCI. Very often fragments of bone or vertebrae tear into the SC and disrupt the network of nerves that carriers signals through the body. However, some diseases (e.g. cancer, arthritis, osteoporosis) can cause non-traumatic SCI. SCI results in a loss or impaired function causing reduced mobility or feeling. It is a devastating and debilitating condition affecting 2.5 million people worldwide, with more than 130,000 new cases reported each year[1]. The average age of injury is 33. SCI has a significant impact on quality of life, life expectancy and economic burden, with considerable costs associated with primary care and loss of income.

Considerable financial support to the research for SCI has been given in the past years. Several experimental regenerative therapies have been recently developed. However, none of these approaches provides full recovery in experimental injury models as well as in humans. In order to discuss classical and unconventional therapies and to set the basements on which the current PhD thesis was developed, a description of the anatomy of the SC and the relevant aspects about SCI are given.

1.2 Spinal Cord Anatomy

SC composes, with the brain, the central nervous system (CNS). It is the responsible of the bidirectional communication between the brain and the peripheral nervous system (PNS). It conducts sensory information from the PNS to the brain and motor information from the brain towards the PNS, which drives muscle and organs. SC also coordinates some reflexes. It is a tubular bundle of nervous tissue and support cells. It starts from the caudal end of the hindbrain to the lower part of the vertebral

column and its total length, in humans, ranges between 40 and 50 cm. The spinal cord runs within the vertebral bones and it is much shorter if compared to the total length of the vertebral column. Vertebrae are thirty-three in humans: first twenty-four are articulated and separated by intervertebral discs and the lower nine are fused, five in the sacrum and four in the coccyx. An easy way to identify the positioning is the numbering according to their region of the spine: seven are cervical, twelve are thoracic and five are lumbar. A second enumeration considers the thirty-one segments of the spinal cord with eight cervical (C1-C8), twelve thoracic (T1-T12), five lumbar (L1-L5) and one coccygeal (Co1) vertebra. Experimentation is often performed on rodents (i.e. mice and rats) that represent a reliable animal model. However, the anatomy of the SC differs in terms of number of vertebrae (from twenty-five to thirty) and caudal vertebrae (that are twenty-six). SC is composed of thirty-four segments: eight cervical (C1-C8), thirteen thoracic (T1-T13), six lumbar (L1-L6), four sacral (S1-S4) and 3 coccygeal (Co1-Co3). Three layers of tissue or membranes, generally referred as meninges, protect the SC. The dura mater is the outermost layer and it acts as a robust protective coating. The space between the vertebra and the dura mater is called epidural space. It is filled with adipose tissue and it contains a network of blood vessels. A middle protective layer is called *arachnoid mater* and it is separated by the subarachnoid space from the underlying *pia mater*. Cerebrospinal fluid (CSF) is contained in the subarachnoid space. The *pia mater* is the innermost of the meninges, it is a vascular membrane and it is tightly associated with the surface of the SC. The cross-section (**Figure 1**) view of the SC allows the identification of the peripheral region of the cord containing neuronal white matter tracts. It is where sensory and motor neurons are located. The grey matter has a butterfly shape and contains neurons cell bodies. It is inside the white matter and surrounds the central canal that contains CSF. The SC has an elliptical shape, compressed along the dorso-ventral axis. The cord has grooves in the dorsal and ventral sides that serve as points where the ventral and dorsal

rootlets emerge from the cord and give rise to spinal nerves. Grey matter is divided into dorsal horns, ventral horns and lateral horns. Dorsal horns receive the afferent information, thus intending the information from the dorsal root, while the ventral horns contains motoneurons (MNs) that innervate the skeletal muscles through the ventral roots. Lateral horns are found in the thoracic and upper lumbar segments and contain autonomic cell bodies for the sympathetic nervous system innervation (unconscious actions). The dorsal roots contain afferent sensory fibres both myelinated and unmyelinated. Myelin is a fatty coating that surrounds the axon of some (myelinated) nerve cells forming an electrically insulating shield essential for the exploitation of their functionality. Neuron cell body is in the dorsal root ganglion (that is a nerve cell cluster) while each single axon split projecting one branch to the periphery and the other to the dorsal SC.

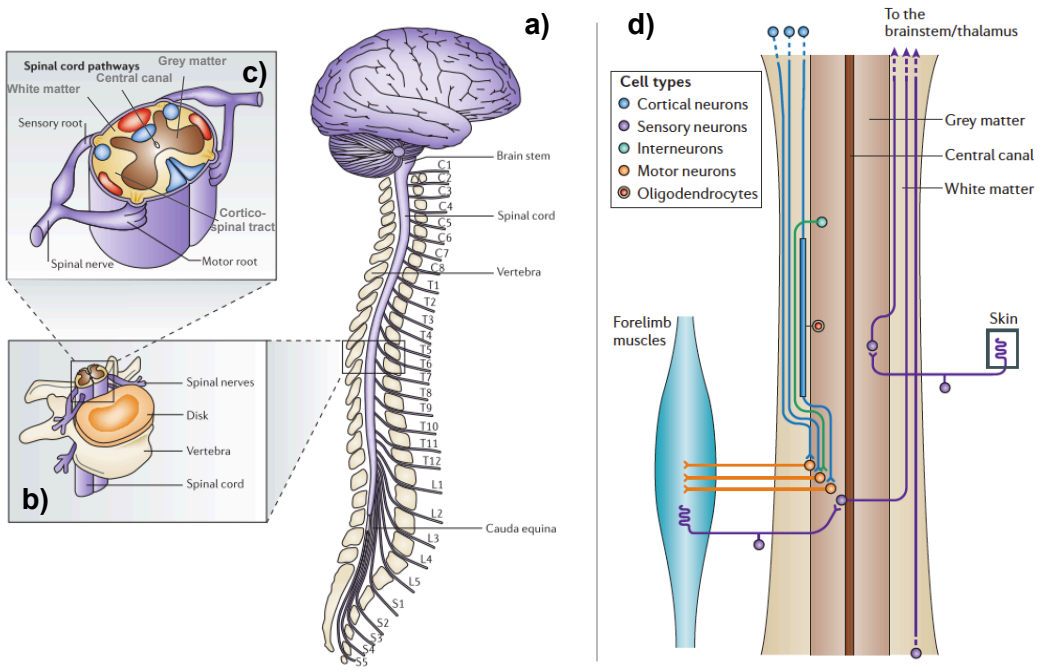

Figure 1 a) Reports a schematic showing a sagittal view through the human CNS. **b)** Schematic representation of a vertebral bone where SC in encased. **c)** Transverse section through human spinal cord. The main ascending pathways (which transmit sensory information to the brain) are indicated in red and the main descending pathways (which transmit motor information to the body) are

indicated in blue. **a**, **b** and **c** are adapted with permission from Ref. [2]. **d)** Scheme showing projections to motor neurons in spinal cord grey matter, which in turn send axons through the PNS to target organs, including muscles. Primary sensory neurons send axons through the PNS to second order sensory neurons in the CNS grey matter, which, in turn, send axons through white matter in the dorsal columns to supraspinal regions. Reprinted by permission from Ref. [3].

Primary afferent fibres are divided into four main subgroups: i) *Aα* (type I) are large and myelinated fibres carrying proprioception (related to the sense of position in space) information through muscles receptors; ii) *Aβ* (type II) are medium size myelinated fibres collecting information from stationery muscles; iii) *Aδ* (type III) are small myelinated fibres carrying nociceptive (e.g. thermal, mechanical) information; iv) *C fibres* (type IV) small non-myelinated fibres acting like *Aδ*.

Ventral roots contain mainly myelinated efferent somatic motor fibres from the ventral grey horns. Branches projected from the ventral and dorsal roots towards the lateral sides of the SC collectively form spinal nerves. White matter is divided into three regions, depending on their position, called dorsal, lateral and ventral funiculus. Myelinated fibres reside in the white matter funiculi and drive the information rostro-caudally thus regulating the ascending and descending path and bringing the commands from the cerebral cortex to voluntary movements, locomotors and posture control. Furthermore, SC contains neural circuits, called long and short descending propriospinal neurons that are interneurons dedicated to the interconnection of different SC segments for the coordination of complex movements.

1.3 Spinal Cord Injury

As already mentioned in the opening, SCI determines a partial or complete loss of sensory-motor functions caused by interruption of

ascending and descending fibers within the SC. The severity of the damage depends on lesion entity and spinal segments involved. SCI occurring between vertebral level C1 and T1 often implies tetraplegia that is the loss of sensorimotor below the head. If the injury occurs between T2 and S5 the disability involves the lower body and legs thus resulting in paraplegia.

Only in the last decades SCI become less lethal and, thanks to the emergency care and rehabilitation protocols, the survival rate is above 93%. However, life expectancy of SCI patients, depending of the severity and level of the injury, is lower and they are 2 to 5 times more likely to die prematurely than healthy people and they undergo severe complications.
SCI pathophysiology studies the functional changes resulting from the injury[4]. The events after the insult can be divided into two phases. The *primary* injury phase involves the mechanical disruption of the spinal column that results in an impact with the SC. This event can lead to axonal damage, cell death and laceration of the blood-spinal cord barrier (BSB). After few hours, *secondary* injury starts and various mechanisms are triggered that lead to aggravation. The understanding of all the single mechanisms is not complete but the study onto animal models[5] contributed to elucidate several aspects[4,6].

Within 0-2 hours after the injury, immediate death of neurons, glia (astrocytes, microglia and oligodendrocytes), vasospasm of the superficial vessels, intraparenchymal hemorrhage and swelling occur. Then, in the *acute phase* (2 hours – 2 weeks), ionic concentration fluctuations appear and accumulation of lipids and proteins, neurotransmitters, reactive oxygen species and ATP take place. Due to damages to the BSB and to the up-regulation of specific adhesion biomolecules, infiltration of immune cells (i.e. macrophages, lymphocytes and neutrophils) takes place. Immune cells release cytokines and interleukins and contribute to recruit monocytes that mature into pro-inflammatory activated macrophages, which release more pro-inflammatory cytokines that activate immune-like resident cells (i.e. microglia and astrocytes)[7]. Neutrophils and

microglia/macrophages are the main responsible for the inflammatory process. Their accumulation in specific necrosis areas where they contribute to re-establish homeostasis via phagocytosis of myelin and other cellular debris[7]. The cysts formation is the consequence of the necrotic tissue removal and prevents neuronal regeneration. Astrocyte reactivity can be promoted that lead (together with other factors) to the formation of a glial scar that serves to insulate the injury site and confine the inflammation. The *subacute phase* (2 weeks – 6 months) is characterized by a glial scar stabilization process that is induced by the infiltration of fibroblasts. Neurons not affected by direct injury can degenerate due to excitotoxicity (excessive stimulation by neurotransmitters) and other causes. Mechanisms leading to the demyelination and oligodendrocyte death are activated and the consequence is a strong inhibition of axons regeneration. BSB is repaired within 6 months. In this time scale, moderate spontaneous reorganization is observed and partial re-myelination is promoted. Modest rewiring (that generates unusual pathways) of the SC is based on the growth of axons from damaged ascending and descending neurons and from the propriospinal neurons. It occurs even though glial scar acts as a barrier to the regeneration process. Microglia/macrophages in this phase down-regulate the pro-inflammatory cytokines assuming an anti-inflammatory phenotype and contributing, by means of secretion of growth factor, to neurons protection and regeneration. However, all these efforts are very far to end with a complete functions restoration.

The complete stabilization of the damaged tissue represents the *chronic phase* and generally starts after the sixth month. A certain chronic inflammation level persists while neurological deficits stabilize with appearance of chronic pain.

Figure 2 reports the effects of the primary and secondary injury on the SC.

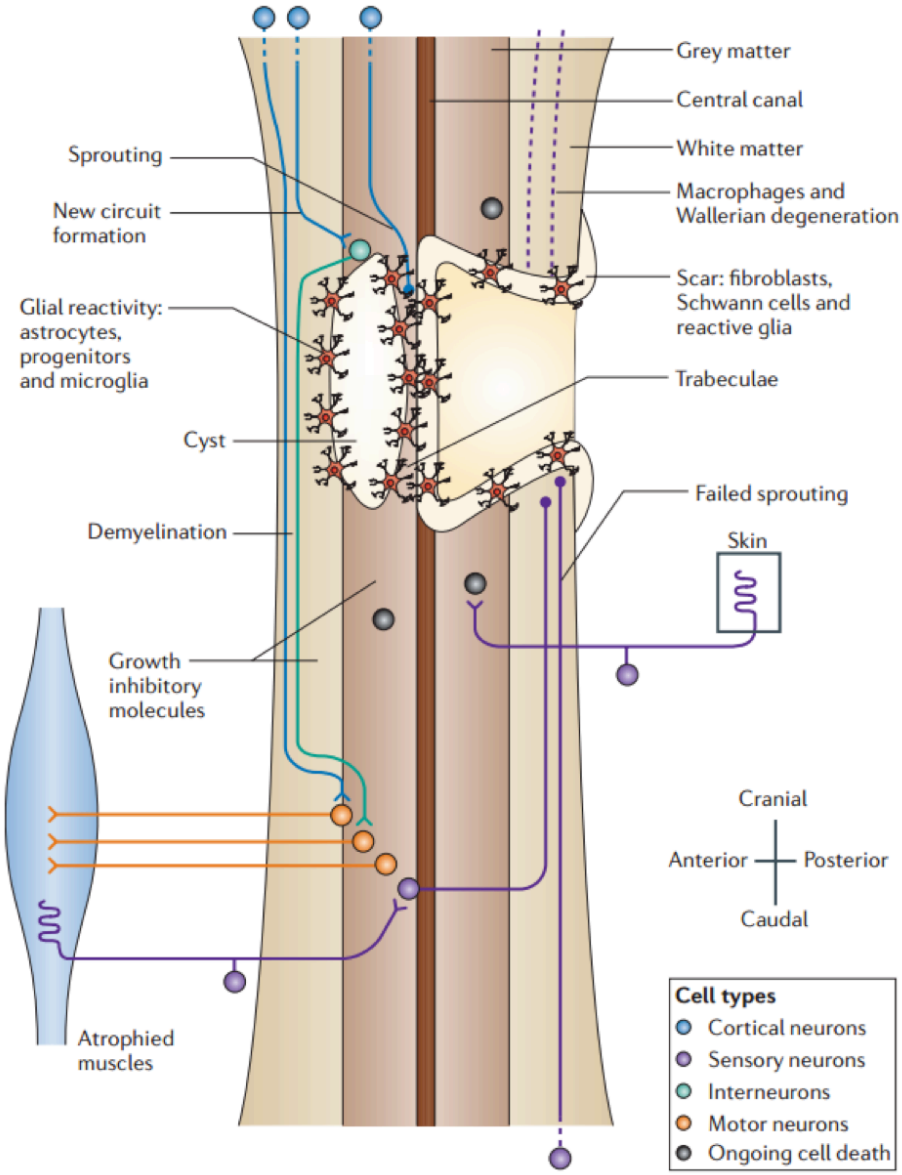

Figure 2 Schematic showing a sagittal view through a region of cervical spinal cord injury (SCI) depicting a combination of features from different types of injury. Many cells die immediately, as well as progressively, after SCI. Cysts usually form after contusion injury. After penetrating injury, cells from the PNS often invade the injury site to form a connective tissue scar that incorporates astrocytes, progenitor cells and microglia. Many ascending and descending axons are interrupted and fail to regenerate over long distances. Some axons form new circuits with motor neurons via interneurons. At the site of cyst formation, axons can sprout. Disconnected myelinated axon segments are phagocytosed by macrophages. Some spontaneous remyelination occurs. Reprinted by permission from Ref. [3].

1.4 SCI conventional and experimental treatments

Due to its pathophysiology complexity and to the singularity of each impact generating the injury[8], SCI is considered very difficult to be treated. Treatment options are limited but rehabilitation and experimental technologies have been found to help to maintain or improve remaining nerve functionality in some patients. Immediately after the insult occurred, immobilization of the spine is necessary in order to confine the lesion prior to surgical stabilization. A personalized rehabilitation program plays an important role in patients with incomplete injuries.

For an efficacious treatment is also necessary tailoring the needs of each phase. This means, for instance, usage of anti-inflammatory to reduce the pro-inflammatory microglia/macrophages spontaneous up-regulation in acute phase is recommended. In the subacute several experimental therapeutic approaches that are based on the assumption that CNS can, in principle, regenerate itself[9] are still under investigation. Among them it is worth mentioning i) the transplantation of stem cells to fill the gap created by the cysts and replace the neural cells loss due to the injury[10,11]; ii) local application of biomaterials scaffolds to drive regeneration[12,13]; iii) administration of growth factors specifically targeted to promote the axonal regeneration and inhibit adverse cues[2]. Even if promising, these therapies are still far from clinical trials.

1.4.1 Spinal cord plasticity

Research is recently focusing on the promotion of injury-induced adaptive changes of CNS. This phenomenon is called plasticity and the possibility of supporting it with dedicated therapies in order to push it further is very appealing. Spontaneous regeneration after SCI leads to a partial recovery[14]. It is supposed to be related to intraspinal and cortical tissue plasticity and sprouting mechanisms. Sprouting is widely observed

along the SC and also involves tracts necessary to exploit locomotors functions. Axonal tracts can run along unconventional circuits and are able to restore the access to segments previously insulated by the injury. The physiological process involves the replacement of the connection between the transected fibres and intraspinal neuronal tract close to the lesion. Then, a synaptic contact is formed between the intraspinal neuron and targeted cells of the transected fibre in order to establish a functional pathway[15]. Particularly prone to sprouting are propriospinal interneurons that can induce positive secondary effects onto locomotors and sensory functions. Among the high amount of examples in literature that report increasing of plasticity, the work of Courtine and co-workers (in the R. Edgerton lab) on mice worth to be mentioned. They reported mediation of spontaneous functional recovery by means of a diverted propriospinal connection. Furthermore, they observed this important plasticity effect onto totally transected descending pathways[16]. Intrinsic mechanisms driving plasticity are not fully elucidated yet. There are evidences about the important role played by sensory feedback[17] (and neuropathic pain[18]) for the spontaneous recovery and unconventional re-wiring. However, in order to achieve a functional synaptic contact, plasticity regeneration process has to be guided.

In order to maximise the efficacy of functional recovery after SCI, increasing the sprouting and plasticity of intact bridges is highly desirable as well as inducing reorganization of interactions between descending inputs and propriospinal circuits[16,19]. This could be enough to enable supraspinal control of lumbosacral circuits after severe SCI without the need of maintaining or regenerating the direct projections from the brain.

1.5 Electrical stimulation and SCI

Among the novel approaches investigated to improve the recovery after SCI, electrical stimulation (ES) is one of the most promising. In principle,

ES could be used to i) improve muscle functionality to maintain tonicity and promote locomotion (FES); ii) stimulate PNS to regulate specific functionalities and iii) apply direct stimulation to the SC (SCS) in order to activate locomotors functionalities. FES stimulates muscles with cutaneous patches, subcutaneous or implanted electrodes[20]. However, the most appealing approach to use ES is the SCS, which is born as an adjuvant in intervention for chronic back or leg pain[21]. In order to enable safe SCS, proper neuroprostheses (NPs) are necessary. NPs are specifically designed prostheses for the stimulation of central or peripheral nervous system. The field is attracting a great deal of attention and the possibilities of restoring health and of treating diseases by precise delivery of electrical pulses, electroceuticals, is becoming real[22]. Reclaim™ Deep Brain Stimulation for Obsessive Compulsive Disorder (OCD) therapy is one of the few basic examples of NPs devices recently approved by Food and Drug Administration (FDA). The usage of electric stimuli represents a great step towards the treatment of several diseases since it means speaking the language that body speaks. As it will be discuss along this thesis work, the fabrication and implantation of NPs set several requirements. Nowadays, more and more specifically performing devices are under investigation for the chronic implantation. However, the effects ES induces, as well as the hypothesis about the mechanisms, are studied in acute with non-implantable silicon based neural probes. Several laboratories reported about the efficacy of SCS in changing the physiological state of the SC circuits while inducing standing and stepping-like movements in animal models of SCI. SCS seems more promising than FES since it is able, with a proper designed implantable electrode array, to recruit and activate all the muscles involved in a specific movement. Secondary, SCS activates muscular fibres from spinal circuit, like a SC of healthy mammals does[23,24]. **Figure 3** shows some commercial and experimental NPs specifically dedicated to CNS and PNS.

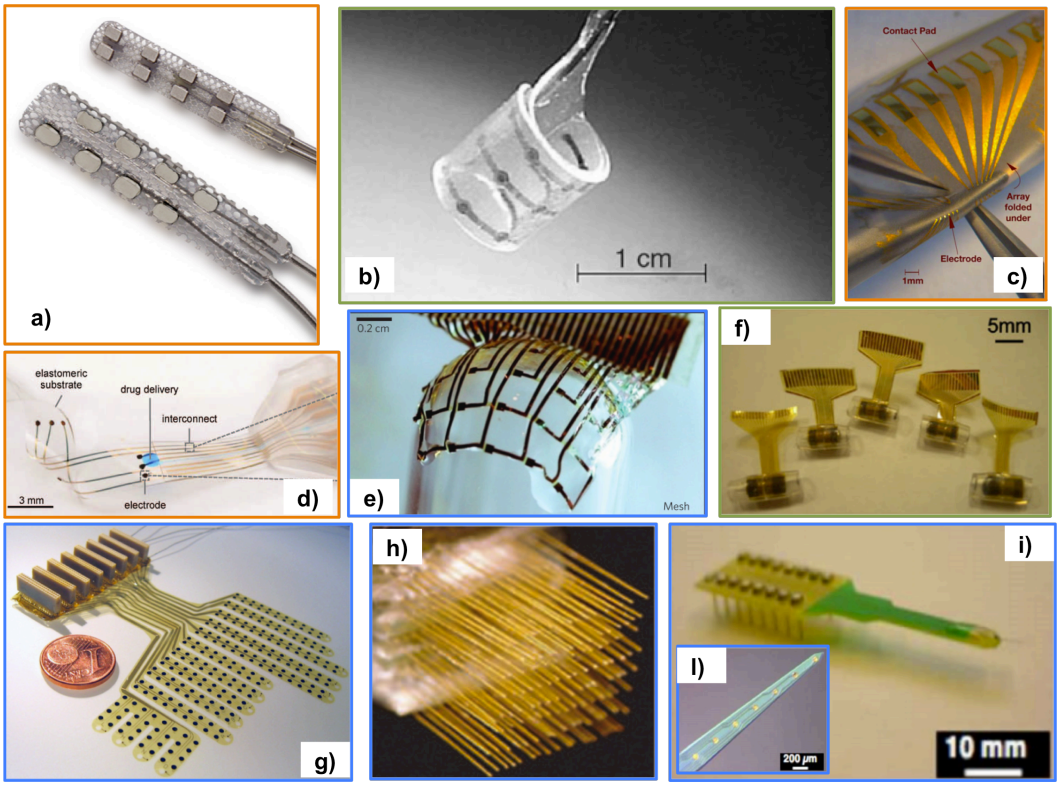

Figure 3 In this figure are reported few pictures about neuroprostheses found in literature. The different colours refer to different application, orange for spinal cord, blue for brain and green for PNS. **a)** Commercial device by Medtronic for the SCS. **b)** Polyimide based device for the stimulation and sensing from the PNS[25]. **c)** PDMS multi electrode array for SC surface stimulation[26]. **d)** *e-dura* is a stretchable multifunctional PDMS based device[27]. **e)** Silk fibroin/polyimide multi electrode array wet and wrapped onto a glass sphere for brain interface[28]. **f)** Rolled multi electrode arrays inserted in silicone tubes for interfacing sciatic nerve[29]. **g)** Layout of an electrocorticography array fabricated onto polyimide[30]. **h)** Teflon-coated stainless micro wires for brain interfacing[31]. **i)** and **l)** picture and magnification of silicon based gold/polypirrole nanotubes to be inserted in the motor cortex[32]. The figures are reprinted by permission from the relative references editors.

However, most important challenge of NPs for SCS is based on their activity in terms of stimulating plasticity to spontaneously reorganize residual descending connections towards the replacement of the ability of the SC to respond to electrical and chemical cues. These [33–36] are recent and very relevant findings which require a deeper discussion.

Edgerton's laboratory pioneered the studies about the relevance of the daily training and demonstrated it can improve functional capacities of cats SCI models[37,38]. Moreover, their findings revealed that specific training conditions the circuitry of a cat SCI model and induces full weight-bearing standing and stepping on a treadmill[39]. These results, obtained also with other animal SCI model [40], contributed to sustain the hypothesis that plasticity is somehow activity-dependant. Furthermore, it is now clear how repetitive activation of both synapses and sensory/motor pathways through specifically dedicated training can reshape the circuits and facilitate the performance of achieving a specific movement[41]. Interpretation and correlation of the general findings about SC of mammalian led to the assumption that supraspinal centres are fundamental only to provide inputs to initiate and terminate a specific movement. Indeed, signals originated from the brain activate the SC cervical and lumbar circuits called central pattern generators (CPGs) that control reflexes and are responsible for the generation of pattern and timing of coordinated and rhythmic muscular activities. Then, afferent sensory fibres adapt and modulate the guidelines of CPG to the environment to optimize the movement. Even though rehabilitation was demonstrated very successful in acute and chronic incomplete SCI patients, rehabilitation promoted functional recovery is not demonstrated successful in cases of severely affected SCI patients[42]. A good explanation about the differences observed between human and other mammals resides on the fact that human locomotors is more supraspinal dependent then other mammal locomotors system and its CPG results strongly depressed after complete SCI[43].

In order to increase SC excitability and to trigger increasing of activity-dependent plasticity[44], several strategies are currently under investigation that specifically target regeneration of CPGs: from pharmacological treatments to ES, both epidural (EES) and intraspinal (ISS). ES resulted very promising since it can induce action potentials

(APs) in the peripheral nerves activating circuits that are involved (in healthy SC) in bridging the information from the brain to the muscles and vice versa. ES effects are position dependent and, if specific fibres are activated, complex coordinated movements, like bilateral stepping, can be generated[45]. Actually, from Edgerton laboratories, the important observation that task-specific training with EES might reactivate previously silent spared neural circuits and promote plasticity in humans with severe SCI arrived[34]. It means activating some CPGs can restore supraspinal control. If the ES is associated to drugs therapy, i.e. injection of serotonergic agonists, and robotic arm interface (used to control the amount of hind limb body weight support) after complete SC transection in adult rats, the functionality of spinal network increased dramatically as early as one week after injury[44] (**Figure 4**). These results were obtained by using the ES as input for the generation of close-to-normal hind limb locomotors patterns in the absence of any supraspinal input.

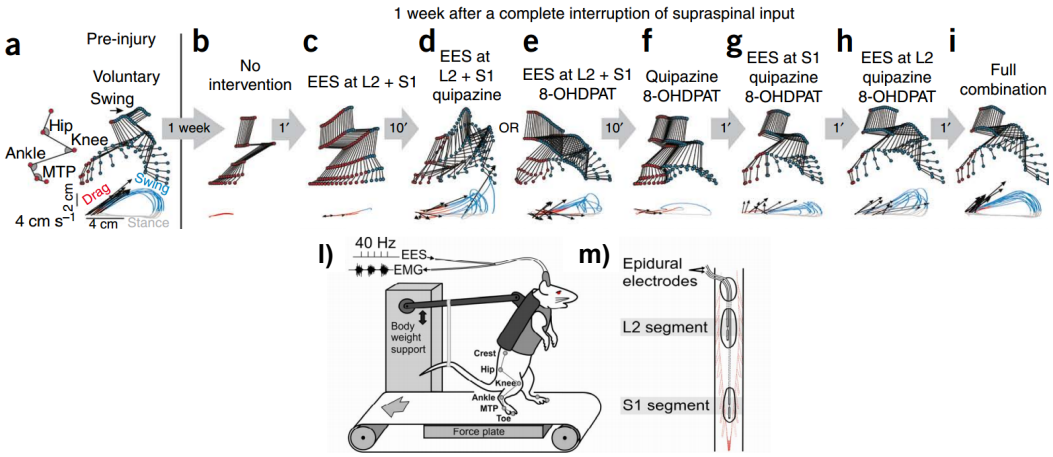

Figure 4 a)-i) Kinematic hind limb characteristics underlying locomotion recorded pre-injury **(a)** and 7-8 days post injury **(b)** without any intervention, as well as under various combinations of serotonergic agonists and/or EES **(c–i)**. The full combination **(i)** included quipazine, 8-OHDPAT and EES at L2 and S1. Recordings were performed sequentially in the same rat. Horizontal arrows indicate the chronology of the different recordings. A representative stick diagram decomposition of hind limb motion during swing is shown for each condition with successive color-coded trajectories of limb endpoint. Vectors

represent the direction and intensity of the limb endpoint velocity at swing onset. **l)** The animal is positioned in an upper body jacket that is attached to a robotic arm that measures and controls the amount of weight support. Intramuscular and epidural electrodes are routed sub-cutaneously to a percutaneous amphenol head connector, enabling the recording of electromiographic activity and the delivery of electrical stimulation chronically. **m)** Wires are routed below the spinous processes and sutured over the dura on the dorsal aspec t of L2 and S1 spinal segments. Reprinted by permission Ref. [44].

The mechanisms that govern ES induced neuronal plasticity are still under investigation. For sake of brevity and simplicity in the current thesis, the different formulated hypotheses are not reviewed. However, it worth to be mentioned that: i) *in vitro* experiments performed onto dorsal root ganglion demonstrated Ca^{2+} plays an important role in the regulation of neurite outgrowth[46]; ii) membrane depolarization induce a rapid transcription of BDNF (Brain-derived neurotrophic factor)[47], which is a protein that somehow encourages growth and differentiation of neurons and synapses; iii) both Ca^{2+} influx through voltage gated calcium channels (VGCCs) and Ca^{2+} mobilization from intracellular stores have to occur in order to obtain BDNF upregulation[48].

In conclusion, in this chapter SC, SCI and the standard medical therapies currently adopted were introduced. More importantly, was pointed out the great opportunity ES provides in order to promote functional recovery. However, most of the results described within this chapter were obtained with stranded stainless steel epidural electrodes or silicon chips. Organic Bioelectronics, by introducing low-invasiveness materials as well as novel architecture, can revolutionize the field. Details of the specific requirements and constraints set by ES and recording and interfacing biological tissues and electronics, that are the core of the current thesis, will be given in the Chapter 2.

Bibliography

(1) Adams, M.; Cavanagh, J. F. R. International Campaign for Cures of Spinal Cord Injury Paralysis (ICCP): Another Step Forward for Spinal Cord Injury Research. *Spinal cord Off. J. Int. Med. Soc. Paraplegia* **2004**, *42*, 273–280.

(2) Bradbury, E. J.; McMahon, S. B. Spinal Cord Repair Strategies: Why Do They Work? *Nat Rev Neurosci* **2006**, *7*, 644–653.

(3) Thuret, S.; Moon, L. D. F.; Gage, F. H. Therapeutic Interventions after Spinal Cord Injury. *Nat Rev Neurosci* **2006**, *7*, 628–643.

(4) Rowland, J. W.; Hawryluk, G. W. J.; Kwon, B.; Fehlings, M. G. Current Status of Acute Spinal Cord Injury Pathophysiology and Emerging Therapies: Promise on the Horizon. *Neurosurg. Focus* **2008**, *25*, E2.

(5) Zhang, N.; Fang, M.; Chen, H.; Gou, F.; Ding, M. Evaluation of Spinal Cord Injury Animal Models. *Neural Regen. Res.* **2014**, *9*, 2008–2012.

(6) Hagg, T.; Oudega, M. Neural Degeneration and Regeneration Myelin and Scar-Derived Inhibition. *J. Neurotrauma* **2006**, *23*, 264–280.

(7) Fleming, J. C.; Norenberg, M. D.; Ramsay, D. A.; Dekaban, G. A.; Marcillo, A. E.; Saenz, A. D.; Pasquale-Styles, M.; Dietrich, W. D.; Weaver, L. C. The Cellular Inflammatory Response in Human Spinal Cords after Injury. *Brain* **2006**, *129*, 3249–3269.

(8) Norenberg, M. D.; Smith, J.; Marcillo, A. The Pathology of Human Spinal Cord Injury: Defining the Problems. *J. Neurotrauma* **2004**, *21*, 429–440.

(9) David, S.; Aguayo, a J. Axonal Elongation into Peripheral Nervous System “Bridges” after Central Nervous System Injury in Adult Rats. *Science* **1981**, *214*, 931–933.

(10) Tewarie, R. S. N.; Hurtado, A.; Bartels, R. H.; Grotenhuis, A.; Oudega, M. Stem Cell – Based Therapies for Spinal Cord Injury. *J. Spinal Cord Med.* **2008**, *32*, 105–114.

(11) Martino, G.; Pluchino, S. The Therapeutic Potential of Neural Stem Cells. *Nat. Rev. Neurosci.* **2006**, *7*, 395–406.

(12) Straley, K. S.; Foo, C. W. P.; Heilshorn, S. C. Biomaterial Design Strategies for the Treatment of Spinal Cord Injuries. *J. Neurotrauma* **2010**, *27*, 1–19.

(13) Perale, G.; Rossi, F.; Sundstrom, E.; Bacchiega, S.; Masi, M.; Forloni, G.; Veglianese, P. Hydrogels in Spinal Cord Injury Repair Strategies. *ACS Chem. Neurosci.* **2011**, *2*, 336–345.

(14) Ballermann, M.; Fouad, K. Spontaneous Locomotor Recovery in Spinal Cord Injured Rats Is Accompanied by Anatomical Plasticity of Reticulospinal Fibers. *Eur. J. Neurosci.* **2006**, *23*, 1988–1996.

(15) Murray, M.; Goldberger, M. E. Restitution of Function and Collateral Sprouting in the Cat Spinal Cord: The Partially Hemisected Animal. *J. Comp. Neurol.* **1974**, *158*, 19–36.

(16) Courtine, G.; Song, B.; Roy, R. R.; Zhong, H.; Herrmann, J. E.; Ao, Y.; Qi, J.; Edgerton, V. R.; Sofroniew, M. V. Recovery of Supraspinal Control of Stepping via Indirect Propriospinal Relay Connections after Spinal Cord Injury. *Nat. Med.* **2008**, *14*, 69–74.

(17) Rossignol, S.; Dubuc, R.; Gossard, J.-P.; Dubuc, J. Dynamic Sensorimotor Interactions in Locomotion. *Physiol. Rev.* **2006**, *86*, 89–154.

(18) Christensen, M.; Hulsebosch, E. Chronic Central Pain after Spinal Cord Injury. *J. Neurotrauma* **1997**, *14*, 517–537.

(19) Bareyre, F. M.; Kerschensteiner, M.; Raineteau, O.; Mettenleiter, T. C.; Weinmann, O.; Schwab, M. E. The Injured Spinal Cord Spontaneously Forms a New Intraspinal Circuit in Adult Rats. *Nat. Neurosci.* **2004**, *7*, 269–277.

(20) Peckham, P. H.; Knutson, J. S. Functional Electrical Stimulation for Neuromuscular Applications. *Annu. Rev. Biomed. Eng.* **2005**, *7*, 327–360.

(21) Compton, A. K.; Shah, B.; Hayek, S. M. Spinal Cord Stimulation: A Review. *Curr. Pain Headache Rep.* **2012**, *16*, 35–42.

(22) Famm, K.; Litt, B.; Tracey, J. K.; Boyden, E. S.; Slaoui, M. A Jump-Start for Electroceuticals. *Nature* **2013**, *496*, 159–161.

(23) Guevremont, L.; Renzi, C. G.; Norton, J. A.; Kowalczewski, J.; Saigal, R.; Mushahwar, V. K. Locomotor-Related Networks in the Lumbosacral Enlargement of the Adult Spinal Cat: Activation through Intraspinal Microstimulation. *IEEE Trans. Neural Syst. Rehabil. Eng* **2006**, *14*, 266–272.

(24) Sharpe, A. N.; Jackson, A. Upper-Limb Muscle Responses to Epidural, Subdural and Intraspinal Stimulation of the Cervical Spinal Cord. *J. Neural Eng.* **2014**, *11*, 016005.

(25) Stieglitz, T.; Schuettler, M.; Koch, K. P. Implantable Biomedical Microsystems for Neural Prostheses. *IEEE Eng. Med. Biol. Mag.* **2005**, *24*, 58–65.

(26) Meacham, K. W.; Giuly, R. J.; Guo, L.; Hochman, S.; DeWeerth, S. P. A Lithographically-Patterned, Elastic Multi-Electrode Array for Surface Stimulation of the Spinal Cord. *Biomed. Microdevices* **2008**, *10*, 259–269.

(27) Minev, I. R.; Musienko, P.; Hirsch, A.; Barraud, Q.; Milekovic, T.; Asboth, L.; Torres, R. F.; Vachicouras, N. Electronic Dura Mater for Long-Term Multimodal Neural Interfaces. *Science.* **2015**, *347*, 159–163.

(28) Kim, D.-H.; Viventi, J.; Amsden, J. J.; Xiao, J.; Vigeland, L.; Kim, Y.-S.; Blanco, J. a; Panilaitis, B.; Frechette, E. S.; Contreras, D.; *et al.* Dissolvable Films of Silk Fibroin for Ultrathin Conformal Bio-Integrated Electronics. *Nat. Mater.* **2010**, *9*, 511–517.

(29) Lacour, S. P.; Benmerah, S.; Tarte, E.; Fitzgerald, J.; Serra, J.; McMahon, S.; Fawcett, J.; Graudejus, O.; Yu, Z.; Morrison, B. Flexible and Stretchable Micro-Electrodes for in Vitro and in Vivo Neural Interfaces. *Med. Biol. Eng. Comput.* **2010**, *48*, 945–954.

(30) Rubehn, B.; Bosman, C.; Oostenveld, R.; Fries, P.; Stieglitz, T. A MEMS-Based Flexible Multichannel ECoG-Electrode Array. *J. Neural Eng* **2009**, *6*, 36003–36010.

(31) Nicolelis, M. A. L.; Dimitrov, D.; Carmena, J. M.; Crist, R.; Lehew, G.; Kralik, J. D.; Wise, S. P. Chronic, Multisite, Multielectrode Recordings in Macaque Monkeys. *Proc. Natl. Acad. Sci. U. S. A.* **2003**, *100*, 11041–11046.

(32) Reza Abidan, M.; Martin, D. C. Experimental and Theoretical Characterization of Implantable Neural Microelectrodes Modified with Conducting Polymer Nanotubes. *Biomaterials* **2008**, *29*, 1273–1283.

(33) van den Brand, R.; Mignardot, J. B.; von Zitzewitz, J.; Le Goff, C.; Fumeaux, N.; Wagner, F.; Capogrosso, M.; Martin Moraud, E.; Micera, S.; Schurch, B.; *et al.* Neuroprosthetic Technologies to Augment the Impact of Neurorehabilitation after Spinal Cord Injury. *Ann. Phys. Rehabil. Med.* **2015**, *58*, 232–237.

(34) Harkema, S.; Gerasimenko, Y.; Hodes, J.; Burdick, J.; Angeli, C.; Chen, Y.; Ferreira, C.; Willhite, A.; Rejc, E.; Grossman, R. G.; *et al.* Effect of Epidural Stimulation of the Lumbosacral Spinal Cord on Voluntary Movement, Standing, and Assisted Stepping after Motor Complete Paraplegia: A Case Study. *Lancet* **2011**, *377*, 1938–1947.

(35) van den Brand, R.; Heutschi, J.; Barraud, Q.; DiGiovanna, J.; Bartholdi, K.; Huerlimann, M.; Friedli, L.; Vollenweider, I.; Moraud, E. M.; Duis, S.; *et al.* Restoring Voluntary Control of Locomotion after Paralyzing Spinal Cord Injury. *Science* **2012**, *336*, 1182–1185.

(36) Angeli, C. a.; Edgerton, V. R.; Gerasimenko, Y. P.; Harkema, S. J. Altering Spinal Cord Excitability Enables Voluntary Movements after Chronic Complete Paralysis in Humans. *Brain* **2014**, *137*, 1394–1409.

(37) De Leon, R. D.; Hodgson, J. a; Roy, R. R.; Edgerton, V. R. Full

Weight-Bearing Hindlimb Standing Following Stand Training in the Adult Spinal Cat. *J. Neurophysiol.* **1998**, *80*, 83–91.

(38) Tillakaratne, N. J. K.; Leon, R. D. De; Hoang, T. X.; Roy, R. R.; Edgerton, V. R.; Tobin, A. J. Use-Dependent Modulation of Inhibitory Capacity in the Feline Lumbar Spinal Cord. **2002**, *22*, 3130–3143.

(39) Rossignol, S.; Bouyer, L.; Barthélemy, D.; Langlet, C.; Leblond, H. Recovery of Locomotion in the Cat Following Spinal Cord Lesions. *Brain Res. Rev.* **2002**, *40*, 257–266.

(40) Edgerton, V. R.; Roy, R. R. Paralysis Recovery in Humans and Model Systems. *Curr. Opin. Neurobiol.* **2002**, *12*, 658–667.

(41) Edgerton, V. R.; Courtine, G.; Gerasimenko, Y. P.; Lavrov, I.; Ichiyama, R. M.; Fong, A. J.; Cai, L. L.; Otoshi, C. K.; Tillakaratne, N. J. K.; Burdick, J. W.; *et al.* Training Locomotor Networks. *Brain Res. Rev.* **2008**, *57*, 241–254.

(42) Dietz, V. Body Weight Supported Gait Training: From Laboratory to Clinical Setting. *Brain Res. Bull.* **2009**, *78*, I – VI.

(43) Courtine, G.; Van Den Brand, R.; Musienko, P. Spinal Cord Injury: Time to Move. *Lancet* **2011**, *377*, 1896–1898.

(44) Courtine, G.; Gerasimenko, Y.; van den Brand, R.; Yew, A.; Musienko, P.; Zhong, H.; Song, B.; Ao, Y.; Ichiyama, R. M.; Lavrov, I.; *et al.* Transformation of Nonfunctional Spinal Circuits into Functional States after the Loss of Brain Input. *Nat. Neurosci.* **2009**, *12*, 1333–1342.

(45) Gerasimenko, Y.; Roy, R. R.; Edgerton, V. R. Epidural Stimulation: Comparison of the Spinal Circuits That Generate and Control Locomotion in Rats, Cats and Humans. *Exp. Neurol.* **2008**, *209*, 417–425.

(46) Lankford, K. L.; Letourneau, P. C. Evidence That Calcium May Control Neurite Outgrowth by Regulating the Stability of Actin Filaments. *J. Cell Biol.* **1989**, *109*, 1229–1243.

(47) Tao, X.; Finkbeiner, S.; Arnold, D. B.; Shaywitz, A. J.; Greenberg, M. E. Ca2+ Influx Regulates BDNF Transcription by a CREB Family Transcription Factor-Dependent Mechanism. *Neuron* **1998**, *20*, 709–726.

(48) Kocsis, J. D.; Rand, M. N.; Lankford, K. L.; Waxman, S. G. Intracellular Calcium Mobilization and Neurite Outgrowth in Mammalian Neurons. *J. Neurobiol.* **1994**, *25*, 252–264.

chapter 2

Methods, devices and materials

This chapter focuses on methods to interface biological signals and to perform bidirectional communication with cells and living tissues. Requisites to achieve an efficient electrical stimulation and recording are reported. Then, an overview of the multi electrodes arrays and transistors for *in vitro* and *in vivo* application and their working principle is given. The requirements set by neuroprostheses implantation, like materials characteristics, are discussed. Finally, the scope of this thesis is presented.

2.1 Introduction

The first historical connection between electrodynamics field and biology dated back to 18th century. Luigi Galvani, Professor at University of Bologna, studied the effect of an electric stimuli applied to leg nerves of the frog[1], opening the field of the so-called “animal electricity” and laying down the foundation of electrophysiology. In the 20th century, 150 years later, the main step ahead was done, which led to modern electrophysiology: Alan Lloyd Hodgkin and Andrew Huxley modelled the action potential (AP) initiation and propagation in the squid’s giant axon[2]. The interest dramatically raised and novel glass microelectrodes were introduced which led to the development of the patch-clamp technique. Investigation of the current flow through single ion channels[3] was enabled and modern neuroscience was born. Patch-clamp is a powerful method that is particularly useful in the study of excitable cells such as neurons, cardiomyocytes and muscle fibres. It allowed the understanding of the involvement of ion channels in fundamental cell processes. The technique has become common in modern laboratories and still allows great breakthrough in neurosciences. Unfortunately, it has few strong limitations, which cannot be circumvented. First of all, investigation of more than few cells at the same time is not possible and dynamics of population are difficult to be resolved and understood. Furthermore, adaptation of standard patch clamp intracellular recording to non-invasive implantable devices is nowadays difficult to be envisioned. Extracellular recordings, on the contrary, circumvent the main obstacle and will enable, for instance, long-term monitoring of correlations between plasticity and learning[4]. The electrodes do not penetrate the cell membrane and characteristics detrimental to biocompatibility, such as sharpness and stiffness, are not required.

This chapter is dedicated to the principles of extracellular stimulation and recording of relevant bioelectric signals and to commercial and technologically advanced devices used for that purpose, in particular

MicroElectrode Arrays (MEAs) and Field Effect Transistors (FETs). Then, an overview about the relevance of materials properties is given.

2.2 Basics Concepts of Extracellular Recording and Stimulation

Three functional classes of neurons constitute peripheral neural circuits: afferent neurons (which carry information from the periphery toward the brain or spinal cord), efferent neurons (which carry information away from the brain or spinal cord) and inter-neurons (which possess short axons and only participate in local aspects). Afferent neurons can be considered sensory neurons, since they carry information from the sense organs to the brain while efferent neurons are often referred as motor neurons, since they control voluntary muscle activity. Neurons employ several different types of electrical signals to encode and transfer information. First of all, they have a means of generating a constant voltage across their membranes when at rest. This voltage, called the resting membrane potential, depends on the type of neuron being examined and ranges between -40 to -90 mV with respect to the potential of the extracellular space that is used as a reference. The electrical signals produced by neurons are caused by responses to stimuli, which then change the resting membrane potential. Although neurons and axons (neurons' slender projections) are both capable of passively conducting electricity, the electrical properties of neurons compare poorly to an ordinary electric wire. To compensate for this deficiency, neurons produce APs that allow them, despite their intrinsically poor electrical characteristics, to conduct electrical signals over great distances. The different concentration of ions on the two sides of the cellular membrane sets the neuron in a resting polarized state. When a passive current flows across the membrane, it induces a depolarization (**Figure 1**). If the depolarized membrane potential passes the threshold (about -48 mV), the

membrane potential is called highly depolarized and an AP is triggered. The AP results in a positive peak in the potential and its amplitude is not dependant on the initial depolarization. Thus, the intensity of the transmitted neural signal depends on the APs number, also referred as firing rate. Next, a strong repolarization follows this phenomenon to set the neuronal internal potential back at a negative level. In the hyperpolarization regime, which lasts for a few milliseconds, the potential is constant at more negative value. The time following the repolarization phase of the action potential is called *absolute refractory* period, where no APs can be generated. It is followed by a short *relative refractory* period during which AP can be generated but only with larger-than-normal depolarization. During the triggering of an AP, transmembrane voltage gated ion channels (VGICs) are involved. Ion channels are proteins that gate the ion flow through the cell membrane. These tunnels express selective permeability that allow only ions of a certain size and charge to pass across. However, some channels may be permeable to the passage of more than one type of ion, typically sharing a common charge. The gate opens or closes in response to specific electrical, chemical, thermal or mechanical stimuli.

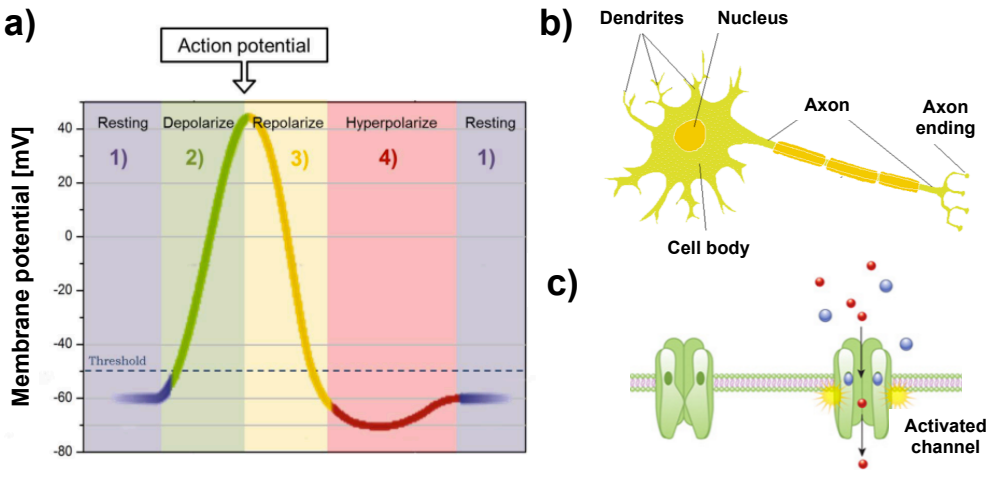

Figure 1 a) The graph represents the transmembrane potential during the steps of an AP. **b)** A scheme of a neuron is reported with the cell body and the axonal protrusion. **c)** Sketch of the transmembrane ion channels.

Depolarization decreases with distance. As a consequence, stimulation does not travel far but propagates down the axon to depolarize new pieces of the membrane. At the axon ending synapses establish connection with dendrites of the neighbour neuron on which AP is induced. Along dendrites, axons and synapses the neuronal signal propagates.

Extracellular field potential recordings, also referred to as local field potentials (LFPs), reflect the spike activity of neurons or the superposition of fast APs, synaptic potentials and slow glial potentials both in time and space[4]. During each AP, current flows and potential gradients are generated around the cell membrane. The usage of non-invasive electrodes for *in vitro* recordings and polytrodes for *in vivo* recordings attenuates and filter the detectability of the generated electrical signals. As a consequence of the high attenuation factor (1/100 to 1/1000), typically the amplitudes of LFPs range between 10 μV to 1 mV and sub-threshold potentials generated by individual neuron cannot be recorded[4]. Extracellular electrical stimulation of APs is also attenuated with respect the usage of intracellular electrodes.

Due to this strong attenuation, the knowledge of the interface between the electrode and the cell/tissue and the optimization of the devices become crucial to successfully achieve non-invasive extracellular stimulation and recording.

2.2.1 Electrode/Electrolyte/cell interfaces

This is probably the most important interface both for stimulation and for sensing in many different architectures and a proper modelling is necessary. Theoretically, there are two kinds of electrodes in terms of behaviour when biased at the interface with an electrolyte: i) perfectly *polarizable* electrodes do not allow transfer of charges across the

electrode-electrolyte interface and ii) perfectly *non-polarizable* electrodes that allow free exchange of charges across the interface. The properties of real electrodes lie between these theoretical limits and, for the modelling, electrochemists use an equivalent circuit made of a capacitor (purely polarizable) and a resistor (purely non-polarizable) in parallel (**Figure 2a**).

The purely polarizable electrode interface is very complex and of particular interest. Graham[5], rationalizing the former studies of von Helmholtz, Gouy, Chapman and Stern, firstly modelled it in the early '40. If the net charge on the electrode is forced to vary (as occurs during stimulation), charge in the electrolyte redistributes. In particular, when two electrodes are immersed in an electrolytic salt solution and a voltage source is applied across the two, one is driven to relatively negative and the other to relatively positive potentials. At the first electrode, positive charges (cations) in solution are attracted towards the interface that repels negative charges (anions) (**Figure 2b** shows a simplified scheme). In the interfacial region, there will be net electroneutrality, because the negative charge excess on the electrode surface will compensate the positive charge in solution near the interface. The bulk solution will also have net electroneutrality. At the second electrode, the opposite process occurs. Three different layers form starting from each of the two electrodes: i) the inner Helmholtz plane (IHP) is composed of bare ions and water molecules; ii) the outer Helmholtz plane (OHP) contains mainly water and hydrated ions and iii) the Gouy-Chapman layer (namely the bulk) where the remnant amount of charge is located. To simplify, at each electrode an electrical double layer (EDL) forms. The distance between the IHP and the electrode surface is always very small, on the order of few Å. Thus, the capacitance of the EDL is extremely high, in the range of 5 to 40 $\mu F/cm^2$. The current that flows in the circuit due to movement of ions towards the interface is called *displacement current*.

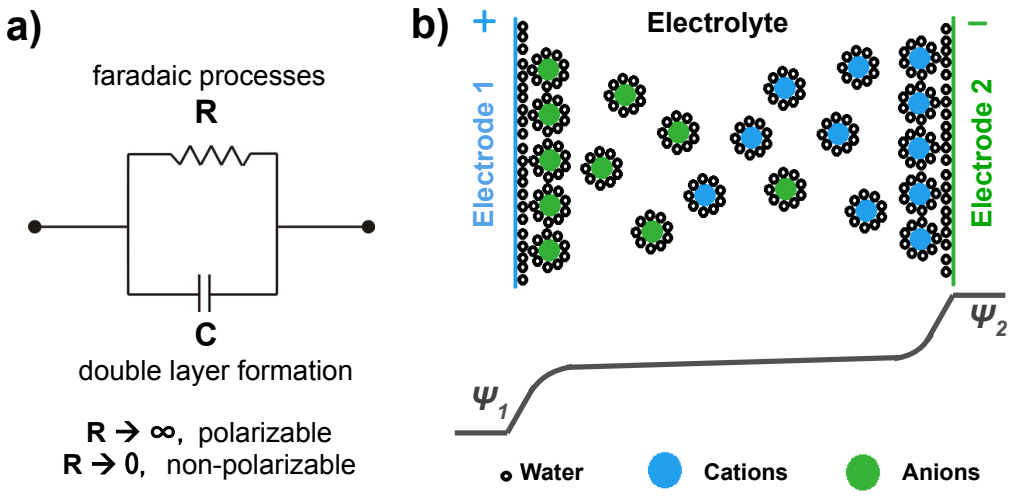

Figure 2 a) A simple equivalent RC circuit, which describes the electrode/electrolyte interface, is depicted. **b)** Simplified scheme of the electrical double layer formation and potential drop at the interfaces.

Since, mercury excluded, all electrodes are to a certain extent non-polarizable, the contribution of *faradaic current*, which is due to redox reactions at the electrode interface, has to be taken into account. Electrons are transferred between the electrode and chemical species into the electrolyte. Unlike the capacitive mechanism, faradaic charge injection forms products in solution that cannot be recovered upon reversing the direction of current if the products diffuse away from the electrode. Details of electrical stimulation from an electrochemical point of view are well reviewed in reference[6].

Both *in vitro* and *in vivo* an intimate contact is established between the surface electrode and the cells plated on top. Cleft is the term used to indicate the space, filled with ionic solution, which separates the electrode and the lower cell membrane, also called junctional membrane. Different compartments of the cell body adhere to the electrode by electrostatic or chemical interaction thanks to adhesion proteins that protrude from the lipid membrane. Typical cleft thickness range from 40 to 100 nm.

The maximal voltage recorded by the device in response to the maximal voltage generated by an excitable cell defines the cell/device electrical coupling. In order to maximize this parameter, one needs to maximize i) the cleft specific resistance, ii) the junction area and iii) the capacitive coupling while have to be minimized: i) the cleft thickness and ii) the electrode impedance. For an efficient electrical stimulation, charge-injection limit, that represents the maximum charge that can be injected into tissue without initiating irreversible faradaic reactions, has to be maximized as well as the specific capacitance[4,6–9].

2.3 Multi (or Micro) Electrodes Arrays (MEAs)

Multi (or Micro) Electrodes Arrays (MEAs) most appealing characteristic is decoding of communication across complex neural networks. Since the first extracellular approach to bidirectional communication, the usage of simple electrodes resulted attractive[10]. Then, progressively from the 50s to the 70s, the adaptation of new materials and fabrication strategies led to a growing interest in MEAs. Nowadays MEAs represent the state of the art in terms of extracellular stimulation and recording. The working principle is consolidated and applied to *in vitro* and *in vivo* electrophysiology and prosthetics devices. Standard active materials for MEAs are metals, such as gold or platinum, but also other conductive components including IrO_x or Indium Tin Oxide (ITO)[4]. Generally, to confine and reduce the electrode area, a passivation layer is used such as the epoxy based SU-8, polyimide or Si_4N_4. Various substrates are used depending on the final application. SiO_x is generally adopted as substrate while, when monitoring of cell activity or electrical stimulation is coupled to other techniques, which require transparency, glass or quartz are used. Towards the application *in vivo*, in the recent past, other materials were introduced which led to flexible and transparent MEAs made on polydimethylsiloxane (PDMS) or polyimide.

Like the scaffolds, the active layers can be replaced in order to increase the long-term biocompatibility. Conducting or semiconducting polymers have already been used as electrodes or electrode coatings. Furthermore, these polymers, like (poly(3,4-ethylenedioxythiophene), PEDOT, are capable of injecting much higher charge then standard metal electrodes and, due to the low impedance and to high ion-to-electron conversion capability, result in a high signal-to-noise recording both in vitro and in vivo[9,11]. **Figure 3** reports pictures of different MEAs.

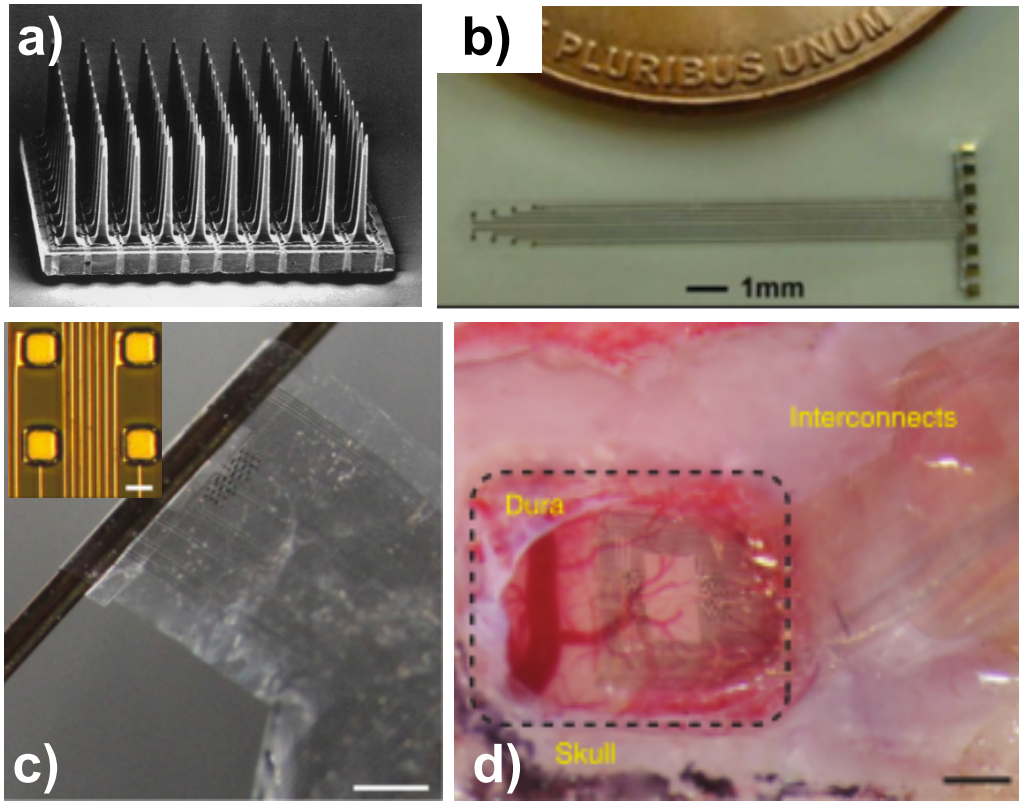

Figure 3 a) Scanning probe microscopy image of a typical protruding MEA (the Utah array). The platinum tip is exposed while the remnant part is insulated. Reprinted with permission from Ref [12]. **b)** A conformable parylene film with gold recording electrodes patterned on top. Reprinted with permission from Ref [13]. **c)** Picture of the 64 channel NeuroGrid (scale bar = 200 μm) conforming to a 100 μm diameter cylinder with an inset of the recording sites of a 256 channel NeuroGrid (scale bar = 10 μm) and d) the device conformed to the surface of the rat somatosensory cortex (scale bar, 1 mm). **c** and **d** are reprinted from Ref. [14].

The most relevant work reported towards the increasing of MEA biocompatibility was done by D. Khodagholy et al.[14]. They have fabricated a (poly(3,4-ethylenedioxythiophene):polystyrene sulfonate (PEDOT:PSS) based MEA onto a 4 μm thick parylene C film (**Figure 3 c** and **d**). Interconnect were made of gold and platinum. The metal leads do not directly interface tissues since they are embedded into the scaffold or covered by the semiconducting polymer. The device, called NeuroGrid, results in ultra conformable structure that can closely adhere to complex curvilinear surfaces. Recently, the possibility of increasing the sensitivity by increasing the junction area and the improvements in the fabrication strategies, led to the development of metal protruding electrodes[4].

2.4 Organic Field Effect Transistors (OFETs)

The field effect transistor (FET) was first theorized and then patented already in the twenties by J. E. Lilienfeld[15]. However it took until 1959 to realize similar device, the silicon-based Metal Oxide Semiconductor FET (MOSFET) by D. Kahng and M. J. Atalla[16]. MOSFET nowadays represents the most prominent constituent of microelectronic devices. The first organic semiconductors based electronic element was the metal-oxide-semiconductor capacitor demonstrated by F. Ebisawa, T. Kurokawa, and S. Nara at NTT 1982[17]. Only fours years later, the Organic Field Effect Transistor (OFET) with recognizable current gain based on in situ polymerized polythiophene was presented by A. Tsumura, H. Koezuka and T. Ando[18]. Technological and scientific reasons are the driving forces behind the rising interest about OFETs. Even if the potential improvement of organic based devices is strongly pursued[19], OFETs are still not commercially widespread due to long-term stability issue and not competitive performances.

2.4.1 What an OFET is

An OFET is a three terminal device where the current between the source (S) and drain (D) electrodes can be modulated through a voltage applied to the gate (G) electrode. The source and the drain electrodes are connected through a semiconducting material, which defines the transistor channel. The bias at gate electrode, separated from the channel by an electrically insulating material, governs the charge carriers in the semiconductor. The OFET can be viewed as a capacitor where one plate is represented by gate electrode and the other by the semiconducting channel. The last is geometrically defined by 3 main parameters: the width (W) of the faced source and drain electrodes, the distance that separates them, length (L) and the film thickness. The semiconducting layer in OFETs is usually sublimed or processed by solution (e.g: spin coating and drop casting) depending on the material characteristics. The gate is a metal (e.g.: gold and aluminium) or a conductive polymer but, very often, highly doped silicon serves as a gate electrode and substrate at once. The dielectric in standard configuration transistors is either polymeric or an oxide (thermally grown silicon or aluminium oxides).

The main architectures adopted in this thesis deviate from the standard OFET configuration. Nevertheless, a description of the working principles, characterization methods and parameters extraction in OFET is given since they undergo the same basic principles.

Depending on the position of the three electrodes with respect the semiconducting material, one can define three main different geometries. The **Figure 4** shows a scheme of these configurations defined as: bottom gate/bottom contacts (BGBC), tog gate/bottom contacts (TGBC) and bottom gate/top contacts (BGTC). To each one of them are related advantages and disadvantages, which are not described in this thesis.

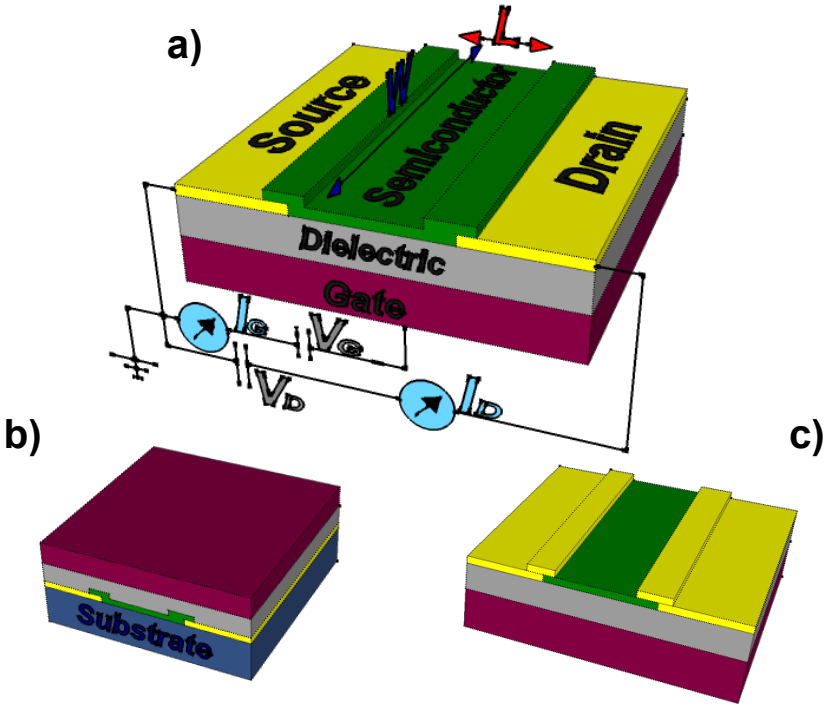

Figure 4 a) Schematic diagram of a BGBC OFET and its wiring diagram. L and W are the channel length and width. V_G and I_G are the bias and the current between the source and the gate while V_D and I_D are the bias and the current between the source and the drain. **b)** and **c)** report schemes of the TGBC and BGTC configurations respectively

2.4.2 How an OFET works

In the basic operation, the potentials are applied at the gate and at the drain while the source is kept grounded. The potential differences are generally referred as V_{GS} and V_{DS} or simply V_G and V_D. The source is the charge-injecting electrode since it is always more negative than the gate when a positive bias is applied ($V_G > 0$ V, electrons injection) and more positive then the gate ($V_D < 0$ V, holes injection).

Current-voltage characteristics display the basic operating regimes (**Figure 5**). First, we consider a simple metal-insulator-semiconductor (MIS) diode ($V_D = 0$ V, $V_G \neq 0$ V). If a positive gate voltage is applied,

negative charges (electrons) accumulate at insulator/semiconductor interface. On the contrary, when a negative potential is applied at the gate, positive charges (holes) are accumulated. The higher the potential applied, and the capacitance C_I of the insulator, the higher the number of charges accumulated. However, of all the accumulated charges, a portion only is mobile and will thus contribute to the I_D current of the OFET, since some of them are trapped. This results in the presence of a threshold voltage (V_{TH}) that has to be taken into account for the evaluation of the effective gate voltage, defined as $V_G - V_{TH}$. On the other hand, donor (for n-channel) or acceptor (p-channel) states and interface dipoles can generate an internal potential at the interface and thus cause accumulation of charges in the channel even if $V_G = 0$ V. In the last case, an opposite voltage has to be applied to turn the channel off.

When $V_D = 0$ V, in the transistor channel, the charge carrier concentration is uniform. As soon as a small V_D is applied, a linear gradient of charge density forms from the carrier-injecting source to the extracting drain electrode. This is called *linear regime* and the current flowing through the channel is directly proportional to V_{SD}. The potential V(x) within the channel increases linearly from the source (V(x=0) = 0 V) to the drain where it corresponds to $V(L) = V_D$ (**Figure 5a**).

The channel is pinched off when V_{SD} is further increased until the value corresponding to $V_G - V_{TH}$ is attained (**Figure 5b**). In these conditions, a depletion region is formed next to the drain because the difference between the local potential V(x) and V_G is below the $V_{TH.}$ A space charge limited saturation current, I_D, flows across a narrow depletion region since the carriers move from the pinch off point to the drain electrode. When the V_D is further increased, the depletion region expands and the channel results shortened. I_D in these conditions does not sensitively increase. This is called *saturation regime* (**Figure 5c**).

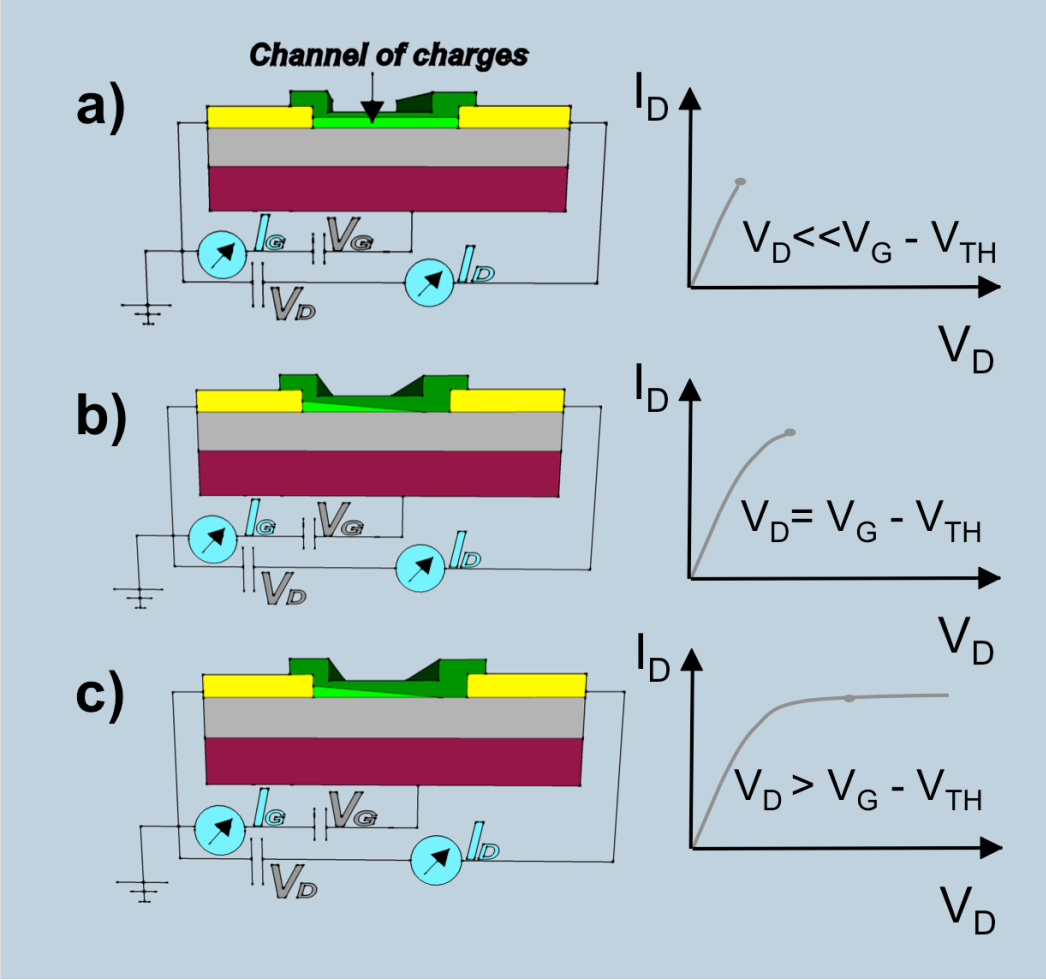

Figure 5 Illustrations of operating regimes of an OFET: **a)** linear regime, **b)** at the pinch off and **c)** saturation regime

2.4.3 Current Voltage characteristics

In order to analytically describe the current voltage characteristics in different operational regimes of an OFET, the gradual channel approximation is adopted. The basic assumption is that the field perpendicular to the current flow is much larger than the electric field parallel to the current flow created by the drain voltage.

When $V_G > V_{TH}$ the induced charge in an elemental strip, *dx*, of the channel is given by

$$dq = - C_i [V_G - V_{TH} - V(x)] W dx$$

Considering $V(x) = 0$ at the source and $V(x) = V_D$ at the drain, C_i is the capacitance per unit area of the dielectric, W the width therefore $W dx$ represents the area of the elemental strip. I_D can be expressed as the amount of charge dq passing from the source to the drain at time dt:

$$I_D = \frac{dq}{dt} = \frac{dq}{dx}\frac{dx}{dt}$$

by introducing the concept of mobility of charge carriers, μ, which can be defined as the ratio between the mean velocity (dx/dt) of the charge carriers and the electric field $E = -dV/dt$, the equation becomes:

$$I_D dx = W C_i \mu [V_G - V_{TH} - V(x)] dV$$

I_D is obtained by integrating the equation from source to (x = 0, V(x) = 0) to drain (x = L, V(x)= V_D)

$$I_{D, lin} = \frac{W}{L} C_i \mu (V_G - V_{TH} - V_D/2) V_D$$

the last holds in *linear regime*, where $V_D < V_G - V_{TH}$

In *saturation regime,* where $V_D = V_G - V_{TH}$, the integration of the equation results in:

$$I_{D, sat} = \frac{W}{2L} C_i \mu (V_G - V_{TH})^2$$

2.4.4 Electrical Characterization and Transport Parameters Extraction

In order to evaluate OFET performances, the device is characterized in standard conditions. Two main curves are recorded: transfer curve and output curve.

i) Transfer characteristics

The OFET is characterized by measuring I_{DS} when a voltage is applied to the gate V_{GS}. The source is generally grounded while potential is applied to the drain. I_{DS} is plotted vs V_{GS}, that is why the transfer is sometimes called *I-V* curve. From a transfer curve several relevant parameters can be extracted, among them: mobility μ, threshold voltage V_{TH} and on/off current $I_{ON/OFF}$. Mobility is extracted by taking the slope of the linear part of I_{DS} vs V_{GS} when measured in linear regime. In the case of saturation regime, it is taken from the slope of the linear part of sqrt(I_{DS}) vs V_{GS} (**Figure 6**). V_{TH} is extracted by taking the intersection of the extrapolated linear part of the transfer curve. From a transfer curve, the transconductance, *g*, can also be extracted. It is defined as dI_{DS}/dV_{GS} and it is expressed in Siemens (S).

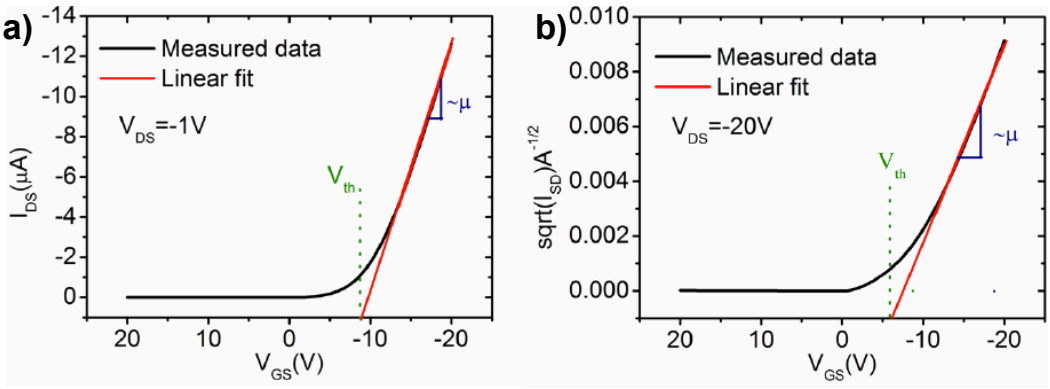

Figure 6 Typical transfer characteristics obtained for pentacene based OFETs. **a)** Measurements performed in the linear regime and **b)** measurements done in the saturation regime.

i) Output characteristics

To record an output characteristics of OFETs the I_{DS} is measured vs the V_{DS} for different V_{GS} (**Figure 7**). The linear and saturation regimes are distinguishable. Visual information about possible contact resistance of the device is given.

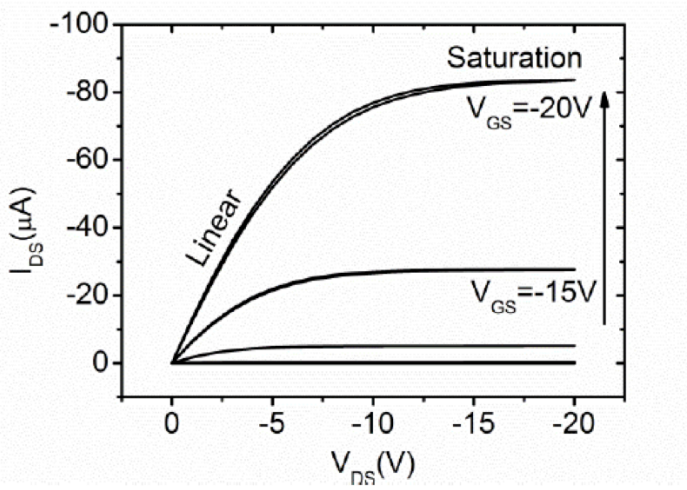

Figure 7 Typical output characteristics of a p-type OFET.

2.4.5 OFETs as Interfacial Sensors Devices

OFETs are basic device architectures used to probe organic materials. Stable operation is generally demonstrated in inert atmospheres in a glove box or in high vacuum conditions. Indeed, the sensitivity of these devices to electrochemically active species[20] (e.g.: water, oxygen) is demonstrated and OFET-based gas and humidity sensors[21] are widely studied. Weak points of these devices were optimization of specificity and robustness. These problems were addressed by investigating in detail the mechanisms of such degrading interaction and by optimizing the semiconductor structures to get OFETs durably operating in ambient conditions[22]. In an OFET sensing experiment the current response of the transistor changes when the device is exposed to analyte vapours or solutions due to chemical species, which adsorb to one of the device interfaces or diffuse into the semiconductor[23]. The investigation of the details of the interaction mechanisms is complex and often represents an open issue. Several OFET interfaces can be involved in sensing: (i) the electrode/semiconductor, (ii) dielectric/semiconductor, (iii) organic/organic interfaces (i.e. grain

boundaries) and (iv) semiconductor/ambient interface. In addition to electrostatic interactions, morphological or chemical changes in the semiconductor might occur and evoke the device response upon exposure to the analyte. Simplifying, two classes of interactions can alter the organic semiconductor's electronic properties:

- Analyte molecules can create trap states or provide additional charges to the semiconductor. As a consequence the density of mobile carriers changes and the threshold voltage shifts. This behaviour is often attributed to polar or redox active molecules and effectively corresponds to the chemical doping of the semiconductor.
- Analyte/semiconductor interaction can involve a change in the electronic coupling along the charge carrier transfer path in the semiconductor. This is often attributed to irreversible morphological changes or interactions at grain boundaries. As a consequence, the charge carrier mobility is altered and experimentally a change in transconductance is the response to the sensing event.

In OFET sensing experiments a multi-parametric response of the transistor is observed upon a binding event at one of the OFETs active interfaces and includes changes in mobility, threshold voltage, off current or other transistor parameters. When high sensitivity is required, monitoring of I_D at constant V_D and V_G during OFET exposure to different analyte concentrations is performed. This mode of operation is equivalent to chemo-resistive sensors (chemristors). Significant relative changes in current ($\Delta I_D/I_D$) have been observed for analyte concentrations as low as the ppb range for detection in gases[24] and liquids[25]. On the contrary, multi-parametric analysis, based on the simultaneous measurement of the transconductance and drain current, offers advantages when the targets are complex analyte mixtures and specific detection.

2.5 OFETs in water

For the transduction of biomolecules or of biological events, the sensor is supposed to be operated in an aqueous environment. As discussed, standard organic electronics devices show, due to various factors, high instability in water. The main issue regarding operating electronic devices in water is that it is an electrolyte and it is electrochemically active. Ultrapure water dissociates and contains a minimum amount of solvated protons and hydroxyl ions of 10^{-7} M. The resulting ionic conductivity, due to proton transfer, is about 10^{-5} S/m. At a standard potential of 0.571 V vs SHE (which is the standard hydrogen electrode) water oxidises:

$$2\ H_2O \rightleftharpoons 4\ H^+ + O_2 + 2\ e^-$$

While at a standard potential of -0.658 V vs SHE water get reduced

$$2\ H_2O + 2\ e^- \rightleftharpoons H_2 + 2\ OH^-$$

Electrochemical reactions set a limit to potentials that can be applied to the electrodes of an OFET in contact with water. In particular, when the potential difference between S and D is above 1 V, a faradic current, that is the result of electrolysis, flows. If a thick dielectric not permeable encapsulation provides necessary stability in liquid environment, it also strongly reduces efficacy of interaction between device and the interfaced environment resulting in low sensitivity or low stimulation capability.

Recently, new materials and architectures were introduced which circumvent the problems.

2.5.1 Electrolyte Gated OFETs

If the usage of water represents a strong limitation in standard electronic devices, which are commonly operated at V_D higher then 20 V,

becomes a great advantage in the case of Electrolyte Gated Organic Field Effect Transistors (EGOFETs). These devices (**Figure 8**) are operated without a dielectric while they are gated through the electrolyte by exploiting the capacitance illustrated in Section 2.2.1. Indeed, the electric field which leads to accumulation is no longer created by the metallic bottom gate but by the ionic charges which constitute the double layer at the semiconductor–water interface. As the two oppositely charged layers are almost in direct contact with only the solid–liquid-interface separating them (few Å), a large capacitive coupling arises. Extracted capacitances[26–28] for typical interfaces (e.g. sexitiophene, P3HT, pentacene) set in the range of few μF/cm^2 [27,28] while a 200 nm thick thermally grown SiO_2 capacitance is about 19 nF/cm^2, two orders of magnitude lower. As a result, small potential differences between the liquid and the semiconducting channel induce substantial charge density inside the channel, thus allowing low voltage operation. The above discussed electrochemical reactions between hole charges and water are likely to occur to some extent also at this interface. Nevertheless, they do not affect transfer characteristics as the protons are not trapped in a dielectric but instead are neutralized by autoprotolysis of water and result only in a small ionic leakage current (typically a few nA) at the gate electrode. Although the devices show robust performance, they do not exhibit the mobility reported for optimized solid-state OFET. This can be partly explained by the increased roughness of the solid–liquid interface where charge transport takes place and in addition by water polarization effects which set an upper limit. Both small molecules (e.g. pentacene) and polymers (e.g. P3HT, Poly(3-hexylthiophene-2,5-diyl)) are used as semiconducting materials in EGOFET.

At a planar semiconductor/liquid interface a quasi two-dimensional channel forms. The standard equations of OFETs presented in Section 2.4.3 also describe the EGOFET and its current-voltage characteristics.

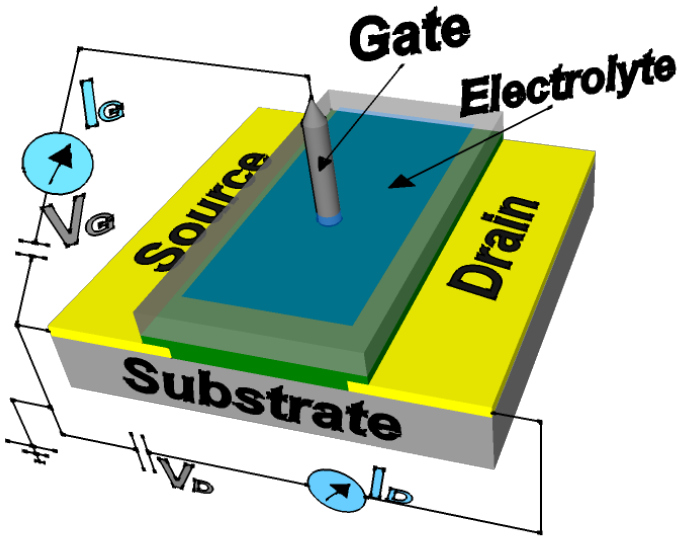

Figure 8 Scheme and wiring diagram of an EGOFET.

Organic Electrochemical Transistors (OECTs) formally belong to the class of EGOFETs since they are gated by an electrolyte, which is not separated by a dielectric layer from the semiconductor. Wrighton et al. developed the concept of the OECT in 1984[29]. They realized a three terminal device based on an electropolymerized polypyrrole film gated through an aqueous electrolyte. The working principle was ascribed to changes in polypyrrole conductivity due to the voltage-induced switching from oxidized to reduced state and vice versa. Many different materials were investigated such as polyaniline[30] and polycarbazole[31]. Recently, the organic electronics (OE) community focused on a very interesting material, the poly(3,4-ethylenedioxythiophene) doped with poly(styrene sulfonate), PEDOT:PSS. It is a heavily doped p-type polymeric semiconductor that, when used as the active channel, gives rise to a "normally on" transistor-like behaviour. Most of the scientific community agrees on the working principle initially proposed: doping/de-doping of the organic semiconductor layer is driven by the application of an appropriate gate voltage[29,32,33]. In its pristine state PEDOT:PSS is oxidized and shows

high conductivity and, when a positive bias is applied at the gate electrode, cations (from the electrolyte) enter the PEDOT:PSS film compensating the pendant sulfonate anions thus reducing the doping state of the polymer and its conductivity.

Other authors propose a different mechanism that takes into account the in-homogeneous nature of these polymers, formed by a highly conductive crystal core of PEDOT:PSS surrounded by a shell of excess insulating PSS[34], and how this is affected by the positive voltage applied[35–38]. They have demonstrated that 2% of the holes on the polymer backbone compensated by ionic charges inserted from the insulating layer was sufficient to alter the PEDOT conductance up to three orders of magnitude. This small fraction of charge compensation demonstrates that the suppression of the PEDOT:PSS conductance does not result from a pure electrochemical effect. Further studies demonstrated that inserted ions interrupt the low dimensional carrier-hopping network on the polymer backbone causing a conductor/non-conductor transition. So, the ion diffusion coupled with the free carrier motion on the PEDOT backbone results in a different “new type” of field effect mechanism. The thin-film transistor equations are no longer applicable, in their place it is necessary to introduce expressions that account for the semiconductor thickness[39]. What is universally accepted is the importance of ionic transport, which makes OECTs ideal converter of ionic current into electronic currents.

2.5.2 EGOFETs as Biosensors

High sensitivity toward a specific analyte is achieved by incorporating specific recognition sites into the device. Different approaches are adopted: i) usage of membranes, which only allow percolation of a specific analyte towards the sensitive interface; ii) attachment of a probe molecule onto one of the active interfaces such as electrodes or semiconductors; iii) incorporation of the probe into the

semiconductor. The last two approaches are generally preferred and recently deeply investigated. Chemical binding, or specific electrostatic interaction, between the target and the probe generates changes in the interfacial electrostatics. The coupled transistor channel transduces the interaction as a change in the charge transport or charge density. As a result, a different current-voltage characteristic is recorded.

Several examples of EGOFETs or OECTs transducers are reported, which sense bioactive molecules (e.g. glucose[40] and dopamine neurotransmitter[41]), enzymes (e.g. glucose oxidase[42,43]) or proteins (e.g. interleukin-4[44]). These devices were also demonstrated as sensors of bioelectric signals both *in vitro* and *in vivo.* Here we report the first approaches and two relevant recent examples.

P. Bergveld set the foundation for the usage of integrated circuits from the silicon technology to achieve extracellular detection. In the 1972 he presented the ISFET (ion sensitive FET) as a powerful tool for electrophysiology[45] and his vision was confirmed by the several hundreds of paper following his original publication[46]. The interest about using these devices raised and several configurations were investigated. P. Fromherz and his group investigated the silicon/cell interface by performing combined recordings and stimulations by the established patch clamp technique and FET based recordings[47]. They introduced an important model that elucidates the nature and characteristics of the interface and which analyses the electrical contribution of each element towards an increasing of the efficacy for both stimulation and recording[48,49]. With the opening provided by OFETs to new opportunities and architectures, various approaches to stimulation and sensing were tested and promising results obtained.

T. Cramer et al. presented an EGOFET fabricated on a Si-SiO_2 for the bidirectional communication with neural stem cell[50] (**Figure 9**). As a

semiconductor they proposed an ultra-thin film of pentacene on which murine stem cells were plated, cultured and differentiated. A dense interconnected network was formed and pentacene layer biocompatibility demonstrated up to two weeks. Fast voltage stimuli were applied by pulsing the V_{GS} through the gate electrode represented by a platinum wire immersed in the cell culture medium. The collective electrophysiological response of the neural network influenced the drain current during the transistor operation and transients, proportional to the intensity of the stimuli, were recorded. The authors were aiming at recording collective responses rather than LFPs, as demonstrated by the usage of mm^2 transistor area, which precludes the sensing of the single cell. Relevance of these devices could be demonstrated *in vivo*, for the sensing of signals from the central or peripheral nervous system. Unfortunately, as it will be discussed, the silicon scaffold represents a strong limitation, which can be circumvented by using different materials.

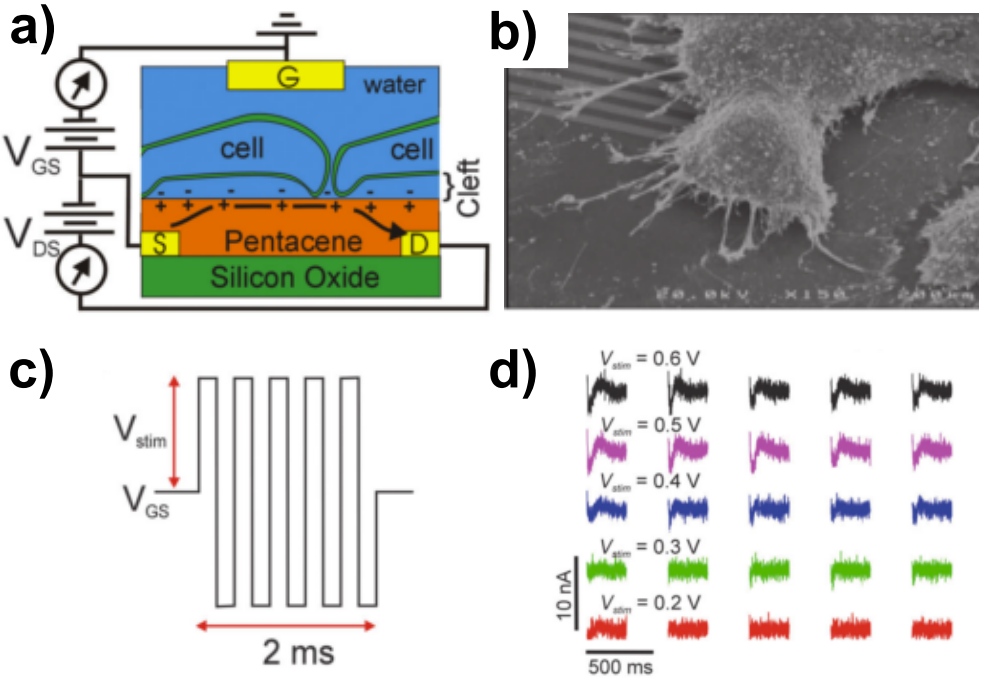

Figure 9 a) Scheme showing the wiring diagram of electrolyte gated pentacene transistor for neural interfacing; **b)** Scanning electron microscopy micrograph with a detail of neurons on active devices at day 9 after performing the electrical

analysis; **c)** shape of the stimulation pulse applied to the potential between the source and the gate; **d)** absolute current traces measured after stimulations of increasing intensity. Reprinted with permission from Ref. [50]

Among tens of examples about OECTs sensing capabilities[51], the first electrophysiological recording *in vivo* was reported by Khodaghouly et al[52]. The authors presented an OECTs array fabricated onto a 2 µm thick parylene film (**Figure 10**). It is transparent, flexible and biocompatible and it adheres perfectly to the cortex tissue. It was demonstrated more efficient than both standard commercial Ir penetrating electrodes and PEDOT:PSS electrodes in the recording of epileptic activity. The recording is based on the high ion to electron conversion capability of the PEDOT:PSS used as channel and on the amplification principle of the transistor configuration. These devices represent the most promising configuration due to their stability and versatility even if few issues like the usage of a common reference electrode have to be addressed.

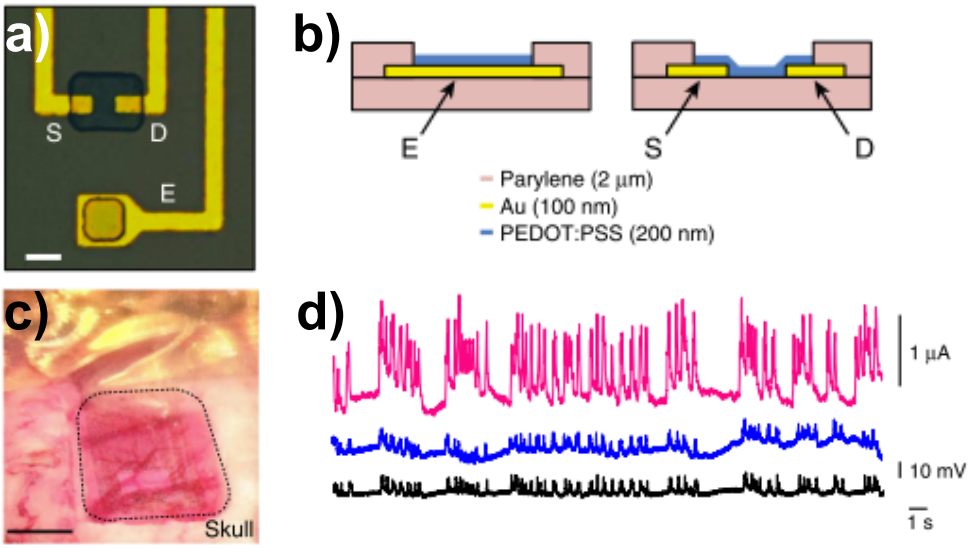

Figure 10 a) and **b)** are respectively the optical micrograph top view and schematic side view of the channel of a transistor and a surface electrode in

which the Au films that act as source (S), drain (D) and electrode pad (E) are identified. Scale bar in a) is 10μm. **c)** Optical micrograph of the probe placed over the somatosensory cortex, with the craniotomy surrounded by dashed lines. Scale bar, 1mm. **d)** Recordings from an OECT (pink), a PEDOT:PSS surface electrode (blue) and an Ir-penetrating electrode (black). Reprinted with permission from Ref. [52]

2.6 Implantable devices

Even though several different platforms and architectures have been developed in the last decades, the number of functional devices to interface various tissues for the treatment of targeted pathologies is limited. Indeed, device functionality is not the unique requirement for an implantable device. The greatest challenge to obtain durable and operationally stable devices is the biological response that interfaced tissue produces against the implant. Indeed, the implant can generate a non-specific immune response called foreign body reaction (FBR) that can lead to its failure[53]. FBR is better described in the following.

2.6.1 Foreign body reaction

Two major aspects represent the critical factors for long lasting implants i.e. materials biocompatibility and mechanical properties. IUPAC gives two different definitions of biocompatibility depending on the context. The most generic is the “ability of a material to be in contact with a living system without producing an adverse effect”. The second definition is more specifically related to biomedical therapy: it is the “ability of a material to perform with an appropriate host response in a specific application”[54]. The last seems more appropriate since no material can perform with an appropriate response in all the possible applications. The

evaluation of selected materials and devices intended for application in humans require a structured program of assessment to establish safety and biocompatibility. The program requires that manufacturers conduct adequate safety testing of their materials or devices through preclinical and clinical phases. Principal organizations to set the current regulations are the U.S Food and Drug Administration (FDA), the international Organization for Standardization (ISO) and the Japanese Ministry of Health and Welfare (JMHW). The preliminary tests to screen the biocompatibility of materials for implantable devices are *in vitro*. The regulation includes positive and negative control materials, choice of cell line and cell culture medium etc. For a standard implant, high mechanical, chemical and electrical stability are required. Stability ensures the material does not release detrimental agents. However, in the past decades transient prosthetics became very appealing. Sensors, drug releasing implants or electrical stimulators, which have to be used for a limited time window, can be explanted or fabricated with bioresorbable materials. The substrates and functional active components of the implant may be resorbed and metabolized within the body. The functionality of such device has to be maintained for the whole therapeutic window. The required lifetime ranges from few hours to months depending on the application. The potential of transient prosthetics is high and the interest of the scientists led to development of new biodegradable materials.

Focusing on the second requirement for the materials, i.e. mechanical properties, one has to consider this is the main factor inducing acute FBR. If a high mismatch between the mechanical properties of the implanted electrodes and the mechanical properties of the tissue is set, the acute FBR is triggered. Elastic modulus of the spinal cord (1 – 100 kPa) and the brain (3 – 100 kPa) are very low with respect elastic modulus of standard material for electronics i.e. silicon (150 – 170 GPa). Tolerability issues are found in the interfacing silicon chips and brain[55,56]. Plastic electronics provides softer standard biocompatible materials like

polydimethilsiloxane PDMS (about 100 MPa), polystyrene PS (5 MPa) or polyimide PI (2 MPa). However, the gap is only partially filled and the mismatch is still evident. Many investments of the scientific community are performed in order to further reduce the difference while keeping high the implant handing. The role of mechanical properties is not fully elucidated and further studies are needed in order to investigate the interplay of the chemical and mechanical factors that contribute to glial scarring surrounding implants when chronic FBR takes place. However, over time the electrode and scaffold surfaces are anchored to the tissue through extracellular matrix and neural inflammatory cells resulting in cellular attachments to the electrode and subsequent modification of the force exerted on the tissues. Due to macroscopic movements of the host animal, the implant locally rearranges thus generating strong forces on the tissues during scar maturation. Movements cause injuries that maintain the inflammatory process.

If the two requirements, i.e. biocompatibility and mechanical properties, are not properly satisfied FBR starts[53]. It is generally divided into phases, from the acute to the chronic, that are depicted in **Figure 11**. Blood vessels and tissue disruption occurs during implantation process and later due to implant micro-movements. Cells leak plasma fluid and blood immune cells (i.e. monocytes/macrophages, mast cells and neutrophils) are recruited. Inflammatory cells release numerous neurotoxic factors and after the first days microglia have degraded most cellular debris and damaged matrix by phagocytosis. The surface of the implanted device aspecifically adsorbs protein that favors the adhesion of inflammatory cells. Macrophages, locally differentiated from monocytes, migrate toward the implant surface intending to lead to its degradation. To do so, they release lytic enzymes and reactive oxygen agents and attempt to phagocyte the foreign object. Macrophages also secrete pro-inflammatory cytokines (e.g. tumor necrosis, interleukins, chemokines) and growth factors. Starting from the second week after implantation, a

dense sheath forms, supported by astrocyte proliferation, around the device that is called glial scar. It isolates neural electrodes from the surrounding tissue with a sort of fibrotic encapsulation.

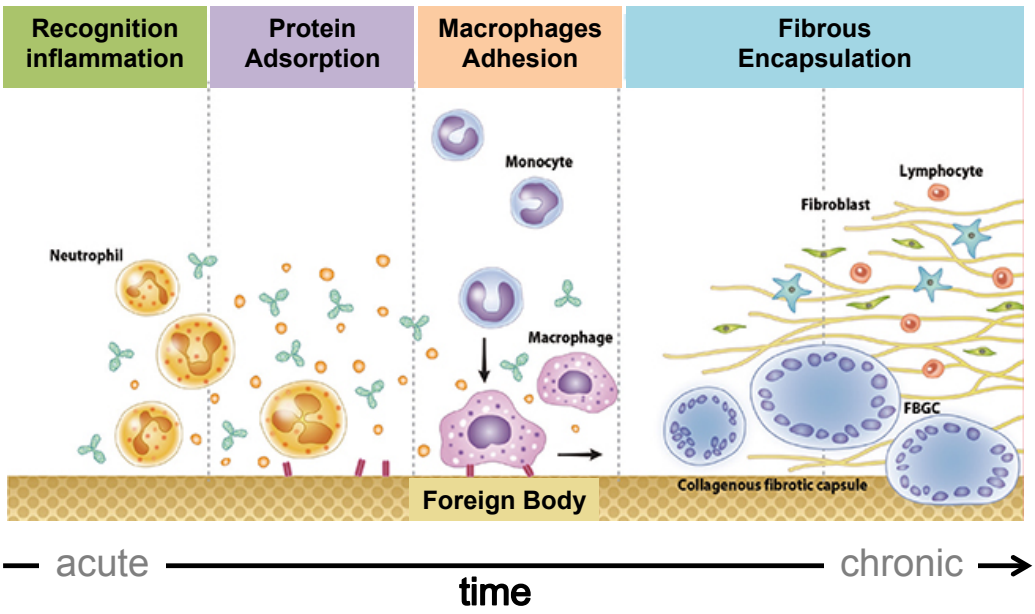

Figure 11 Scheme of the FBR steps. Damaged tissue release host proteins and blood that are absorbed on the implant surface. Neutrophils (i.e. leukocytes) and macrophages are recruited on the guest surface. Macrophages secrete enzyme to degrade the guest and factors that recruit and activate fibroblasts. A fibrous capsule develops around the material that insulates it thus preventing functionality. Modified from ref [57].

2.6.2 Materials

In order to reduce the FBR induced by an implant, an appropriate materials choice is fundamental[58,59]. Several are the materials that trigger FBR including polyethylene, poly(ethylene glycol), silicone rubber and titanium. Indeed, softness and biocompatibility are not unique requirements but surface morphology, wettability and surface tension also play a role. To obtain optimal conditions one can tune the properties of the material with specific coatings made for instance of poly(lactic-co-glycolic)

acid (PLGA), hydrogels or phospholipids membranes or perform specific physical or chemical functionalization. The material can also be loaded with anti-inflammatory drugs and specific mechanisms for the release can be designed. In this sense, organic materials offers the great advantage of the easy chemical synthesis and functionalization that can provide hundreds of small molecules or polymers with similar but different well-defined properties[60,61]. They can be specifically designed and synthetized tailoring the surgical and operational needs. It is highly desirable to have an implant characterized by high stiffness at the very first hours that softens with time. This enables an easy implantation surgery and allow with time higher conformability that implies higher sensitivity, higher efficiency during electrical stimulation and lower induced FBR[62].

An implant designed to perform electrical stimulation and recording is composed of the scaffold and the active materials. The scaffold is preferably made of a standard biocompatible material. Active components of the implant have to perform specific tasks. They can be conductors or semiconductors (depending on the final role in the device) characterized by i) stable and excellent electrical properties, ii) stability in physiological environment, iii) robustness and, obviously, iv) bio- and mechanical compatibility. Metals like gold and titanium are still used as thin conductive leads or electrodes but recently the usage of conductive and semiconducting polymers is rising exponentially. Two semiconducting polymers polypyrrole (PPy) and the already mentioned PEDOT show an incredible potential for their both recording and stimulation properties as neural interfaces. These capabilities are expressed in terms of reduced impedance, enhanced charge capacity and short time response[9,63–66]. Their compatibility is demonstrated *in* vitro with different cell lines and several are the studies *in vivo*, which are giving promising results[9]. PEDOT is generally preferred both because of high porosity, which increases the interfacial area while decreasing the electrode impedance, and because of its high stability in physiological environment. Furthermore, it is characterized by an easy processability. It can be i)

electropolymerized (to get polymer covered electrodes); ii) deposited by spin coating or by spray coating and then it can be patterned with various wet or dry etching techniques.

2.7 The i-ONE FP7 project and the scope of the thesis

The current thesis work is closely related to the FP7 i-ONE project[67] (Grant Agreement No. 280772). The consortium consisted of 10 different partners Institutions from 7 countries. i-ONE stands for Implantable Organic Nano Electronics and refers to the device envisioned for the treatment of the spinal cord injury (SCI). SCI pathophysiology, as described in Chapter 1, involve severance of axons, loss of neurons and glia and demyelination associated with a secondary inflammatory degenerative process. The extension of the lesion depends on different factors and leads to different functional deficits. Very often, SC undergoes an incomplete injury and spare neural tissue triggers a partial spontaneous recovery. The acute inflammatory response also plays an important role onto the final recovery. If it is monitored and down regulated some late damages to spare neural tissue can be prevented. The higher the amount of post-injury neural tissue, the more likely neural plasticity promotes recovery. It is demonstrated that electrical stimulation, administration of specific therapies and training encourage neural plasticity.

In order to target the different aspects of the SCI and to tailor the needs of a complex regenerative process, the implant envisioned by i-ONE consortium is highly multifunctional. The vision is to fabricate a device, designed for epidural or subdural implantation, to interface the SC soon after the injury. At the very beginning, the device, which integrates sensors for inflammatory response, monitors the state and performs local

delivery of drugs upon need by means of a microfluidic system. The device has to integrate active electrodes for the delivery of precise and tunable electrical stimulation in order to promote plasticity from the sub-acute phase. In this phase, delivery of anti-inflammatory is associated with the delivery of growth factors. In the vision, device functionalities are not exhausted; it integrates highly sensitive organic transducers (preferably highly sensitive organic transistors) to sense neural electrical activity and to evaluate the regeneration process. i-ONE innovative approach also involves the materials that compose the device, which is supposed to behave like a transient implant. In order to maximize the biocompatibility and safety and to reduce the risk of a host versus graft immune response, the usage of mostly organic and highly biodegradable materials is recommended. The device is supposed to work stably for the therapeutic window (from weeks to months) and then degrades. The patient is not subject to a second surgery for the removal of the implant and the detrimental effects of the long-term FBR are prevented. The project is divided into different work packages. The validation *in vitro* precedes the *in vivo* implantation into rodents.

During the PhD I was involved in the fabrication and characterization of the so-called Active Multifunctional Implantable Device, AMID, and the implementation of the stimulation and sensing protocols. The multidisciplinary project necessarily evolves step-by-step. The PhD timeline can be divided into few main blocks: i) development of a highly biodegradable and fully biocompatible device for the stimulation and sensing of bioelectric signals and its demonstration in a medically relevant application (Chapters 3 and 4); ii) demonstration of efficacy of electrical stimulation *in vitro* onto significant cell lines (Chapter 5, in collaboration with University of Cambridge); iii) development of a fabrication strategy to obtain an implantable multifunctional device with the desired characteristics (Chapter 6); iv) validation of efficient electrical stimulation

onto healthy and injured SC rodents and investigation of the AMID-induced FBR (Chapter 7, in collaboration with University of Cambridge).

A first screening of the most suitable materials to be used as scaffold, leads to poly(lactic-co-glycolic) acid, PLGA, which is well known for its biocompatibility and biodegradability. At the same time, the development of a fabrication strategy to obtain organic transistors on PLGA operating in physiological environment is needed. After the platform for the stimulation and for the recording of bioelectric signals is validated, the devices are tested *in vitro.* In order to evaluate the real efficacy of electrical stimulation onto relevant cell lines, a complete setup that allows one to perform a real-time optimization of both the architecture and the stimulating parameters have to be prepared. The setup has to be characterized by easy-to-use apparatus and interfaces in order to be used by non-expert operators. After having verified and optimized the efficacy of the stimulation onto neural-like cells and having investigated the effect, same parameters will be adopted onto other inflammatory SCI relevant cell lines. Once a stimulation safety protocol is set *in vitro,* the technology is transferred towards the development of the implantable device, AMID. As previously mentioned, the requirements for having safe neuroprostheses are stringent and device multifunctionality requires a completely new strategy to be developed. AMID performances have to be evaluated and the implant has to be validated *in vivo* with mice and rats SCI models. The three years long project is not enough for addressing long-term efficacy. We focus on the *in vivo* subacute FBR and on the effective capability of AMID to stimulate bioelectric activity onto rodent in acute SCI.

To summarize, the goal of the thesis is the development of a platform to take a step forward in available neuroprostheses for spinal cord stimulation. A transient AMID, characterized by high biodegradability,

capability of performing bidirectional communication and drug delivery, has to be fabricated and its activity demonstrated.

Bibliography

(1) Galvani, L. *De Viribus Electricitatis in Motu Musculari Commentarius*; Bologna, 1791; Vol. VII.

(2) Hodgkin, A. L.; Huxley, A. F. A Quantitative Description of Membrane Current and Its Application to Conduction and Excitation in Nerve. *Bull. Math. Biol.* **1990**, *52*, 25–71.

(3) Neher, E.; Sakmann, B.; Steinbach, J. H. The Extracellular Patch Clamp: A Method for Resolving Currents through Individual Open Channels in Biological Membranes. *Pflugers Arch.* **1978**, *375*, 219–228.

(4) Spira, M. E.; Hai, A. Multi-Electrode Array Technologies for Neuroscience and Cardiology. *Nat. Nanotechnol.* **2013**, *8*, 83–94.

(5) Grahame, D. C. The Electrical Double Layer and the Theory of Electrocapillarity. *Chem. Rev.* **1947**, 441–501.

(6) Merrill, D. R.; Bikson, M.; Jefferys, J. G. R. Electrical Stimulation of Excitable Tissue: Design of Efficacious and Safe Protocols. *J. Neurosci. Methods* **2005**, *141*, 171–198.

(7) Schoen, I.; Fromherz, P. The Mechanism of Extracellular Stimulation of Nerve Cells on an Electrolyte-Oxide-Semiconductor Capacitor. *Biophys. J.* **2007**, *92*, 1096–1111.

(8) Schoen, I.; Fromherz, P. Extracellular Stimulation of Mammalian Neurons through Repetitive Activation of Na+ Channels by Weak Capacitive Currents on a Silicon Chip. *J. Neurophysiol.* **2008**, *100*, 346–357.

(9) Venkatraman, S.; Hendricks, J.; King, Z. a.; Sereno, A. J.; Richardson-Burns, S.; Martin, D.; Carmena, J. M. In Vitro and in Vivo Evaluation of PEDOT Microelectrodes for Neural Stimulation and Recording. *IEEE Trans Neural Syst Rehabil Eng* **2011**, *19*, 307–316.

(10) Renshaw, B.; Forbes, a.; Morison, B. R. Activity of Isocortex and Hippocampus: Electrical Studies with Micro-Electrodes. *J. Neurophysiol.* **1940**, *3*, 74–105.

(11) Nyberg, T.; Shimada, A.; Torimitsu, K. Ion Conducting Polymer Microelectrodes for Interfacing with Neural Networks. *J. Neurosci.*

Methods **2007**, *160*, 16–25.

(12) Normann, R. A.; Maynard, E. M.; Rousche, P. J.; Warren, D. J. A Neural Interface for a Cortical Vision Prosthesis. *Vision Res.* **1999**, *39*, 2577–2587.

(13) Metallo, C.; White, R. D.; Trimmer, B. A. Flexible Parylene-Based Microelectrode Arrays for High Resolution EMG Recordings in Freely Moving Small Animals. *J. Neurosci. Methods* **2011**, *195*, 176–184.

(14) Khodagholy, D.; Gelinas, J. N.; Thesen, T.; Doyle, W.; Devinsky, O.; Malliaras, G. G.; Buzsáki, G. NeuroGrid : Recording Action Potentials from the Surface of the Brain. *Nat. Neurosci.* **2014**, *18*, 310–316.

(15) Lilienfeld, J. E. Methods and Apparatus for Controlling Electric Currents. **1930**, US patent 1,745,175.

(16) Kahng, D. Electric Field Controlled Semiconductor Device. **1963**, US Patent 3,102,230.

(17) Ebisawa, F.; Kurokawa, T.; Nara, S. Electrical Properties of Polyacetylene/polysiloxane Interface. *J. Appl. Phys.* **1983**, *54*, 3255.

(18) Tsumura, a.; Koezuka, H.; Ando, T. Macromolecular Electronic Device: Field-Effect Transistor with a Polythiophene Thin Film. *Appl. Phys. Lett.* **1986**, *49*, 1210–1212.

(19) Kymissis, I. *Organic Field Effect Transistors Theory, Fabrication and Characterization*; Springer US: New York, 2008.

(20) Bobbert, P. A.; Sharma, A.; Mathijssen, S. G. J.; Kemerink, M.; de Leeuw, D. M. Operational Stability of Organic Field-Effect Transistors. *Adv. Mater.* **2012**, *24*, 1146–1158.

(21) Torsi, L.; Dodabalapur, A.; Sabbatini, L.; Zambonin, P. G. Multi-Parameter Gas Sensors Based on Organic Thin-Film-Transistors. *Sensors Actuators B Chem.* **2000**, *67*, 312–316.

(22) Guo, X.; Ortiz, R. P.; Zheng, Y.; Hu, Y.; Noh, Y.-Y.; Baeg, K.-J.; Facchetti, A.; Marks, T. J. Bithiophene-Imide-Based Polymeric Semiconductors for Field-Effect Transistors: Synthesis, Structure-Property Correlations, Charge Carrier Polarity, and Device Stability. *J. Am. Chem. Soc.* **2011**, *133*, 1405–1418.

(23) Cramer, T.; Campana, a.; Leonardi, F.; Casalini, S.; Kyndiah, a.; Murgia, M.; Biscarini, F. Water-Gated Organic Field Effect Transistors – Opportunities for Biochemical Sensing and Extracellular Signal Transduction. *J. Mater. Chem. B* **2013**, *1*, 3728.

(24) Angione, M. D.; Cotrone, S.; Magliulo, M.; Mallardi, A.; Altamura, D.; Giannini, C.; Cioffi, N.; Sabbatini, L.; Fratini, E.; Baglioni, P.; *et al.*

Interfacial Electronic Effects in Functional Biolayers Integrated into Organic Field-Effect Transistors. *Proc. Natl. Acad. Sci. U. S. A.* **2012**, *109*, 6429–6434.

(25) Hammock, M. L.; Sokolov, A. N.; Stoltenberg, R. M.; Naab, B. D.; Bao, Z. Organic Transistors with Ordered Nanoparticle Arrays as a Tailorable Platform for Selective, in Situ Detection. *ACS Nano* **2012**, *6*, 3100–3108.

(26) Kergoat, L.; Herlogsson, L.; Braga, D.; Piro, B.; Pham, M.-C.; Crispin, X.; Berggren, M.; Horowitz, G. A Water-Gate Organic Field-Effect Transistor. *Adv. Mater.* **2010**, *22*, 2565–2569.

(27) Buth, F.; Kumar, D.; Stutzmann, M.; Garrido, J. A. Electrolyte-Gated Organic Field-Effect Transistors for Sensing Applications. *Appl. Phys. Lett.* **2011**, *98*, 153302.

(28) Cramer, T.; Kyndiah, A.; Murgia, M.; Leonardi, F.; Casalini, S.; Biscarini, F. Double Layer Capacitance Measured by Organic Field Effect Transistor Operated in Water. *Appl. Phys. Lett.* **2012**, *100*, 143302.

(29) White, H. S.; Kittlesen, G. P.; Wrighton, M. S. Chemical Derivatization of an Array of Three Gold Microelectrodes with Polypyrrole: Fabrication of a Molecule-Based Transistor. **1984**, 5375–5377.

(30) Paul, E. W.; Ricco, A. J.; Wrighton, M. S. Resistance of Polyanillne Films as a Function of Electrochemical Potential and the Fabrication of Poiyanlline-Based Microelectronic Devices. *J. Phys. Chem.* **1985**, *89*, 1441–1447.

(31) Rani, V.; Santhanam, K. S. V. Polycarbazole-Based Electrochemical Transistor. *J. Solid State Electrochem.* **1998**, *2*, 99–101.

(32) Nilsson, B. D.; Chen, M.; Kugler, T.; Remonen, T.; Armgarth, M.; Berggren, M. Bi-Stable and Dynamic Current Modulation in Electrochemical Organic Transistors. **2002**, 51–54.

(33) Stavrinidou, E.; Leleux, P.; Rajaona, H.; Khodagholy, D.; Rivnay, J.; Lindau, M.; Sanaur, S.; Malliaras, G. G. Direct Measurement of Ion Mobility in a Conducting Polymer. *Adv. Mater.* **2013**, *25*, 4488–4493.

(34) Takumi Takano, Hiroyasu Masunaga, Akihiko Fujiwara, Hidenori Okuzaki, and T. S. PEDOT Nanocrystal in Highly Conductive PEDOT:PSS Polymer Films. *Macromolecules* **2012**, *45*, 3859–3865.

(35) Hsu, F. C.; Prigodin, V. N.; Epstein, A. J. Electric-Field-Controlled Conductance of “Metallic” Polymers in a Transistor Structure. *Phys. Rev. B - Condens. Matter Mater. Phys.* **2006**, *74*, 1–12.

(36) Epstein, A. J.; Hsu, F.-C.; Chiou, N.-R.; Prigodin, V. N. Electric-Field

Induced Ion-Leveraged Metal–insulator Transition in Conducting Polymer-Based Field Effect Devices. *Curr. Appl. Phys.* **2002**, *2*, 339–343.

(37) Prigodin, V. N.; Hsu, F. C.; Park, J. H.; Waldmann, O.; Epstein, A. J. Electron-Ion Interaction in Doped Conducting Polymers. *Phys. Rev. B - Condens. Matter Mater. Phys.* **2008**, *78*, 1–9.

(38) Prigodin, V. N.; Epstein, A. J. Nature of Insulator-Metal Transition and Novel Mechanism of Charge Transport in the Metallic State of Highly Doped Electronic Polymers. *Synth. Met.* **2002**, *125*, 43–53.

(39) Bernards, D. A.; Malliaras, G. G. Steady-State and Transient Behavior of Organic Electrochemical Transistors. *Adv. Funct. Mater.* **2007**, *17*, 3538–3544.

(40) Macaya, D. J.; Nikolou, M.; Takamatsu, S.; Mabeck, J. T.; Owens, R. M.; Malliaras, G. G. Simple Glucose Sensors with Micromolar Sensitivity Based on Organic Electrochemical Transistors. *Sensors Actuators B Chem.* **2007**, *123*, 374–378.

(41) Casalini, S.; Leonardi, F.; Cramer, T.; Biscarini, F. Organic Field-Effect Transistor for Label-Free Dopamine Sensing. *Org. Electron.* **2012**.

(42) Yang, S. Y.; Cicoira, F.; Byrne, R.; Benito-Lopez, F.; Diamond, D.; Owens, R. M.; Malliaras, G. G. Electrochemical Transistors with Ionic Liquids for Enzymatic Sensing. *Chem. Commun. (Camb).* **2010**, *46*, 7972–7974.

(43) Bernards, D. a.; Macaya, D. J.; Nikolou, M.; DeFranco, J. a.; Takamatsu, S.; Malliaras, G. G. Enzymatic Sensing with Organic Electrochemical Transistors. *J. Mat. Chem.* **2008**, *18*, 116–120.

(44) Casalini, S.; Dumitru, A. C.; Leonardi, F.; Bortolotti, C. A.; Herruzo, E. T.; Campana, A.; Oliveira, R. F. De; Cramer, T.; Garcia, R.; Biscarini, F. Multiscale Sensing of Antibody-Antigen Interactions by Organic Transistors and Single-Molecule Force Spectroscopy. *ACS Nano* **2015**, *5*, 5051–5062.

(45) Bergveld, P. Development, Operation, and Application of the Ion-Sensitive Field-Effect Transistor as a Tool for Electrophysiology. *IEEE Trans. Biomed. Eng.* **1972**, *19*, 342–351.

(46) Bergveld, P. Thirty Years of ISFETOLOGY What Happened in the Past 30 Years and What May Happen in the next 30 Years. **2003**, *88*, 1–20.

(47) Fromherz, P.; Offenhausser, A.; Vetter, T.; Weis, and J. A Neuron-Silicon Junction: A Retzius Cell of the Leech on an Insulated-Gate Field-Effect Transistor. *Science (80-.).* **1991**, *31*, 1290–1293.

(48) Fromherz, P. Neuroelectronic Interfacing: Semiconductor Chips with

Ion Channels, Nerve Cells, and Brain. *Nanoelectron. Inf. Technol.* **2003**, 781–810.

(49) Kaul, R. A.; Syed, N. I.; Fromherz, P. Neuron-Semiconductor Chip with Chemical Synapse between Identified Neurons. *Phys. Rev. Lett.* **2004**, *92*, 038102.

(50) Cramer, T.; Chelli, B.; Murgia, M.; Barbalinardo, M.; Bystrenova, E.; de Leeuw, D. M.; Biscarini, F. Organic Ultra-Thin Film Transistors with a Liquid Gate for Extracellular Stimulation and Recording of Electric Activity of Stem Cell-Derived Neuronal Networks. *Phys. Chem. Chem. Phys.* **2013**, *15*, 3897–3905.

(51) Yao, C.; Xie, C.; Lin, P.; Yan, F.; Huang, P.; Hsing, I. M. Organic Electrochemical Transistor Array for Recording Transepithelial Ion Transport of Human Airway Epithelial Cells. *Adv. Mater.* **2013**, *25*, 6575–6580.

(52) Khodagholy, D.; Doublet, T.; Quilichini, P.; Gurfinkel, M.; Leleux, P.; Ghestem, A.; Ismailova, E.; Hervé, T.; Sanaur, S.; Bernard, C.; *et al.* In Vivo Recordings of Brain Activity Using Organic Transistors. *Nat. Commun.* **2013**, *4*, 1575.

(53) Anderson, J. M.; Rodriguez, A.; Chang, D. T. Foreign Body Reaction to Biomaterials. *Semin. Immunol.* **2008**, *20*, 86–100.

(54) Vert, M.; Doi, Y.; Hellwich, K.-H.; Hess, M.; Hodge, P.; Kubisa, P.; Rinaudo, M.; Schué, F. Terminology for Biorelated Polymers and Applications (IUPAC Recommendations 2012). *Pure Appl. Chem.* **2012**, *84*, 1.

(55) Bjornsson, C. S.; Oh, S. J.; Al-Kofahi, Y. a; Lim, Y. J.; Smith, K. L.; Turner, J. N.; De, S.; Roysam, B.; Shain, W.; Kim, S. J. Effects of Insertion Conditions on Tissue Strain and Vascular Damage during Neuroprosthetic Device Insertion. *J. Neural Eng.* **2006**, *3*, 196–207.

(56) Edell, D. J.; Toi, V. Van; McNeil, V. M.; Clark, L. D. Factors Influencing the Biocompatibility of Insertable Silicon Microshafts in Cerebral Cortex. *IEEE Trans. Biomed. Eng.* **1992**, *39*, 635–643.

(57) Lee, J. M.; Kim, Y. J. Foreign Body Granulomas after the Use of Dermal Fillers: Pathophysiology, Clinical Appearance, Histologic Features, and Treatment. *Arch. Plast. Surg.* **2015**, *42*, 232–239.

(58) Hassler, C.; Boretius, T.; Stieglitz, T. Polymers for Neural Implants. *J. Polym. Sci. Part B Polym. Phys.* **2011**, *49*, 18–33.

(59) Zhong, Y.; Bellamkonda, R. V. Biomaterials for the Central Nervous System. *J. Roy. Soc. Interface* **2008**, *5*, 957–975.

(60) Mandal, H. S.; Knaack, G. L.; Charkhkar, H.; McHail, D. G.; Kastee, J. S.; Dumas, T. C.; Peixoto, N.; Rubinson, J. F.; Pancrazio, J. J. Improving the Performance of poly(3,4-Ethylenedioxythiophene) for

Brain-Machine Interface Applications. *Acta Biomater.* **2014**, *10*, 2446–2454.

(61) Ghasemi-mobarakeh, L.; Prabhakaran, M. P.; Morshed, M. Application of Conductive Polymers , Scaffolds and Electrical Stimulation for Nerve Tissue Engineering. **2011**.

(62) Kim, D.-H.; Viventi, J.; Amsden, J. J.; Xiao, J.; Vigeland, L.; Kim, Y.-S.; Blanco, J. a; Panilaitis, B.; Frechette, E. S.; Contreras, D.; *et al.* Dissolvable Films of Silk Fibroin for Ultrathin Conformal Bio-Integrated Electronics. *Nat. Mater.* **2010**, *9*, 511–517.

(63) Asplund, M.; Nyberg, T.; Inganäs, O. Electroactive Polymers for Neural Interfaces. *Polym. Chem.* **2010**, *1*, 1374.

(64) Martin, D. C. Molecular Design, Synthesis, and Characterization of Conjugated Polymers for Interfacing Electronic Biomedical Devices with Living Tissue. *MRS Commun.* **2015**, 1–23.

(65) Wilks, S. J.; Richardson-Burns, S. M.; Hendricks, J. L.; Martin, D. C.; Otto, K. J. Poly(3,4-Ethylenedioxythiophene) as a Micro-Neural Interface Material for Electrostimulation. *Front. Neuroeng.* **2009**, *2*, 7.

(66) Venkatraman, S.; Hendricks, J.; Richardson-Burns, S.; Jan, E.; Martin, D.; Carmena, J. M. PEDOT Coated Microelectrode Arrays for Chronic Neural Recording and Stimulation. *2009 4th Int. IEEE/EMBS Conf. Neural Eng. NER '09* **2009**, *4*, 383–386.

(67) Implantable-OrganicNanoEctronics. I-ONE. *http://ione-fp7.eu/*.

chapter 3

Electrolyte Gated Field Effect Transistors on Biodegradable Substrate: a Facile Maskless Fabrication

The fabrication of test pattern with interdigitated gold electrodes on a biodegradable substrate is achieved by laser ablation of an Au film using a high-precision multifunction IR-laser scan marker. Two approaches are presented, a direct ablation process and a pattern-and-peel method. The approaches enable for fast prototyping of a variety of materials and devices. We demonstrate the fabrication of EGOFETs on the biodegradable poly(lactic-co-glycolic) acid (PLGA) scaffold and their operations in water and physiological environment.

3.1 Introduction

The fabrication of biomaterials is mostly by water-based or dry, and relies on processes that can alter the functionality of the materials commonly used in organic electronics. Conversely, printing techniques or photolithography are routinely used in organic electronics, however they are often non-compatible with biomaterials else the respective solubility is not orthogonal. Finding common processing windows for organic electronics materials and biomaterials is important for the possibility to interface organic devices to living systems, thus opening unprecedented opportunities in biomedicine[1–4]. Towards this aim, we developed a patterning technique for fabricating metal electrodes on the PLGA biodegradable scaffolds.

PLGA is an FDA approved biocompatible and biodegradable material. A considerable amount of research has been conducted on PLGA family that shown in the last decades its immense potential. Polypyrrole/PLGA fibres to combine electrical stimulation and topographical guidance in neural tissue engineering were tested and enhancement in neurite formation and length was demonstrated[5]. Copolymers of PLGA and caprolactone were investigated as biodegradable nerve tubular guides for the reconstruction of sciatic nerve[6]. PLGA is also known for being used for controlled drug delivery[7]. Various biodegradable PLGA devices fabricated from different techniques provide various classes of drug encapsulation and set different time periods and diverse routes of the delivery to tailor the specific implantation needs[8]. Among all the biomaterials PLGA is chosen for the favourable biocompatibility and well known degradation properties[9].

However, PLGA, as many others biopolymers, is soluble in chloroform, dichloromethane, acetone, fluorinated solvents and many other solvents which are used in micro and nanofabrication techniques. Therefore, photolithography and printing have to be excluded for the

patterning of gold electrodes or semiconductors. Shadow masking allows one to obtain features down to a few micrometres, however suffers for several limitations: i) contact with the substrate can result detrimental due to overheating, ii) patterning of large areas with small features is unreasonable and iii) prototyping is extremely slow and expensive due to the fabrication of new masks.

Our strategy exploits laser-assisted local ablation of a thin gold layer sublimated on the substrate. The resulting electrodes lead to the fabrication of transparent and fully biocompatible EGOFETs working in water. The viability our approach is first demonstrated on a standard rigid substrate, viz. quartz (Section 3.2), then on PLGA (Section 3.3).

A second strategy is proposed (Section 3.4) where the laser ablation is not directly performed on the final PLGA instead a sacrificial layer is used. The latter is the support on which the patterning is performed and from which metal electrodes are released to PLGA. This technique lead to the fabrication of EGOFETs operated in physiological environment.

3.2 Laser Ablation Protocol: EGOFET on Quartz

Quartz glass slide with 50 nm of gold and a titanium adhesive layer were used as purchased by Phasis, Geneva – Switzerland. Laser ablation of the Au film was performed with a short-pulsed Nd:YAG IR-laser (centre wavelength λ= 1064 nm) with a laser scan marker (ScribaR, Scriba Nanotecnologie S.r.l, Bologna, Italy) (**Figure 1**). Optimal parameters depend on dimensions of the desired features. Typical operation is performed at a laser power of 160 mW with pulse width of 10 ns and 14000 Hz repetition rate. The substrate is positioned under the laser beam on a stage equipped with inertial motors featuring an encoder for each axis. Motors control both the focal distance z and the x-y

displacement. The laser spot was moved over the surface at a speed of 2000 µm/s. The movement is finely controlled with an accuracy of less than 1 µm in x-y-z axes for 100 mm travel distance by means of a controller guided via a General User Interface (GUI). A CAD (Computer-Aided Design) file, created with the freeware DraftSight® software and containing the drawing (**Figure 2a**) defines the laser path. A software interface allows the operator to control the position and the ablation parameters in real time.

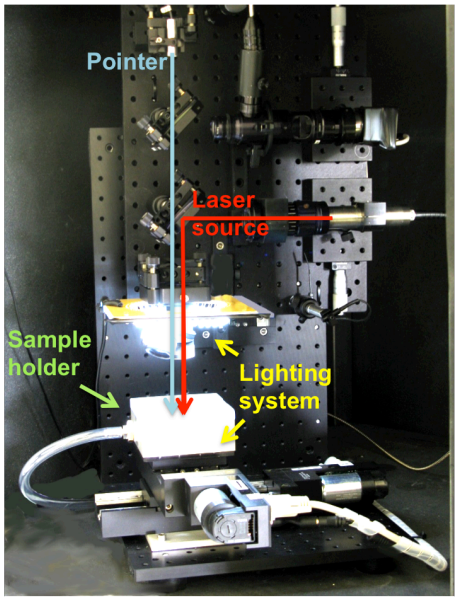

Figure 1 ScribaR Laser Marker. The sample holder stage (white) can be moved under the fixed laser source. The laser pointer and camera both positioned above the stage (orthogonally), allow the alignment of the incident beam on the pre-patterned sample. The focus is controlled through the z-positioner moving the moving the vertical optical table.

An advantage of this machine is the possibility to finely control the position of the incident laser beam and to re-align the ablation path on structures previously patterned on the surface with an epitaxial video microscope. The screen connected to the microscope CCD camera enables real time monitoring of the outcome of the ablation process. Fast

prototyping can be implemented by changing the drawing without additional steps of fabrication. The accurate control of the parameters allows the technique to be adapted to almost all the substrates provided they exhibit a negligible absorption of infrared radiation. The material, laser spot and optics limit the minimum channel length. 16 pairs of highly interdigitated electrodes (with L=15 μm and W = 26 mm, ratio W/L=1733) were patterned on the 1 x 1 cm^2 quartz (**Figure 2b**).

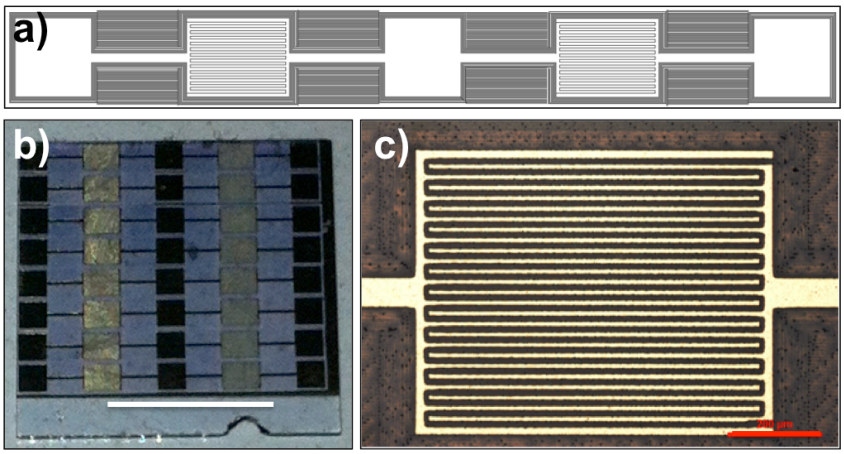

Figure 2 a) Technical drawing of two pairs of interdigitated source and drain electrodes with a common source. **b)** Photo of a quartz test pattern that contains 16 pairs of highly interdigitated electrodes patterned by scanning laser ablation technique. Ruler is 5 mm. **c)** Optical microscopy image of the electrodes with 15 μm channel length. Ruler is 200 μm.

After the ablation process, a six monolayer[10] (9 nm) nominal thickness) pentacene thin film was grown in a high vacuum chamber (base pressure < 10^{-7} mbar) by sublimation from a Knudsen cell at a rate of 7 Å/s, the nominal thickness being estimated with an AFM-calibrated quartz microbalance. The functional transistor, obtained by evaporation of the semiconductor, shows stable mechanical properties. Dewetting or delamination of the active layers was not observed upon immersion in pure water, saline water and cell culture medium.

3.2.1 EGOFET on Quartz: Electrical Performances

Electrical characterization was performed with a Pt wire as a gate electrode immersed in the solution confined on the active area with a PDMS pool adhered to the test pattern. Transfer curve in linear and saturation regime and output curves are reported in **Figure 3**. They exhibit typical FET response, stable low-voltage operation and low hysteresis. The transfer scan shows modulation of the drain current by two orders of magnitude. The leakage current I_{GS} (black curve) remains at least one order of magnitude lower.

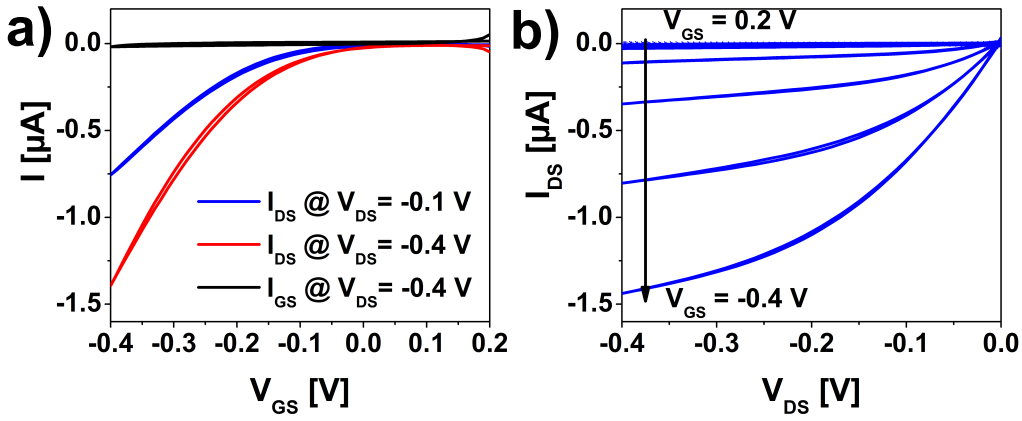

Figure 3 a) Transfer curve of the EGOFET in pure water obtained in linear (blue curve) and saturation (red curve) regimes. Leakage current is black curve. **b)** Output characteristics at different gate voltages. Both show low hysteresis and high current modulation.

The extracted charge carrier mobility, $\mu = (6.9 \pm 5.7)\ 10^{-4}\ cm^2/(Vs)$, and the threshold voltage, $V_{TH} = 0.15 \pm 0.5$ V, are about one order of magnitude lower with respect to their counterparts in EGOFETs fabricated on commercial silicon oxide test pattern[11].

3.3 Laser Ablation onto Soft Scaffold: EGOFET on PLGA

Copolymer PLGA, composed by 75:25 ratio of D,L-lactide and glycolide units (MW = 66-107 KDa, Sigma Aldrich), was used for manufacturing 20 μm thick films by solvent casting in chloroform. The thickness is controlled by confining the solution in a PDMS ring adhered to a glass slide cleaned with acetone and isopropanol. The ring forms a pool of 1 cm^2 area. The resulting films are transparent. Dr. Giulia Foschi, at UNIMORE now at Scriba Nanotecnologie Srl., developed this highly reproducible strategy for PLGA film production.

Ti (3 nm) as adhesive layer and Au (40 nm) were deposited (at a rate of 1 Å/s) in a high vacuum chamber (base pressure < 10^{-6} mbar) by thermal evaporation on PLGA films. Both Ti and Au are used for biomedical implants because of their resilient bio-fouling properties[12]. The deposition chamber was modified to keep the PLGA films 50 cm far from the evaporation boats. This reduces the heating of the substrates and preserves their integrity. Metal layer thickness was determined by means of a calibrated quartz microbalance. The laser ablation procedure described in detail in Section 3.2 was repeated onto PLGA. Different ablation parameters were used in order to find the best compromise between removal of the metal and thermal roughening of the underlying biodegradable scaffold. Optimal parameters depend on metal film thickness and dimensions of the desired features. For the specified thickness, a laser power of 150 mW with pulse width of 10 ns and 11000 Hz repetition rate was found to be effective. The overall fabrication of a test pattern with 10 pairs of source and drain electrodes (**Figure 4a**), takes about 20 minutes from the placement of the substrate on the sample holder. For high signal to noise ratio of the EGOFET, we patterned interdigitated electrodes minimizing the channel length (L = 12 μm) while maximizing the channel width (W = 26000 μm) (**Figure 4a** and **b**). Optical microscopy of the ablated Au electrodes reveals the removal of gold

(**Figure 4b**). Atomic Force Microscopy (AFM) was used to study the ablated electrodes in detail. **Figure 4c** shows an AFM image acquired at the boundary between electrode and channel. A well-defined interface with some line roughness separates the electrode from the channel where PLGA is exposed. An increasing height is observed at the rim of the electrodes as caused by the accumulation of gold caused by the dewetting process induced by the laser. Presence of ablated material can also be observed inside the channel. These clusters, which have small size and irregular shape, are isolated and do not cause shortcuts between the electrodes, as demonstrated with electrical measurements. They may affect the threshold voltage. The surface of the resulting channel is also characterized by line roughness caused by semicircular features (whose diameter is equivalent to the channel length) that are induced by the circular shape of the laser spot engraving on the sample. The surface of PLGA bio-scaffolds exhibits characteristic circular cavities of two-micrometer diameter that form during the solvent casting procedure in air. The cavities can be observed in both regions of the AFM picture and are not affected either by the metal deposition or by the laser ablation. The Ti/Au electrodes show excellent adhesion to the PLGA substrate and no delamination is induced by solvents, mechanical stress or long time degradation.

Ten monolayers (15 nm) pentacene thin film was grown as described in the previous section. Patterned metal and semiconductor layers were demonstrated stable in pure water, saline water and cell culture medium. No delamination was observed in operational conditions. The EGOFET obtained is largely biodegradable as most of the mass consists of the scaffold. Patterned non-biodegradable films on the surface (metals and pentacene) contribute a negligible fraction of the total mass. Indeed, the biodegradable substrate composes the 98.9 % in weight of the freestanding film.

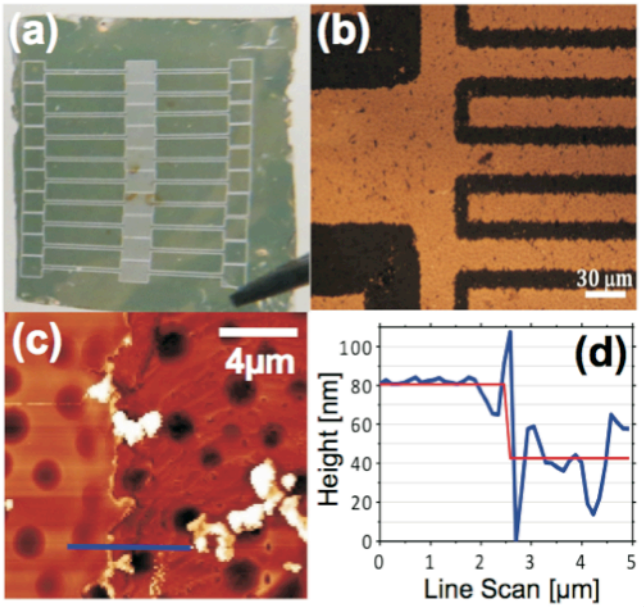

Figure 4 Photo of PLGA obtained as a free standing film on which 10 pairs of interdigitated electrodes are patterned by scanning laser ablation technique; **(b)** optical microscopy image of the electrodes; AFM image **(c)** of the boundary between transistor channel area (on the right) and the electrode (on the left) and **(d)** a representative profile across the blue line in (c). Reprinted with permission from Ref. [13]

3.3.1 EGOFET on PLGA: Electrical Performances

The gate used for the electrical characterization is a Pt wire immersed in pure water confined by means of a PDMS pool pressed on the device surface. A scheme of the EGOFET is depicted in **Figure 5**.

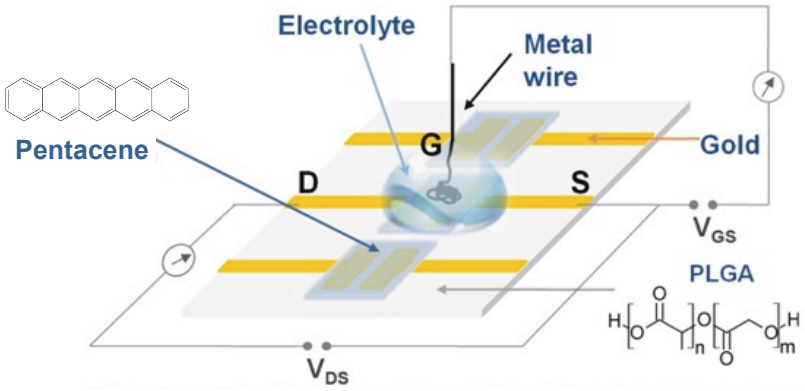

Figure 5 Pentacene based EGOFET fabricated on PLGA, a wiring diagram

Typical transfer and output curves were reported in **Figure 6**. The measurements demonstrate typical FET response and stable low-voltage operation, with saturation of drain current and almost absence of hysteresis. The transfer scan shows modulation of the drain current by more than one order of magnitude with a leakage current I_G which remains one order of magnitude lower. The charge carrier mobility μ = (8.7± 1.5) 10^{-5}cm^2/(Vs) and threshold voltage V_{th} = 0.14 ± 0.11 V are extracted. The transconductance in saturation regime of these devices is 0.8 ± 0.1 µS, that is one order of magnitude lower with respect the one obtained for similar devices on silicon wafers and with gold electrodes patterned by photolithography and lift-off[11,14]

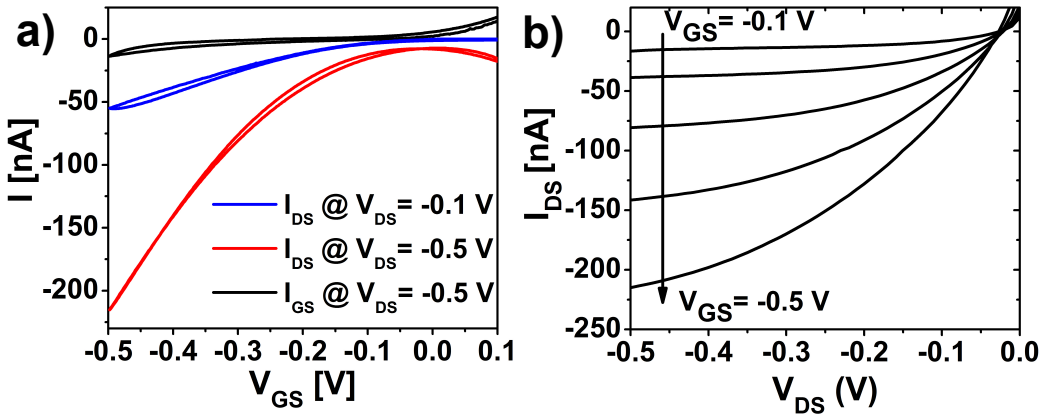

Figure 6 Transfer **(a)** and output **(b)** characteristics of the EGOFET fabricated on PLGA. Electrolyte is pure water.

As already mentioned in chapter Chapter 2, extracellular detection of bioelectric signals requires potentiometric sensitivity in the µV range. In order to demonstrate it, the EGOFET was operated at constant V_{GS} and V_{DS} (both -0.5 V) and the drain current was monitored in time. Small potential pulses were applied for 1 s at the gate electrode. The resulting changes in drain current are depicted in **Figure 7** after polynomial correction for drain current drift. Potential changes down to 100 µV still lead to a detectable change in drain current above the background noise (I_{rms} = 30 pA). The current spikes at the beginning and end of the potential

pulse result from capacitive currents due to the altered charge density in the EDL. Stable performance in water for a few hours was achieved.

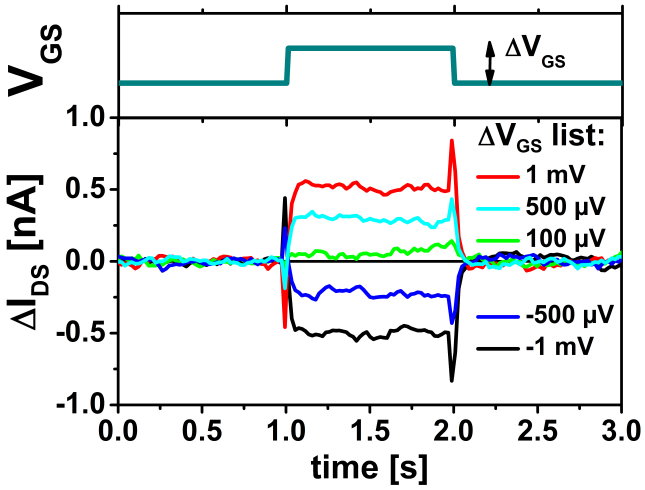

Figure 7 Potentiometric sensing experiment showing high sensitivity of the drain current to small potential pulses, ΔV_{GS}, applied to the liquid gate electrode. Reprinted with permission e from Ref. [13]

Devices fabricated with the direct ablation process were also tested in saline water but electrical performance decreases dramatically. In particular, as soon as water is replaced with saline solution (e.g.: sodium chloride, phosphate buffer solution or cell culture medium) the drain current drops while leakage current rises. This unexpected phenomenon was not deeply investigated. Our hypothesis resides on the formation of electrochemically active species induced by direct ablation onto PLGA.

3.4 Conclusions on EGOFET on PLGA by Direct Fabrication

The first EGOFET fabricated onto a biodegradable scaffold exhibits good performance in pure water. Although this technique is serial and hence throughput limited, it is suitable for prototyping implantable medical

applications. As will be shown in the following chapters: the process is simple, it can be applied to a variety of polymeric substrates and avoids contact with masks and exposure to solvents. This makes possible to manufacture personalized devices. The EGOFET is suitable for potentiometric sensing in pure water with a detection limit of 100 μV range. These characteristics, in combination with the verified *in vitro* biocompatibility of pentacene semiconductor films[15,16], would make the EGOFET a promising device for non-invasive recordings of neuronal electric activity. The main issue to be solved is the lack of stability in electrophysiological environment.

3.5 EGOFET on PLGA by Inverse Fabrication

The second proposed technique is based on an inverse fabrication (IF) bypassing the usage of photolithographic solvents and direct ablation of the metal onto the scaffold. The process relies on the capability of transferring a pattern from a sacrificial layer, which has fewer constraints, onto the desired substrate, which is then cast atop. Sacrificial layers have been exploited as protective layers or as temporary adhesive layers between the final substrate film and a stiff carrier to enable handling[17–19]. The novelty here is related to the usage of the sacrificial layer for the fabrication and transfer of gold patterns onto biomaterials.

The requirement set by the technique is that the sacrificial layer and the biopolymer must have orthogonal solubility. Since PLGA is soluble in organic solvents, we chose a well known water-soluble polymer, poly(acrylicacid), PAA, as a sacrificial layer[18]. It is transparent and it can be processed by spin coating or drop casting onto solid carriers, such as glass slides or silicon wafers (**Figure 7a**). The active metal layer is deposited on PAA (**Figure 7a**) and patterned by means of laser ablation(**Figure 7b-c**). Doing so, one can easily generate a metal pattern and design electrodes. The next step includes the transfer of the metal

pattern onto the PLGA film. The metallic layer is sandwiched between the sacrificial layer and the PLGA that is solvent cast on top (**Figure 7d**). When the solvent is evaporated, the whole sandwich structure is immersed in water (**Figure 7e**). PAA is solubilized and the pattern adheres to PLGA (**Figure 7f**), which is released as freestanding scaffold (**Figure 7g**). The great advantage of this technique is that the processing has a very low impact on the final biopolymer scaffold since the metal pattern is already formed prior to the formation of the PLGA. In this way, one can avoid the detrimental impact of solvents on the biodegradable polymer. The detailed protocol used for the fabrication of an EGOFET is described below.

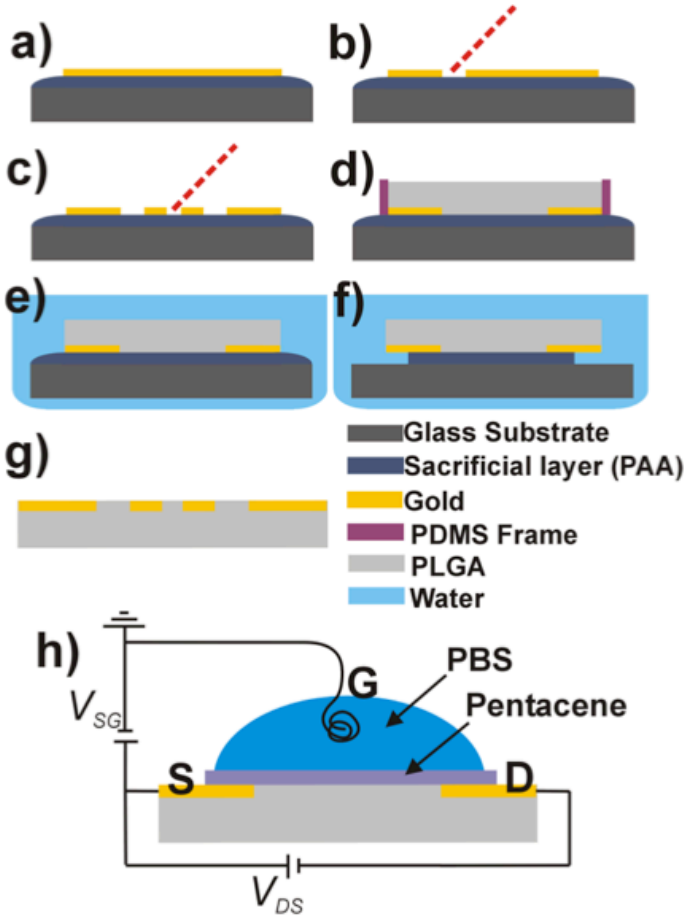

Figure 8 From **a)** to **g)** is depicted the fabrication sequence of the gold pattern on PAA sacrificial layer and the transfer onto the PLGA film. **h)** Schematic cross section of the EGOFET and its wiring diagram.

Microscopy glass slides are cleaned by sonication in acetone and isopropanol (both ultra-pure grade) for 10 minutes each. Further rinsing with isopropanol is followed by drying under N_2 stream. The glass slides are then functionalized with (3-aminopropyl)-trietoxysilane (APTES) (Sigma Aldrich, 99%) 1 mM in ethanol for 45 minutes. Rinsing with ethanol and purge under N_2 stream are the final steps prior to the spin coating of a PAA (Sigma Aldrich, 35% wt. in H_2O, MW = 100 kDa) films. PAA solution is diluted in water to get a 5% solution, which is spun at 500 rpm for 3 s and 2000 rpm for 20 s. The glass is then baked 20 min at 140 °C and cooled at RT prior to the spin coating of a second layer of a neutralized (by means of NaOH aliquots) 3% PAA at 500 rpm for 3 s and 1800 rpm for 20 s. A second baking for 20 min at 120 °C is performed. The thickness of the sacrificial layers obtained with this method on microscopy glass slides was measured with a Veeco Dektak 3ST Surface Profiler. The thickness measured is 500 nm. Au films are thermally evaporated in a high vacuum chamber. The thickness of gold can vary from 25 nm to 100 nm depending on the final application. The sample is kept far (55 cm) from the incandescent hot tungsten boat in order to avoid surface overheating to occur. To obtain a gold pattern several different strategies can be adopted. PAA is a water-soluble polymer, which means it is not compatible with most photolithographic processes followed by local chemical etching. The ScribaR is used to perform the local removal of gold[13]. This process, even if highly controlled by fine optimization of ablation parameters (frequency, power, mark speed, pulse width) induces strong local heating and roughening of the surface, especially when directly applied on biopolymers, which have low melting points. To circumvent these issues, the laser ablation is performed onto the sacrificial layer. For a 50 nm thick gold film on PAA the parameters adopted for the ablation were: 150 mW with pulse width of 10 ns and 22000 Hz repetition rate. The biocompatible and biodegradable PLGA film is then fabricated on top of the gold patterned on PAA casted on the microscopy glass slide. 100 µL of a 5% PLGA solution in dichloromethane

is cast inside a 1 x 1 cm^2 PDMS frame to confine the liquid. After the drying process at 50 °C for 3 hours, the resulting film is 20 μm thick. The whole microscopy glass slide is then immersed in ultrapure water to induce PAA dissolution. This step requires different timing mainly depending on the area of the PLGA casted films. For a 1 x 1 cm^2 area, generally one can obtain a freestanding film within 25 minutes. While the PAA dissolves in water, gold adheres to the PLGA scaffold. The adhesion of the metal film to the biodegradable polymer is comparable to the adhesion of the metal film directly thermally evaporated with the addition of titanium adhesive layer. We suppose this is due to gold embedding into the PLGA film, which is then formed around the metal structures. The resulting thin pattern is protected and strongly adhered to the final substrate, as desired.

Before any further step, the substrate has to be abundantly rinsed with pure water in order to remove all PAA traces and obtain a PLGA/Au clean surface. The film can be dried in vacuum or in the oven for 4 hours at 40 °C.

The same fabrication strategy can be adopted also on silicon wafers. We have chosen to use microscopy glass slides as they are cheaper and can be used as disposable carriers. Furthermore, transparency of glass substrates represents an advantage during the fabrication since it allows the alignment and positioning to occur easily. When silicon wafers are used as carriers, silanization by means of APTES is not required since its surface energy allows the PAA film to be homogeneously spun.

Once we have obtained the freestanding biodegradable scaffold, the next step is to fabricate the EGOFET devices. The geometry of the transistor can be systematically designed by the parameters used during the ablation process. For our devices, the gold patterning generates interdigitated electrodes with a 16800 μm a channel width and 15 μm

channel length to define a W/L of 1120. By refining the ablation parameters one can further reduce the channel length down to 10 μm. For obtaining different patterning in terms of shapes and dimensions one can easily change the CAD (computer assisted drawing) file, which defines the movement of the stage under the laser beam. The CAD file contains straight or circular lines, which correspond to regions in where material has to be removed. The interdigitated electrodes, transferred on the formed PLGA film (**Figure 9a**, **b** and **c**), will play the role of source and drain of the final transistor architecture. The resulting PLGA surface, template on the PAA film, results to an extremely flat surface with a roughness lower than 2 nm. 10 monolayers of pentacene (sublimated in a high vacuum chamber with a deposition rate of 7 Å/min) define the transistor channel. **Figure 9 d** reports an AFM image of the boundary between transistor channel and gold electrode.

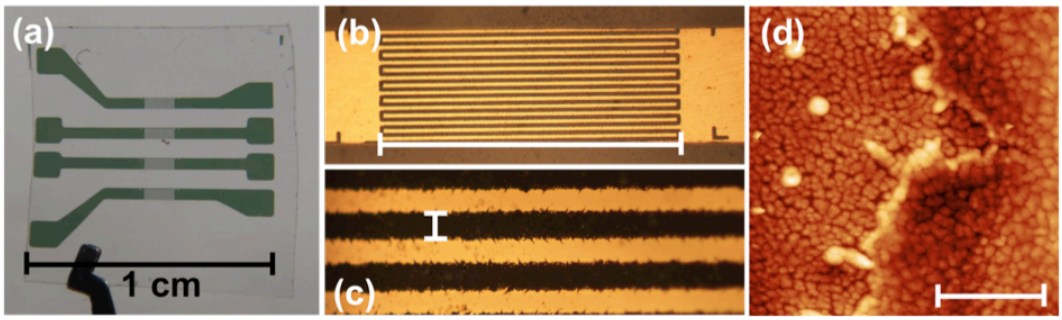

Figure 9 a) Photo of a free standing 20 μm-thick 1x1 cm^2 test pattern with four pairs of interdigitated gold electrodes. **b)** and **c)** are optical microscopy images of the interdigitated electrodes; rulers are 1.2 mm and 15 μm, respectively. **d)** AFM of the boundary between transistor channel (left) and gold electrode (right) coated with sublimed pentacene, the scale bar is 2 μm.

3.5.1 EGOFET on PLGA by IF: Electrical Characterization

To complete the EGOFET architecture, a platinum wire is immersed in water or phosphate buffer solution (PBS) confined on the device active area with a PDMS pool sealed to the biodegradable scaffold

(**Figure 8h**). The platinum wire serves as the gate electrode of the transistor. **Figure 10a** shows a typical transfer curve obtained in saturation regime (V_{DS}=-0.5 V). The characteristics show field effect transistor behaviour with very low hysteresis in PBS. The charge carrier mobility $\mu=(2.4\pm0.7)10^{-4}$ $cm^2/(Vs)$ and a threshold voltage V_{th}=0.13 ± 0.09 V are extracted. In saturation regime, transconductance of these devices is 3.2 ± 0.7 µS that is three times higher then devices made with direct ablation on PLGA.

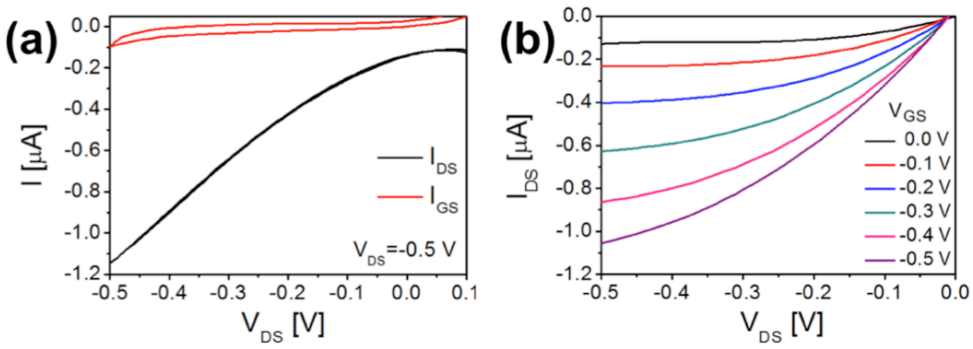

Figure 10 Electrical characteristics of the EGOFET/PLGA acquired in PBS. **a)** Transfer curve obtained in saturation regime. **b)** Output curves at different gate voltages.

The typical output curve in PBS is reported in **Figure 10b**. It shows good drain current modulation at different gate voltages. A low contact resistance can be noted. The device performance is stable for hours in the working environment.

3.6 Conclusions on EGOFET on PLGA by IF

In conclusion, this second technique for the fabrication of gold electrodes on biocompatible and biodegradable material offers several advantages. The surface roughness is lower and the damage induced by heating the PLGA film is highly reduced. This process is versatile and can be applied to various polymers produced by casting. The crucial step in

the processing is the ability to pattern metal electrodes on a sacrificial layer and transfer them onto the biopolymer. The performances of the EGOFET, with respect to direct ablation technique, are improved and the device is also demonstrated is physiological environment.

Bibliography

(1) Angione, M. D.; Pilolli, R.; Cotrone, S.; Magliulo, M.; Mallardi, A.; Palazzo, G.; Sabbatini, L.; Fine, D.; Dodabalapur, A.; Cioffi, N.; *et al.* Carbon Based Materials for Electronic Bio-Sensing Bio-Sensing Represents One of the Most Attractive Applications of Carbon. *Mater. Today*. **2011**, *14*, 424–433.

(2) Zhong, Y.; Bellamkonda, R. V. Biomaterials for the Central Nervous System. *J. Roy. Soc. Interface* **2008**, *5*, 957–975.

(3) Irimia-Vladu, M.; Sariciftci, N. S.; Bauer, S. Exotic Materials for Bio-Organic Electronics. *J. Mat. Chem.* **2011**, *21*, 1350–1361.

(4) Hassler, C.; Boretius, T.; Stieglitz, T. Polymers for Neural Implants. *J. Polym. Sci. Part B Polym. Phys.* **2011**, *49*, 18–33.

(5) Lee, J. Y.; Bashur, C. a; Goldstein, A. S.; Schmidt, C. E. Polypyrrole-Coated Electrospun PLGA Nanofibers for Neural Tissue Applications. *Biomaterials* **2009**, *30*, 4325–4335.

(6) Luis, A. N. A. L.; Rodrigues, J. M.; Amado, S.; Raimondo, S.; Fregnan, F.; Lopes, M. A.; Mauri, A. N. A. C.; Geuna, S.; Vareja, A. S. P. PLGA/90/10 and Caprolactone Biodegradable Nerve Guides for the Reconstruction of the Rat Sciatic Nerve. *Microsurgery* **2007**, 125–137.

(7) Makadia, H. K.; Siegel, S. J. Poly Lactic-Co-Glycolic Acid (PLGA) as Biodegradable Controlled Drug Delivery Carrier. *Polymers (Basel).* **2011**, *3*, 1377–1397.

(8) Jain, R. a. The Manufacturing Techniques of Various Drug Loaded

Biodegradable Poly(lactide-Co-Glycolide) (PLGA) Devices. *Biomaterials* **2000**, *21*, 2475–2490.

(9) Yoo, J. Y.; Kim, J. M.; Seo, K. S.; Jeong, Y. K.; Lee, H. B.; Khang, G. Characterization of Degradation Behavior for PLGA in Various pH Condition by Simple Liquid Chromatography Method. *Biomed. Mater. Eng.* **2005**, *15*, 279–288.

(10) Shehu, A.; Quiroga, S. D.; D'Angelo, P.; Albonetti, C.; Borgatti, F.; Murgia, M.; Scorzoni, A.; Stoliar, P.; Biscarini, F. Layered Distribution of Charge Carriers in Organic Thin Film Transistors. *Phys. Rev. Lett.* **2010**, *104*, 246602.

(11) Cramer, T.; Chelli, B.; Murgia, M.; Barbalinardo, M.; Bystrenova, E.; de Leeuw, D. M.; Biscarini, F. Organic Ultra-Thin Film Transistors with a Liquid Gate for Extracellular Stimulation and Recording of Electric Activity of Stem Cell-Derived Neuronal Networks. *Phys. Chem. Chem. Phys.* **2013**, *15*, 3897–3905.

(12) Voskerician, G.; Shive, M. S.; Shawgo, R. S.; Recum, H. Von; Anderson, J. M.; Cima, M. J.; Langer, R. Biocompatibility and Biofouling of MEMS Drug Delivery Devices. *Biomaterials* **2003**, *24*, 1959–1967.

(13) Campana, A.; Cramer, T.; Greco, P.; Foschi, G.; Murgia, M.; Biscarini, F. Facile Maskless Fabrication of Organic Field Effect Transistors on Biodegradable Substrates. *Appl. Phys. Lett.* **2013**, *103*, 073302.

(14) Cramer, T.; Kyndiah, A.; Murgia, M.; Leonardi, F.; Casalini, S.; Biscarini, F. Double Layer Capacitance Measured by Organic Field Effect Transistor Operated in Water. *Appl. Phys. Lett.* **2012**, *100*, 143302.

(15) Bystrenova, E.; Jelitai, M.; Tonazzini, I.; N. Lazar, A.; Huth, M.; Stoliar, P.; Dionigi, C.; Cacace, M. G.; Nickel, B.; Madarasz, E.; *et al.* Neural Networks Grown on Organic Semiconductors. *Adv. Funct.*

Mater. **2008**, *18*, 1751–1756.

(16) Tonazzini, I.; Bystrenova, E.; Chelli, B.; Greco, P.; Stoliar, P.; Calò, A.; Lazar, A.; Borgatti, F.; D'Angelo, P.; Martini, C.; *et al.* Multiscale Morphology of Organic Semiconductor Thin Films Controls the Adhesion and Viability of Human Neural Cells. *Biophys. J.* **2010**, *98*, 2804–2812.

(17) Cheung, K. C.; Renaud, P.; Tanila, H.; Djupsund, K. Flexible Polyimide Microelectrode Array for in Vivo Recordings and Current Source Density Analysis. *Biosens. Bioelectron.* **2007**, *22*, 1783–1790.

(18) Linder, V.; Gates, B. D.; Ryan, D.; Parviz, B. a; Whitesides, G. M. Water-Soluble Sacrificial Layers for Surface Micromachining. *Small* **2005**, *1*, 730–736.

(19) Ceyssens, F.; Van Kuyck, K.; Vande Velde, G.; Welkenhuysen, M.; Stappers, L.; Nuttin, B.; Puers, R. Resorbable Scaffold Based Chronic Neural Electrode Arrays. *Biomed. Microdevices* **2013**, *15*, 481–493.

chapter 4

Organic Electrochemical Transistor Fabricated on Biodegradable Scaffold: Electrocardiographic Recording

The fabrication of an Organic Electrochemical Transistor (OECT) on a biodegradable scaffold is described. The fabrication process requires deposition of a gold film through a shadow mask and the deposition of semiconductor followed by a dry-etching patterning. Electrical characteristics are comparable to state of the art OECTs fabricated on rigid substrates. We used the small area flexible OECT device for the recording of electrocardiogram (ECG). In terms of signal-to-noise ratio, the biodegradable imperceptible sensor is comparable to silver faradaic electrodes.

4.1 Introduction

In Chapter 3 we demonstrated the possibility to fabricate Electrolyte Gated Organic Field Effect Transistors (EGOFETs) based on pentacene on a poly(lactic-co-glycolic), (PLGA) substrate. Albeit the configuration is in principle suited for implants, the nature of pentacene and its long-term stability in a physiological environment appear to be critical features. In an effort to overcome these, we investigated other semiconducting materials, which could replace pentacene in a fully stable and mechanically robust device. The list of biocompatible semiconductors which can be sublimed or processed in water and which are biocompatible and guarantee long term performances is not extensive. The most interesting results were obtained with (poly(3,4-ethylenedioxythiophene):polystyrene sulfonate) PEDOT:PSS as semiconductor channel in a transistor operated in depletion (as opposed to accumulation) mode. Fabrication process, which allows us to pattern the devices on a bioresorbable PLGA scaffold, is simple. The prototype device combines optimized materials properties for implantation such as flexibility, and bioresorption with transparency (useful for *in vitro* assessment) and with excellent potentiometric response. Like for the fabrication of the EGOFET, two criticalities must be overcome to get an OECT onto PLGA: i) micro-structuring of PEDOT:PSS has to be achieved without solvent-based lithographic procedures as PLGA is highly soluble and ii) surface chemistry has to be optimized to avoid delamination of the swelling PEDOT:PSS. The results of this work are published in reference [1].

4.2 Easy Fabrication of an OECT onto PLGA

The 20 μm thick homogeneous and transparent PLGA substrate was prepared by solvent casting (5% weight solution in chloroform) as described in Section 3.3. By tightly controlling environmental conditions, films could be prepared with an averaged mean roughness of 2 nm, as determined by AFM measurements. In our experimental setting, no visual

degradation of the film could be observed on the day time scale at which measurements were undertaken. On top of the PLGA layer, metal source and drain contacts were deposited by evaporation of gold (30 nm) through a shadow mask (L = 30 µm, W = 1000 µm) at a pressure of 10^{-6} mbar. Next, PEDOT:PSS was spin cast on the substrate and thermally annealed (50 °C, 24 h) to form ca. 200 nm thick layers. The incorporation of an epoxy cross-linker and, more importantly, pH neutrality of the aqueous PEDOT:PSS suspension to avoid pH-catalyzed hydrolysis of the PLGA scaffold and subsequent delamination were found to be crucial for adhesion on the PLGA scaffold. **Figure 1a** shows optical properties and conformability of the transistor fabricated on the transparent scaffold onto curved human tissues.

Patterning of PEDOT:PSS was achieved by a plasma assisted dry etching process (20 s, 150 W, 600 mTorr, O_2:CF_4 = 1:1). The transistor regions were protected through pressing a PDMS, polydimethylsiloxane, elastomeric stamp on their surface. In the **Figure 1b** a micrograph (after etching) of the active transistor area with a channel length of 30 µm is reported. On the source and drain electrodes, a darker color region evidences the presence PEDOT:PSS.

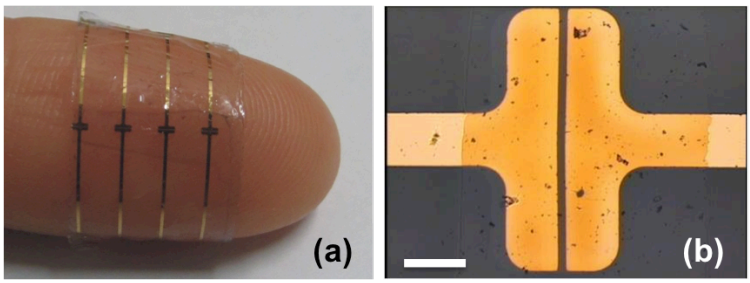

Figure 1 a) Picture of the device showing its transparency and conformability to human fingertip. **b)** Optical microscopy image of an individual transistor. The darker color of the electrodes indicated the area on which PEDOT:PSS is present. Scale bar 200 µm. Reprinted with permission from [1]

4.3 OECTs Fabricated on PLGA: Electrical Performances

To characterize the OECT, the channel region was contacted by aqueous phosphate buffer solution (0.1 M PBS, pH 7) in which a platinum or silver wire was immersed and used as the gate electrode (**Figure 2**).

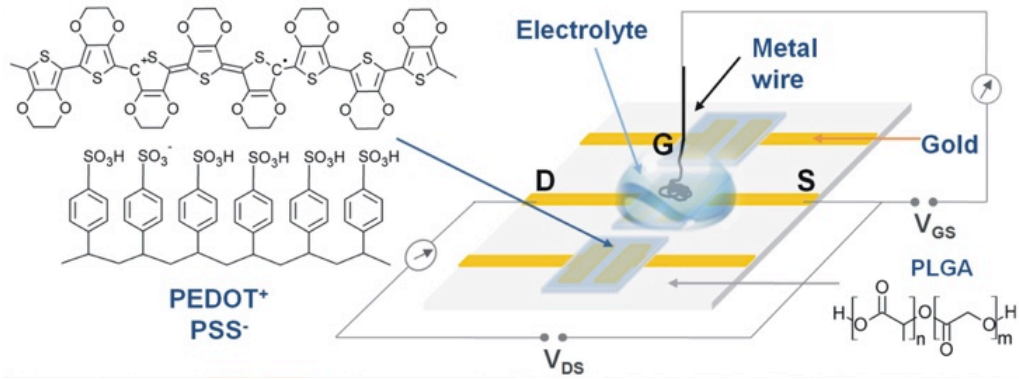

Figure 2 OECT structure and materials. PEDOT:PSS is patterned as the active layer on the bioresorbable PLGA thin film and contacted by gold source and drain electrodes. The structure is gated by the electronic potential applied to the aqueous electrolyte via a metal wire.

Stable low voltage operation is achieved as in state-of-the-art OECTs. As in normal thin film transistors the output curves in **Figure 2b** exhibit linear behavior at low drain potentials while current saturation is observed when the drain potential is increased. As the transistor works in depletion mode, reduction of the transistor current occurs when setting the electrolyte to positive potential with respect to the PEDOT:PSS channel. In this way, mobile positive carriers in the p-type semiconducting polymer PEDOT are reduced and cations from solutions migrate into the film to counterbalance the negative charges of the polyanionic dopant PSS. As charge modulation affects the whole volume of the film, the transistor shows a huge interfacial capacitance of ~500 μF cm^{-2} (**Figure 2a**) in the

low frequency limit and a large transconductance of 3.2 ± 0.5 mS at V_{DS} = -1 V as extracted from the transfer curve. The Faradaic leakage currents during transistor characterization remain more than three orders of magnitude below I_{DS}.

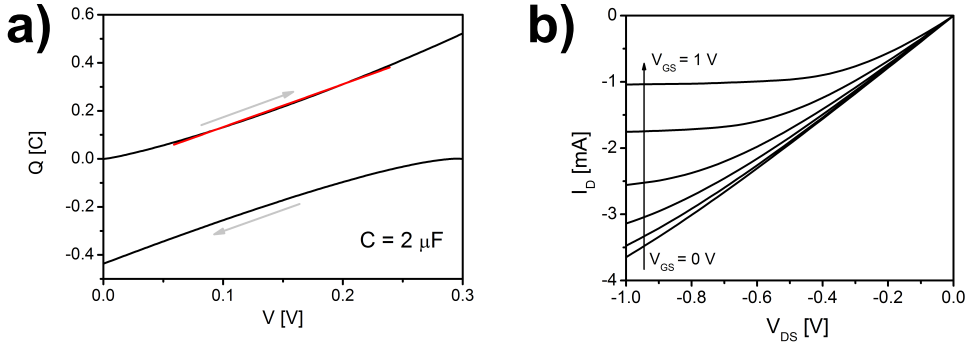

Figure 2 a) Determination of the PEDOT:PSS layer capacitance. The capacitive structure contains the PEDOT:PSS area (4 x 10^{-3} cm^2) contacted by gold leads, the PBS aqueous electrolyte and a Pt wire. The scan rate of the potential V was 100 mV/s. A linear fit (red line) results in specific capacitance c ~ 500 µF/cm^2. **b)** Output characteristics recorded in PBS with a Pt wire as a gate electrode. Reprinted with permission from Ref. [1].

Next, we tested the influence of conforming the device to non-planar surfaces on the electrical performance (**Figure 3**). **Figure 3c** illustrates a transfer measurement (dashed line) obtained after stressing the device by bending it down to curvature radii of 80 µm **Figure 3a** and **b** and reporting it to planarity. The observed variations were well within the range of the standard deviation of measurements on unstressed devices (grey areas). Also, mechanically stressing the device by attaching it to curved biological surfaces like human skin did not result in device failure. Even in cases of extreme stressing like crumpling of the device with repeated pressing on folding edges, no dewetting or disruption of the polymeric layer could be observed, although devices did start to show failure due to cracks in the gold electrodes.

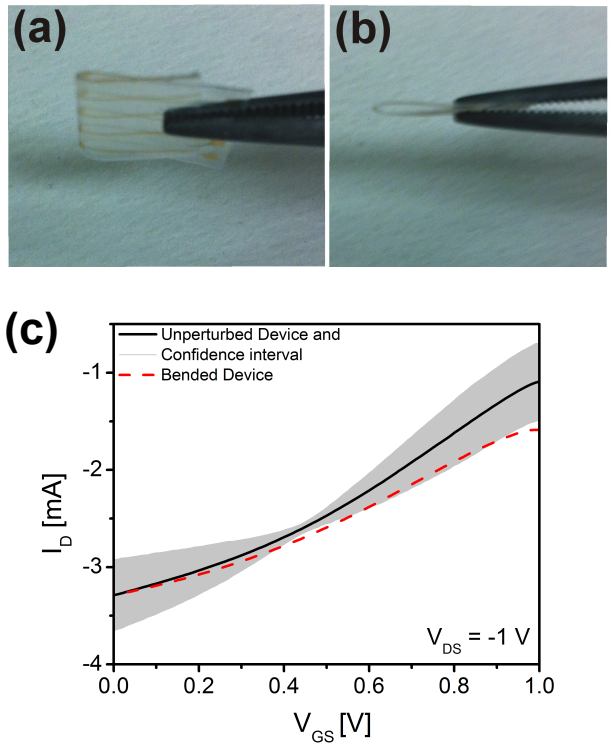

Figure 3 (a) and **(b)** report representative pictures showing the mechanical stressing of the device by bending. The transistor region was deformed with curvature radii down to 80 µm. **(c)** Transfer characteristics of unperturbed devices (black being the mean curve and the grey area indicating the experimental variation) and after bending at a curvature radius of 80 µm. Reprinted with permission from Ref. [1].

In order to assess the devices as a potentiometric sensor, we operated the transistor at constant gate and drain potential (V_{GS}= 0.3 V; V_{DS}= -0.3 V) in electrolyte solution and sampled the drain current. Application of small potential pulses to the gate resulted in characteristic changes in drain current, depicted in **Figure 4a**. High sensitivity combined with operational stability is demonstrated by the clear detection of potential changes as low as ΔV_{GS}= 50 µV on seconds time scale. In order to define the response time of the device we applied a larger potential pulse (ΔV_{GS}= 0.1 V) and sampled the current at a rate of 10 kHz. The resulting response is shown in **Figure 4b** and follows the exponential behavior of an RC circuit with a time constant of τ = 1.5 ms. In terms of

performances these devices are comparable to state of the art OECTs fabricated onto glass or other non bioresorbable scaffolds [2–4].

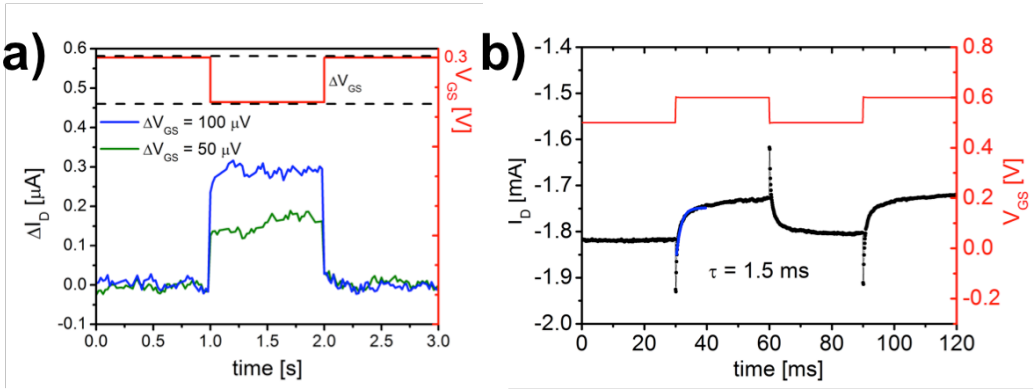

Figure 4 a) Potentiometric sensitivity tested by monitoring the drain current variation as a consequence of potential changes as small as 50 μV applied to the gate. **b)** Fast response of the drain current (V_{DS} = -0.5 V) to a gate voltage variation of 0.1 V. Reprinted with permission from Ref. [1].

4.4 ECG Recording by means of an OECT on PLGA

In order to demonstrate the potentiometric recording capabilities of the bioresorbable OECT in a medically relevant setting, we recorded a human ECG. The ECG signal originates in the muscular tissue of the heart whose contraction is initiated by an influx of cations in the cardiac cells causing cell depolarization. The ordered progression of contraction throughout the heart muscle gives rise to a macroscopic ionic current wave that spreads throughout the body during each heart beat cycle leading to tiny potential changes on the skin due to the finite resistance of the body's tissue. By attaching electrodes, the signal can be recorded by a sensitive potentiometer. From the recorded shape one can extract information about the pulse rate, pulse regularity as well as heart dimensions and the presence of damage. Standard Ag/AgCl based electrodes (Euro ECG Electrodes, Fiab, Florence) establish a Faradaic contact to the skin. In the case of an OECT based ECG sensor, the recording occurs by attaching the transistor's exposed PEDOT:PSS

channel directly to the skin. We used electroconductive gel, as usual in ECG recordings, to promote adhesion and to reduce the skin's impedance. In that way, the skin replaces the role of the gate. The skin potential changes with respect to a ground contact and leads to transient fluctuations of the drain current.

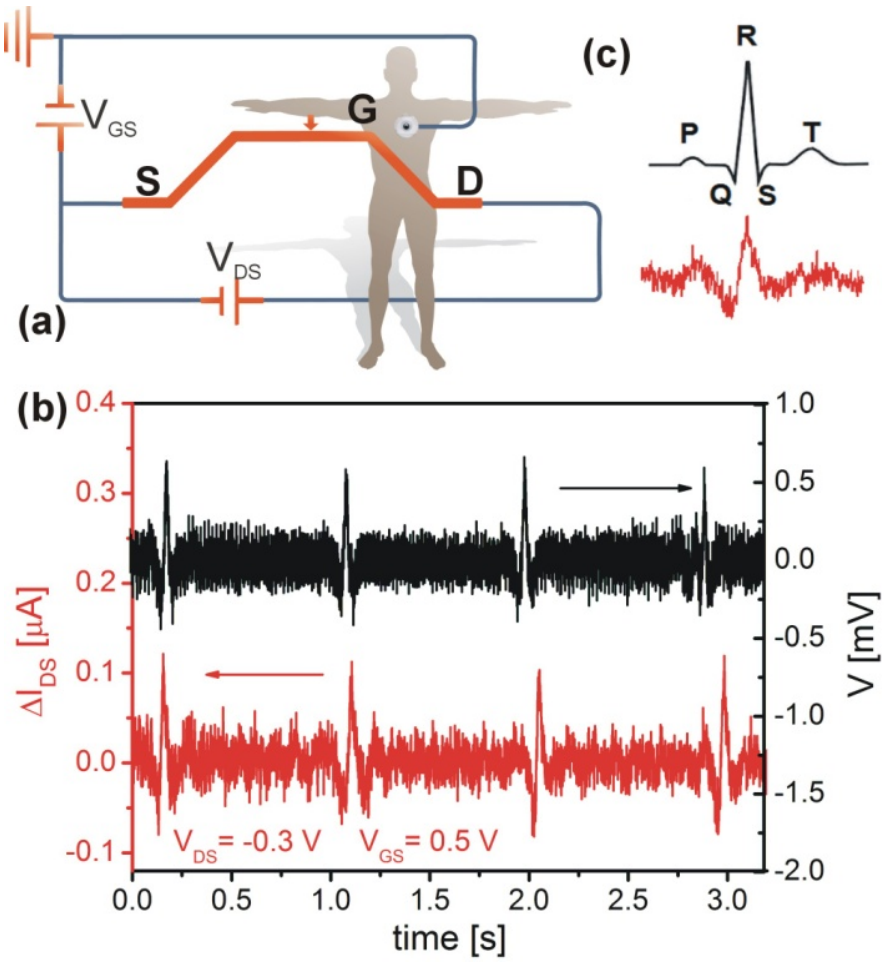

Figure 5 ECG recording with a bioresorbable OECT operated in direct contact with the skin. **a)** Wiring diagram of the experiment. **b)** Measured drain current trace (red) as obtained during ECG recording (V_{SG} = 0.5 V, V_{SD} = -0.3 V) and comparison to a normal potentiometric recording with standard disposable leads (black). **c)** Enlarged transistor ECG trace of a single cardiac cycle and comparison to a schematic textbook example. Reprinted with permission from Ref. [1]

We realized a cross-thoracic recording by placing the ground contact (acting as gate) on the chest and the OECT on the forearm as shown in **Figure 5a**. In order to measure in a transistor regime where transconductance is high and leakage current sufficiently low, we set the transistor channel to a potential of V_{GS} = 0.5 V with respect to the grounded body while monitoring the drain current at V_{SD} = -0.3 V. I_D was sampled at a rate of 1 kHz. Noise was removed according to standard digital procedures (Matlab®, The MathWorks Inc) by applying a high pass filter (cutoff at 3 Hz) and notch filters (50 Hz and higher harmonics). The resulting current trace (red line, **Figure 5b**) contains the typical spikes of the heartbeat with an amplitude of ~100 nA in comparison to spikes of 500 µV as measured with the traditional potentiometric recording (black line, **Figure 5b**). Although the measurements were done with ordinary lab equipment, the signal-to-noise ratio of the bioresorbable transistor is already comparable to the recording based on the traditional Faradaic electrodes. A closer look to an isolated OECT signal **Figure 5c** and comparison to an idealized ECG signal as found in cardiology textbooks shows that its quality is sufficient to extract some fine structure that allows one to characterize the timing between the different sub-waves.

4.5 Conclusions

We demonstrated conformable and transparent transistor devices fabricated on a fully resorbable bioscaffold. The device fabrication relies on a simple process which allows patterning of active areas of the conductive polymer PEDOT:PSS contacted by gold electrodes on the bioscaffold. The resulting structure combines biocompatibility and biodegradability with excellent electronic properties for fast and sensible potentiometric sensing in aqueous conditions. The fast ion-to-electron exchange which is crucial for bioelectric interfaces results from the intrinsic materials properties of the PEDOT:PSS layer. By optimizing the

layer thickness and the channel geometry we achieve the sensing of signals down to a few tens of microvolts at timescales of a few milliseconds. As a medically relevant bioelectric recording device, we applied the transistor in electrocardiography and show a signal-to-noise ratio that is comparable to the one of standard Faradaic electrodes. These results highlight the feasibility of realizing simple organic bioelectric interfaces on implantable bioscaffolds which would allow the recording of signals from muscular or nervous tissue to monitor health status, or which could provide electrical stimulation to influence the tissue's activity. Resorption of the bioscaffold leads to a finite lifetime of the implant in the body. This opens the possibility to avoid the removal of the devices from the regenerated tissue in future applications.

Bibliography

(1) Campana, A.; Cramer, T.; Simon, D. T.; Berggren, M.; Biscarini, F. Electrocardiographic Recording with Conformable Organic Electrochemical Transistor Fabricated on Resorbable Bioscaffold. *Adv. Mater.* **2014**, *26*, 3874–3878.

(2) Yaghmazadeh, O.; Cicoira, F.; Bernards, D. a.; Yang, S. Y.; Bonnassieux, Y.; Malliaras, G. G. Optimization of Organic Electrochemical Transistors for Sensor Applications. *J. Polym. Sci. Part B Polym. Phys.* **2011**, *49*, 34–39.

(3) Tarabella, G.; Santato, C.; Yang, S. Y.; Iannotta, S.; Malliaras, G. G.; Cicoira, F. Effect of the Gate Electrode on the Response of Organic Electrochemical Transistors. *Appl. Phys. Lett.* **2010**, *97*, 123304.

(4) Khodagholy, D.; Doublet, T.; Quilichini, P.; Gurfinkel, M.; Leleux, P.; Ghestem, A.; Ismailova, E.; Hervé, T.; Sanaur, S.; Bernard, C.; *et al.* In Vivo Recordings of Brain Activity Using Organic Transistors. *Nat. Commun.* **2013**, *4*, 1575.

chapter 5

In vitro Extracellular Electrical Stimulation with Biodegradable OECTs

In vitro electrical stimulation (ES) of primary neurons and macrophages is presented. In this chapter a complete description of the fabrication of fully biocompatible and highly biodegradable Organic Electrochemical Transistors (OECTs) to be interfaced to cell lines is provided. The complete experimental setup for the application and monitoring of the effective electrical stimulation is established. An efficient and safe protocol for extracellular stimulation is developed and adopted on primary neurons and it is repeated onto macrophages. Relevant biological results are extracted that demonstrate the importance of ES not only onto excitable cells but also on cells of the immune system. Furthermore, the versatility of the OECT based stimulation technique allows the investigation of the biochemical mechanisms that lead to ES-induced cells modifications. Stimulation paradigm toward *in vivo* application is optimized.

5.1 Introduction

Towards the fabrication of the active multifunctional device and its implantation *in vivo*, *in vitro* experiments on selected cell lines are necessary. *In vitro* experiments represent a key step in the understanding of complex mechanisms, which will take place in living organisms. Indeed, they provide strong indications about the effect of induced specific stimuli (chemical, electrical, mechanical) delivered to specific cell lines. The stimuli/therapies are not exclusively delivered to the target cells (e.g. neurons). Indeed, the whole biological environment in vicinity to the stimulation will be affected.

As reported in Chapter 1, after SCI neurons are strongly damaged and their functionality is strongly compromised. ES tested in various different configurations appears to positively affect their plasticity and networking. The approach we propose is based on extracellular stimulation performed by means of OECTs fabricated onto a biodegradable scaffold. Since it is a novel architecture for stimulation and recording, its validation is necessary. In order to demonstrate both materials compatibility and efficacy of ES, *in vitro* experiments on primary neurons, along with cell viability assays, were performed.

The main issue to be solved is to find OECT operation allowing effective extracellular stimulation of primary neurons. Optical imaging of intra-cellular variations of Ca^{2+} concentrations is the technique adopted to independently assess the efficacy of OECT stimulation in the modulation of neural activities. ES modulates ions flow through the cell membrane and induced action potentials (APs) onto excitable cells. The opening and closing of voltage gated ions channels (VGICs), which are specific for K^+, Na^+ and Ca^{2+}, are responsible for the variations in concentration of each species during resting, depolarization and repolarization steps. When resting, intracellular Ca^{2+} ion concentration is low (10-100 nM) while when excited calcium intake is high and its cytoplasmic concentration reaches 500-1000 nM. Changes in the intracellular Ca^{2+} concentration are detected as changes in fluorescence caused by binding of the fluorescent indicator Fluo-4 acetoxymethyl (AM) to free calcium ions[1]. After the AP is over, calcium is again transported from the intracellular to extracellular environment. The association constant of this indicator is 345 nM, which allows

reliable detection of Ca^{2+} in the range of 35-3500 nM thus making optical APs monitoring feasible. The monitoring is performed with a fluorescence microscope and all the cells within the field of view are monitored at the same time. Calcium transients that result from the ES are recorded and can be analyzed afterwards.

These experiments were carried out in collaboration with the group of S. Pluchino, MD at the University of Cambridge, specifically with the biotechnologists E. Giusto, PhD and M. Donegà whose expertise is in the field of stem cells and spinal cord injury. Their responsibility was the biological part of the experiments (e.g.: cell lines isolation, plating, culturing, immunological tests, biological data analysis and Ca^{2+} imaging), while our team was responsible for the experimental setup, development and fabrication of the devices, identification of the best stimulation protocol, development of an easy-to-use device/instrumentation interface (which implies both device holder and electrical connections and software stimulation setup) and remote control of the stimulations.

The whole setup underlies several critical constraints. Neurons (or other neuronal cell lines) have to be plated on the surface of the device. In biology, inverted microscopes are generally used and the full optical transparency of the substrate on which the cells are plated is required. Therefore, the whole OECT has to be transparent and has to reliably inject high currents. Experiments in biology require many replicates and each device can be used once. Just to give an idea, at the end of my PhD, we counted more than 1000 tested devices fabricated on 1x1 cm^2 substrate. As a consequence, an easy and rapid fabrication process is highly desirable. Cells are stimulated for time intervals ranging from few minutes up to hours and during this time they need to be immersed in cell culture medium. A pool to contain the medium and a stable connection with a perfusion system for the controlled delivery of chemicals are required. Electrical probes have to be engineered to provide easy connections between the pads on the device and the electronic equipment. The system has to be able to perform all the different possible combinations of electrical stimulations in terms of current, voltages, speed, frequency and so on. The system has to be easy programmable, it has to integrate a user-friendly graphic interface and it has

to be, when needed, remotely driven. Obviously, whatever gets in contact with cell culture medium or cells, has to be biocompatible and should be sterilized.

5.2 Experimental Section:

In the following, descriptions of apparatus and results of ES by means of highly biodegradable OECT are given.

5.2.1 Fabrication of the Stimulating OECTs

In order to perform reliable *in vitro* experiments, OECTs are fabricated with the same materials that are then used *in vivo*. 5 µm thick PLGA films remain fully transparent up to 12 days when immersed in cell culture medium (then opacification starts) and for unlimited time in air. The films are prepared using solvent casting technique. 1% PLGA solution in dichloromethane is casted onto a microscopy glass slide where a silicon frame (Sigma, S1815, SecureSlip™ glass coverslip, 1.2 x 1.2 cm^2) is well adhered. The films are then placed in the oven at 37 °C for 4 hours. 25 nm of gold are evaporated in a high vacuum chamber at a pressure of 10^{-6} mbar through shadow masks. The masks are designed with fixed contact pads and different channel length and width in order to investigate the effect of different geometries. Stainless steel masks were purchased from Lasertech s.r.l.. In this thesis, for sake of simplicity, the results of 4 OECTs with single geometry (L=200 µm and W=200 µm) are reported. 8 gold electrodes are patterned on each 1x1 cm^2 test pattern (TP) to define 4 couples of source/drain. On the surface PEDOT:PSS Clevios™ P Jet N V2 (Heraeus, Deutschland GmbH & Co) is spun. It is a particular formulation dedicated to ink-jet printing, which resulted particularly suitable due to its pH, closer to neutrality then standard PEDOT:PSS (e.g. the most used Clevios™ PH 1000). Only with the P Jet N V2 only we obtained a perfect adhesion while semiconductor film delamination is observed with more acidic PEDOT:PSS formulations. Our hypothesis is that acidic pH induces fast degradation of the exposed PLGA inducing rapid detachment when immersed in liquid. The commercial formulation is not used as purchased but 0.2% Silquest (3-glycidoxypropyltrimethoxysilane) and 5% DMSO (dimethyl sulfoxide) are added. The solution is sonicated for 30 minutes at 70 °C. The solution is spun at room temperature onto the PLGA/gold 5 µm thick film at

500 rpm for 3 seconds and 2200 rpm for 20 sec. The annealing is performed at 45 °C for 12 h. In order to fix the TP on the chuck of the spin coater and to increase the handing, 1x1 cm^2 glass slides (cut by means of a laser) are used as carriers. 1 µL of pure water is deposited on the glass surface in order to promote the adhesion of the plastic thin film onto the glass slide. Geometry of this transistor is not optimized for the sensing experiment. On the contrary, the exposed PEDOT:PSS area is maximized in order to widely apply ES to the whole network. No bare gold is directly exposed to the electrolyte.

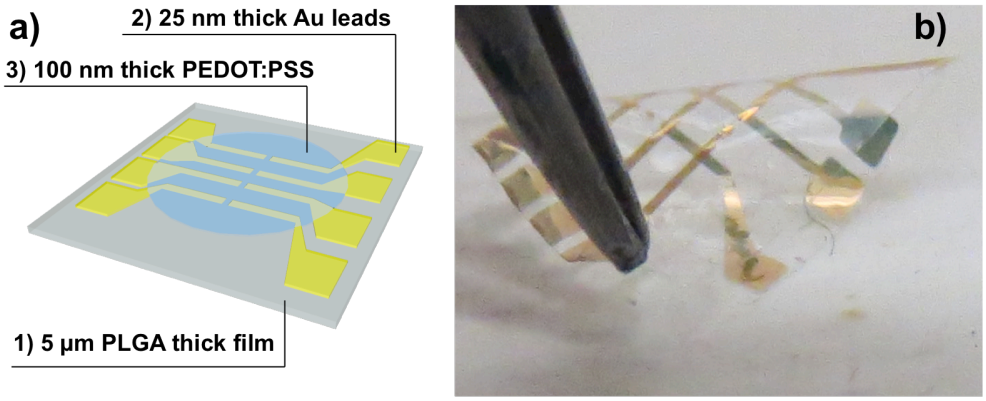

Figure 1 a) shows a scheme of a PLGA film where 25 nm of gold are evaporated through a shadow mask and a 100 nm thick PEDOT:PSS film is deposited by spin coating. **b)** picture of real TP device showing its flexibility and transparency.

5.2.2 Device holder

The device holder (DH) performs four main tasks: i) it provides an easy-to-set and stable electrical connection between the TP and the source measure unit (SMU); ii) it provides a transparent support to allow real time imaging with the inverted microscope; iii) it contains a pool to maintain the cells, cultured on the TP, immersed in the medium and iv) it contains an easy-to-plug microfluidic connector to the perfusion system. The DH, designed by Dr. T. Cramer, Dr. M. Murgia and me, was fabricated by M. Murgia. The DH is composed of two parts, the base and the top (**Figure 2**). The base contains a frame, positioned onto a transparent glass window, in which the TP is placed. On it, the top is fixed by

means of screw. The top is the most complex of the two parts. It contains a plastic *o-ring*, which can be removed and properly cleaned, that softly presses on the TP and confines the liquid that is contained on the pool above preventing both leakages and damages. The internal diameter of the *o-ring* is 5 mm that results in a TP exposed area of about 0.2 cm^2. Eight gold plated tips, dampened by means of an internal spring, are positioned on the top layer of the DH. When the DH is properly closed, the tips gently touch the pads of the TP. On the other side of the tips, 1 m long coaxial cables are soldered to provide easy and stable BNC connections with the SMU. On the top, an additional coaxial cable is fixed on which a metal gate electrode can be easily plugged and immersed into the pool. In the following experiment, a platinum wire is used. Two metallic small tubes enter the pool of the DH, they provide connections for easy plugging a perfusion pump. The device holder is made of Teflon shaped by means of lathe and other machinery.

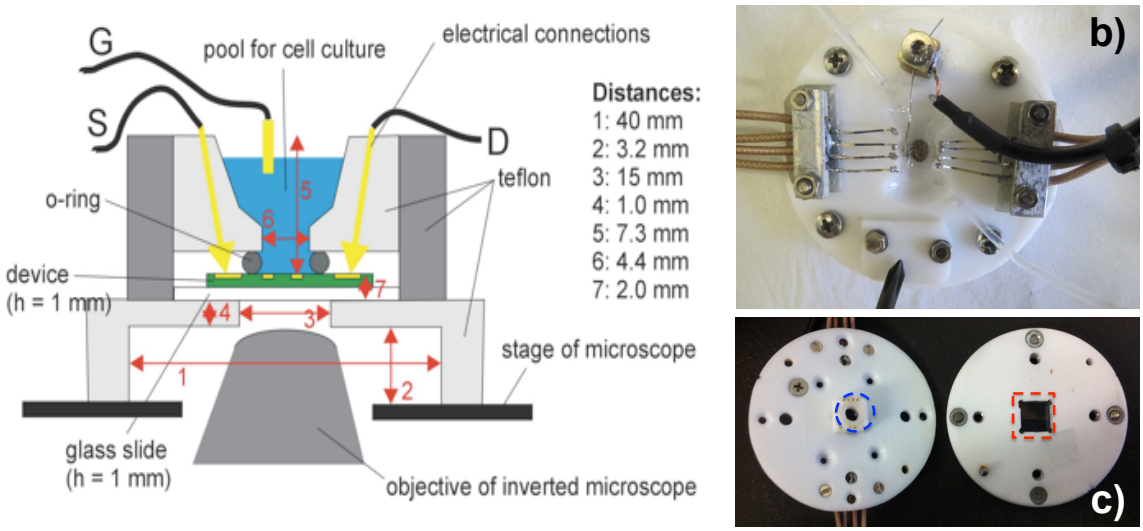

Figure 2 a) cross sectional scheme of a device holder with dimensions. **b)** top view picture of a device holder. **c)** a device holder opened, the spaces for the device and the *o-ring* are specified with a dashed red frame and dashed blue circle respectively.

5.2.3 Setup: Microscope, SMU and Software

The DH with inserted TP is placed on the stage of the fluorescence microscope (Leica DMI 4000B equipped with a DFC3000G camera and Leica SPE DMI4000B scanning laser confocal microscope). The camera can record

many shots; the number of collected frames per second is termed fps. Electrical measurements and stimulations are performed with a dual channel Agilent B2912A. In a simple configuration, a two-channels SMU can measure a single transistor (a channel dedicated to the drain and a channel dedicated to the gate with a common source). Dr. M. Murgia fabricated a multiplexer (MPX or MUX) that allows the fast addressing/switching of 4 transistors with a common gate (**Figure 3**). 8 BNC connectors (namely 4 sources and 4 drains) from the TP are plugged into the MPX that is connected by means of two BNC connectors to the High and Low input of a channel. At the same time, the gate from the DH is directly plugged onto the High of the remnant channel while to the Low goes the source shortened with the one coming from the MPX (**Figure 4a**). From this configuration, suitable for the sensing experiments and OECTs characterization, one can easily shift to the configuration for the stimulation (**Figure 4b**). Since the aim was to stimulate the whole surface, the MPX is equipped to force a short circuit between the 8 electrodes on the surface. The stimulation is then applied between the whole PEDOT:PSS surface and the platinum electrode immersed in the pool that serves as a counter electrode.

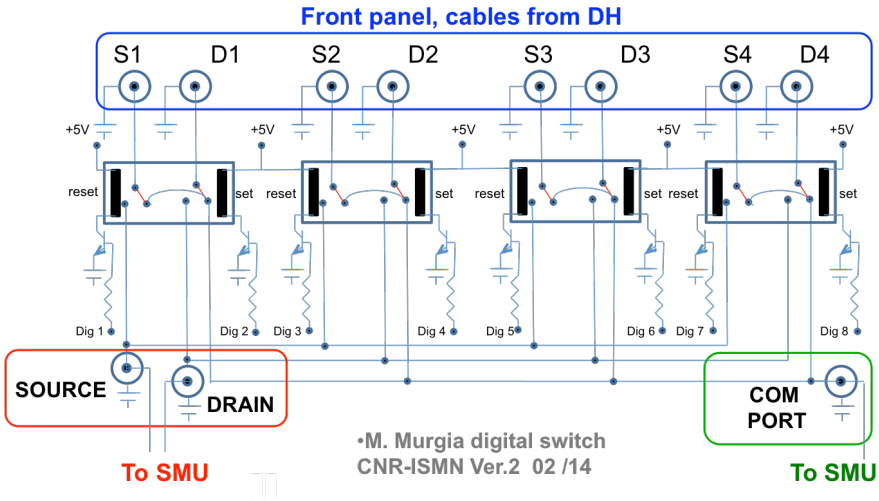

Figure 3 Four channels multiplexer (digital switch) internal scheme. It allows characterization in high-speed sequence of 4 transistors with a 2-channel instrument without the need of manual changing of wire connections. A common port connects in a short all the 8 independent ports (configuration used in stimulation).

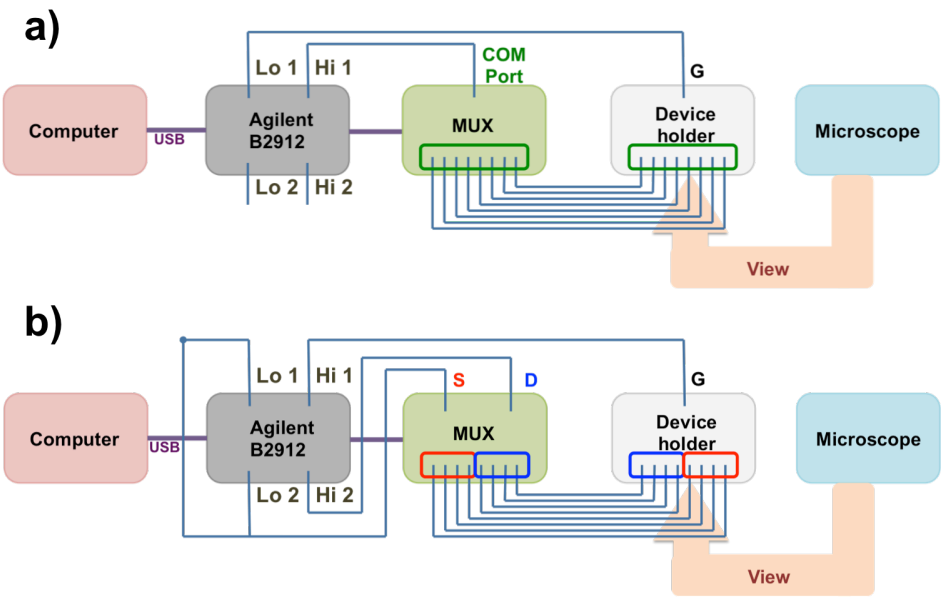

Figure 4 Simplified wiring diagram for the configurations adopted in stimulation **(a)** and recording **(b)**.

Dr. T. Cramer developed the software running on a graphical user interface (GUI) for stimulation and recording operations of the transistors. This software environment can be easily implemented, operated by people with minimum training or automatically, and can be expanded for experiments of an increasing degree of complexity.

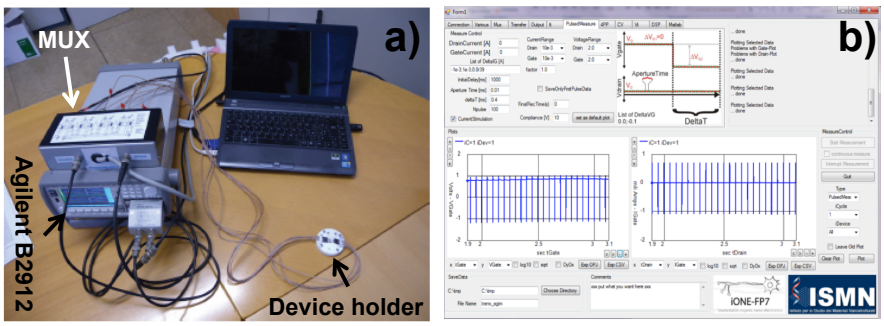

Figure 5 a) shows the compact setup for the electrical measurements composed of a device holder, the Agilent SMU, the multiplexer and a computer to drive the electronics. **b)** reports a snapshots of the software during electrical stimulation.

The software mounts an updatable library to supply sequences of bio-electrically relevant stimuli and to perform sensing. An example of a stimulus sequence is

shown in **Figure 5**. The interface allows one the most versatile choice of periodic stimuli where amplitude, duty cycle, duration, etc. can be independently fixed. Included with the software, there is also a proprietary library with stimulation waves that was developed by us during the tests we performed.

5.2.4 Stimulation Protocols

The kinds of different stimuli one can apply are unlimited. Indeed, in terms of pulse shapes, timing, amplitude and frequency the number of possible combinations is infinite. To restrict the range of parameters, we have exploited basic rules inferred from electrochemistry in *in vitro* electrophysiology that have been studied for years[2].

Many different shapes and frequencies were tested while looking for calcium waves transients. Nevertheless, for sake of brevity, the most successful stimuli and their effects onto cells are reported in this thesis.

In order to create charge unbalance around the cell membrane, high current density has to be delivered. To increase reproducibility, it is more effective to drive the stimuli in terms of current density instead of voltage. In order to reduce the faradaic component of the electrical stimulation, and let the capacitor behavior dominate, the pulse have to be short (ms regime) and charge neutrality has to be re-established at the end of the stimuli. In this manner, no sizable chemical change occurs either at the electrode or at the tissue. Products of irreversible electrochemical reactions (e.g. oxygen or chloride, hydronium, toxic species) could be extremely detrimental for the cells. The best way to minimize these undesired processes is to apply a short biphasic pulse. Beyond the shape and timing, the amplitude of the pulse is also important. The injected current density has to go beyond a threshold otherwise cell depolarization is not induced at all and calcium intake is not triggered. The stimulation threshold represents the minimum amount of current that generates a response and depends on the type of cell/tissue and on the system configuration. The PEDOT:PSS surface show a very high specific capacitance of about of 500 $\mu F/cm^2$ that means it easily injects high amount of current. The higher the current, the higher is the efficacy of the ES. This is valid until a second threshold, called damage threshold that, if

exceeded, leads to cell damages. Furthermore, each electrode is characterized by a reversible charge injection limit, which represents the total amount of charge that may be stored reversibly (including storage in the double layer capacitance and any reversible faradaic reaction). In ES of excitable tissues, to have a high reversible charge injection is desirable. It means a high amount of charge is delivered prior to the onset of irreversible Faradaic reactions that could damage the electrode leading to the breakdown. This parameter depends upon the active electrode material, the size and the shape of the electrode, the electrolyte composition and stimulation waveform. Resulting from these limitations, safe and efficient ES occurs only in a narrow current window.

Specifications about the applied stimuli waveform are reported in **Figure 6**. Current is injected from the PEDOT:PSS surface in about 0.5 ms and the charge neutrality is restored in less then 2 ms. The stimuli is defined as a cathodic first bipolar pulse driven in current. This means the PEDOT:PSS surface, very close to the cell junctional membrane, is negatively charged and then rapidly neutralized after a reversed current peak.

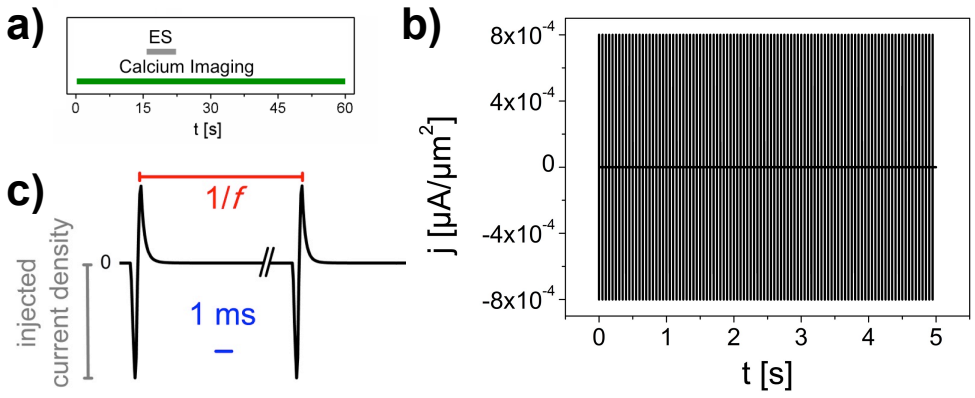

Figure 6 a) reports the general timing of the experiment with the 15 seconds of basal fluorescence recording, five seconds of simultaneous stimulation and fluorescence recording and the final 35 seconds of fluorescence recording only. **b)** Example of five seconds stimulation. Each stimulus has an amplitude of $8*10^{-4}$ µA/µm^2 and the repetition frequency is 20 Hz. **c)** Detail of sharp bipolar electrical stimuli. Current is injected and electroneutrality restored in less then 2 ms.

Injected current densities are varied between $4*10^{-5}$ to $4*10^{-3}$ $\mu A/\mu m^2$, which is below the safety limit for the Au/PEDOT:PSS electrodes. Repetition frequencies are varied between the single pulse and 500 Hz. In the standard experiment five seconds burst stimulation follows 15 seconds of basal recording and the effect is optically monitored 35 s further. Long-term stimulations are intended to stand for one hour. When experimental conditions are different, a description is provided within the section.

5.3 ES Activity onto Primary Neurons

5.3.1 Primary neurons culturing

E. Giusto and M. Donegà performed cell plating and culturing at University of Cambridge. First round of stimulation experiments were performed with neural progenitor cells (NPCs) differentiated into neuronal cells. The results reported here were obtained with rat E18 primary cortical neurons that were adopted at the second round of experiments to increase reliability. Plating is performed directly onto the device with a density of $4x10^4$ cell cm^{-2}. Few details about the culturing are given in the experimental section. More detailed information are reported in M. Donegà's PhD thesis. **Figure 7a** reports a picture of a TP while **Figure 7b** shows an optical fluorescence image in the presence of a fluorescent dye that binds Ca^{2+}.

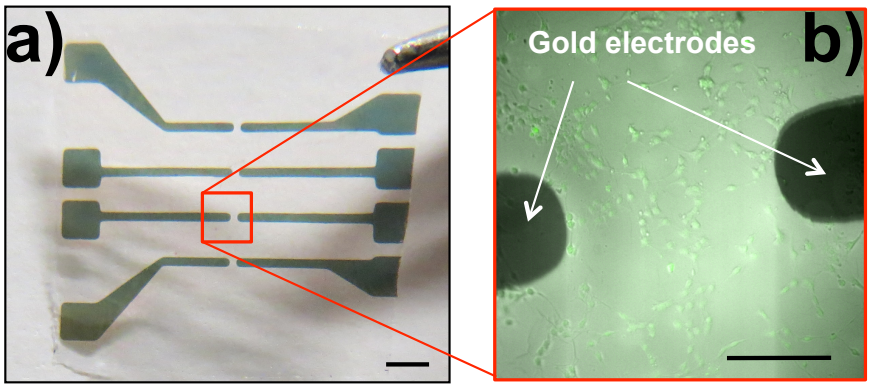

Figure 7 a) picture of a device with L=W=200 µm, scale bar 1 mm. **b)** reports an optical image (brigth field + Fluo-4) of primary neurons plated onto the PLGA surface. The scale bar is 200 µm since the device has W=200 µm and L=400 µm.

In order to characterize the phenotype of plated and cultured cells, immunofluorescence staining is used. This technique is based on the specific recognition of antibodies to antigens and is used to target fluorescent dyes that bind specifically biomolecules within the cell thus allowing direct visualization of the distribution of the target molecule in the sample (**Figure 8a** and **b**). Different antigens were investigated: i) DAPI (a dye that strongly binds A-T rich regions in DNA like nucleus), ii) βIII-Tubulin (microtubule element found almost exclusively in neurons), iii) microtubule-associated protein (MAP)-2 (microtubule-associated protein family, related to neuron specific cytoskeletal proteins enriched in dendrites), iv) GFAP (glial fibrillary acidic protein that is expressed by various cell types including astrocytes), v) Nestin (neural stem/progenitor cell marker, expressed in neural cells) and vi) ionized calcium binding adaptor molecule (Iba) (protein specifically expressed in macrophages/microglia). **Figure 8c** shows the high percentage of βIII-Tubulin and MAP-2 positive neurons. The portion of the remaining cells is composed of astrocytes, microglia and nestin positive cells. Upon further staining, none of the cells were positive to fibronectin (expressed in fibroblasts). 10-15 % were positive for NG2 (oligodendrocytes precursor cells) but easily distinguishable, due to the smaller nucleus, from neurons. The complete analysis is performed at different time points 7-9 days *in vitro* (DIV) and 14-16 DIV and no significant differences were observed.

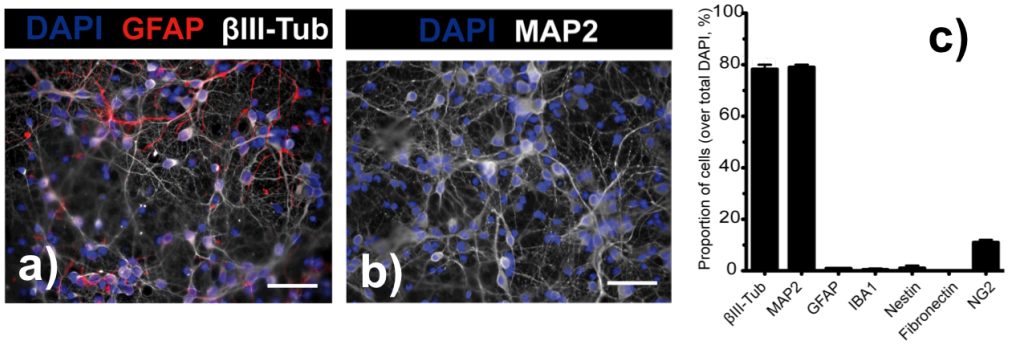

Figure 8 Representative images of the characterization of cortical rat neurons onto OECTs by means of immunofluorescence. Images are taken at 7-9 or 14-16 DIV. **a)** and **b)** show the staining for βIII-Tubulin, DAPI and GFAP, scale bar 50 μm. **c)** Graph shows the proportion of cells (percentage over total DAPI) positive for the different antigens tested. Figures also reported in the PhD thesis of M. Donegà.

The maturation state is relevant to the electrical activity of a neuron and to the capacity of generating APs. In order to investigate ES of neurons at a proper time point, M. Donegà performed *in vitro* patch-clamp of the neurons cultured onto the devices (**Figure 9**). Many different parameters were extracted, among them: resting membrane potential, proportion of cells able to fire single or multiple APs, input resistance and membrane capacitance. As the cell maturates, from 7-9 to 14-16 DIV, differences are generally observed: the resting membrane potential shifts to more hyperpolarized potential and APs can be more easily generated upon stimulus. Even if detectable and directly ascribed to higher maturation, only slight differences were observed between the two time points. However, at 14-16 DIV the PLGA substrate is rougher and opaque and a higher percentage of cell death was observed. For these two reasons, stimulation of cortical neuron is performed at 7-9 rather then 14-16 DIV.

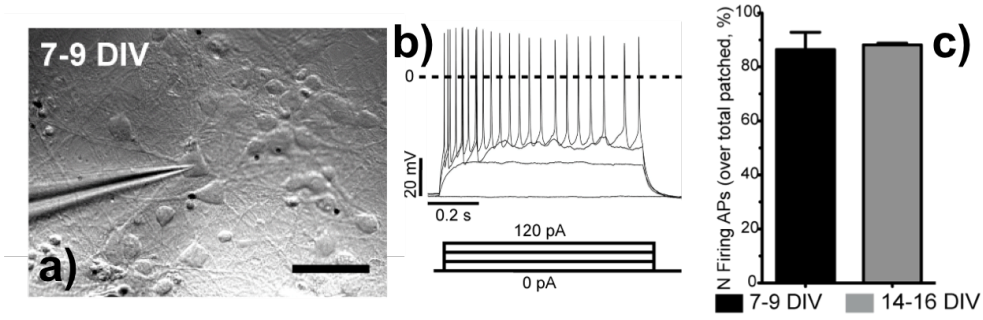

Figure 9 a) The optical image shows a cortical neuron patched onto the PLGA/OECT and in **b)** are reported representative traces of the variation of membrane potential upon injection of positive current steps (from 0 to 120 pA); **c)** reports the fraction of firing cells at two different time points. Figures also reported in the PhD thesis of M. Donegà.

5.3.2 Results and Discussions

As previously stated, in the current thesis the most successful stimulation protocol only is reported and described. It generates the best response in terms of calcium waves stimulation and minimization of detrimental responses. The stimulation protocol is the one already reported in **Figure 6**. The field is always randomly chosen in the area where the culture medium is confined. In order to investigate the relation between the intensity of the stimuli and the effect evoked,

the first approach is to supply a 20 Hz stimulation. Stimulation current densities are varied from $4*10^{-5}$ to $4*10^{-3}$ μA/μm^2. Their effect is shown in **Figure 10**. When the injected current is below the threshold, no variations of the spontaneous activity are observed. At the threshold, the overall population responds to the ES with a fast and sharp increase in the intracellular fluorescence. As soon as the stimulus is completed, the basal fluorescence level of each single cell is recovered.

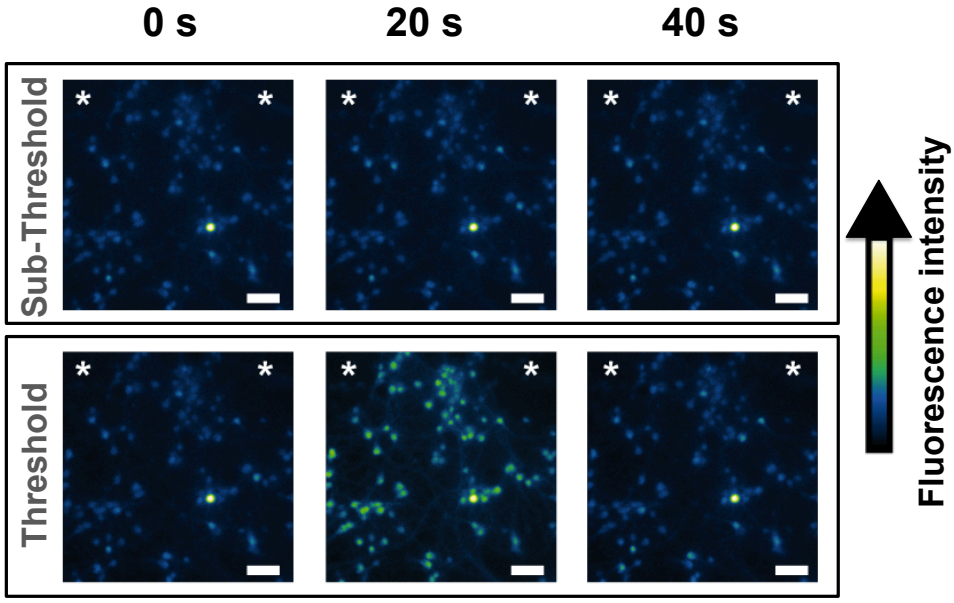

Figure 10 shows the Ca^{2+} transients induced by ES. The frames report the snapshots of fluorescence at different timing (0 s, 20 s and 40 s) both at the sub-threshold and at the threshold ES. When below a certain intensity, ES does not induce significant changes in the fluorescence while above the threshold a clear response is recorded. The stars (*) indicate the gold electrodes position in the field. Scale bar is 50 μm. Figures modified from the PhD thesis of M. Donegà.

The simplified scheme of the electrical current flow during the stimulation is reported in **Figure 11**. A falling voltage ramp applied to the substrate evokes a capacitive current that creates a voltage profile around the cell. Both the junctional membrane and the upper side cell membrane exposed to the electrolyte results polarized. The junctional membrane, that is described as the center of the membrane exposed to the PEDOT:PSS surface, is strongly

depolarized while the upper side is weakly hyperpolarized[3,4]. The strong depolarization during a falling voltage ramp is able to activate ion channels in the center of the adhered membrane. The resulting inward flow of calcium ions depolarizes the cell. In order to confirm this hypothesis, further experiments are performed as described in the following.

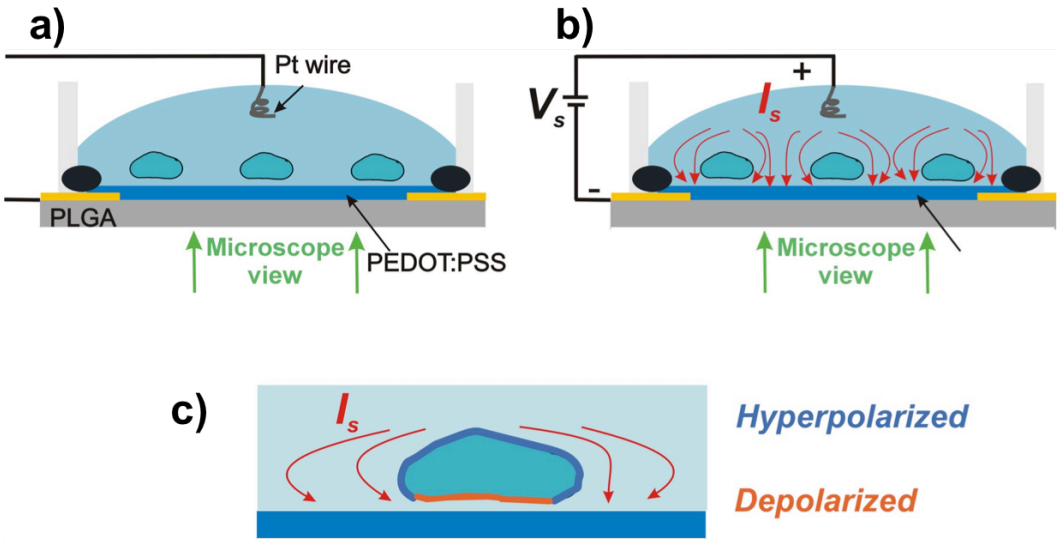

Figure 11 a) Cross section of the PLGA/OECT with cells plated on top in resting condition. **b)** Wiring diagram and schematics of the current flowing around the cells during the cathodic first bipolar pulse. **c)** Detail of the membrane polarization during the stimuli with the junctional membrane strongly depolarized and the weakly hyperpolarized upper side membrane.

In order to investigate the response to different current densities, the intracellular fluorescence variations were quantified as $\Delta F/F0$ over time, where ΔF is defined as the difference between the *Fi* (fluorescence at time *i*) and F0. The results at a constant frequency of 20 Hz are shown in **Figure 12**. The threshold above which a collective response is detectable is found to be $8*10^{-4}$ $\mu A/\mu m^2$ even if at lower injected current densities ($2*10^{-4}$ $\mu A/\mu m^2$) few cells already respond. The time to restore a basal fluorescence after the ES is less then 10 seconds. On the contrary, when the current injected is about $4*10^{-3}$ $\mu A/\mu m^2$ cells undergo a strong not fully reversible stimulation. This is revealed by longer time of the Ca^{2+} transients and by the fact that few cells, even after

minutes, show high intracellular calcium levels. Furthermore, the overall number of responding cells is lower. Interestingly, the response to different intensities is mainly in terms of number of responding cells rather then in the ΔF parameter. Importantly, the time needed for intracellular calcium concentration to be restored is comparable to what observed[5] with field induced stimulation coupled to rapid fluorescence imaging and is consistent with AP-induced Ca^{2+} modulation in the soma.

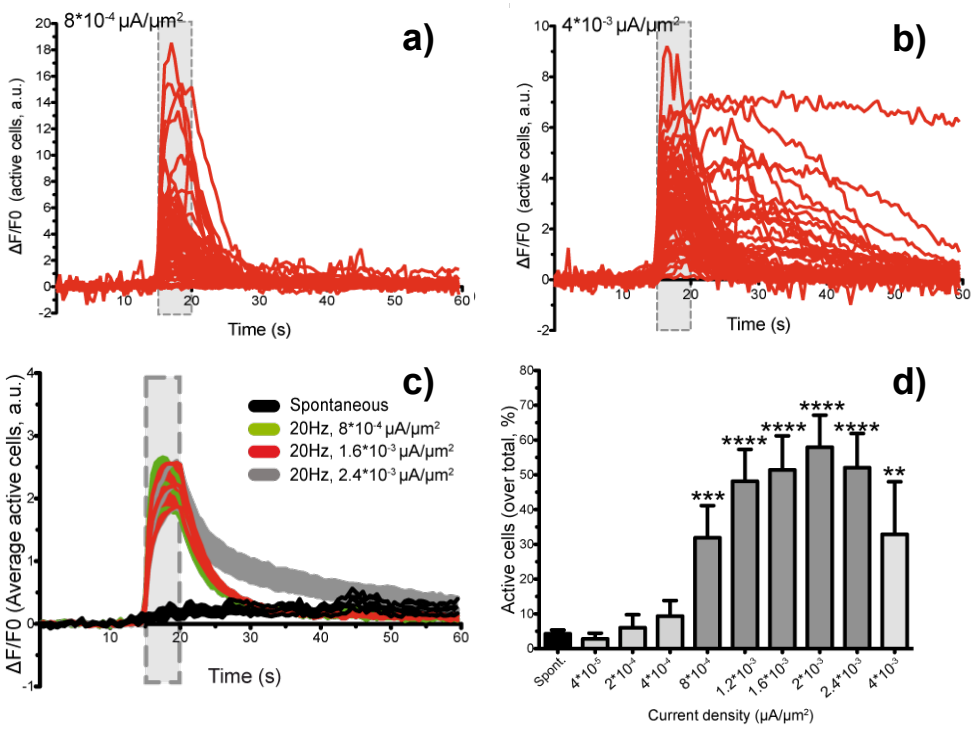

Figure 12 Effects of the injected current densities onto the neuronal network. **a)** and **b)** report fluorescence variations over the 60 seconds of optical recording at a current density of $8*10^{-4}$ µA/µm^2 and $4*10^{-3}$ µA/µm^2 and a frequency of 20 Hz. The 5 seconds during the stimuli are highlighted as a grey area in which the variations occur. **c)** the average fluorescence response of the neuronal population **d)** Fraction of cells responding to specific ES. Different grey levels highlights the different regimes. The darker grey area is considered the most efficient ES intensity range. Figures also reported in the PhD thesis of M. Donegà where specifications about the statistical analysis are given.

After investigation of the stimuli intensity, the effect of the frequency was explored. Keeping constant the injected current density at $1.6*10^{-3}$ $\mu A/\mu m^2$ different samples were stimulated at frequency ranging from the single pulse up to 500 Hz. Different regimes are observed (**Figure 13**). The response of the neurons to frequencies lower then 2 Hz is not observed while at frequencies up to 50 Hz fluorescence intensity increases with frequency. At higher frequencies, few cells respond to electrical stimulation and the recovery to basal fluorescence is slower.

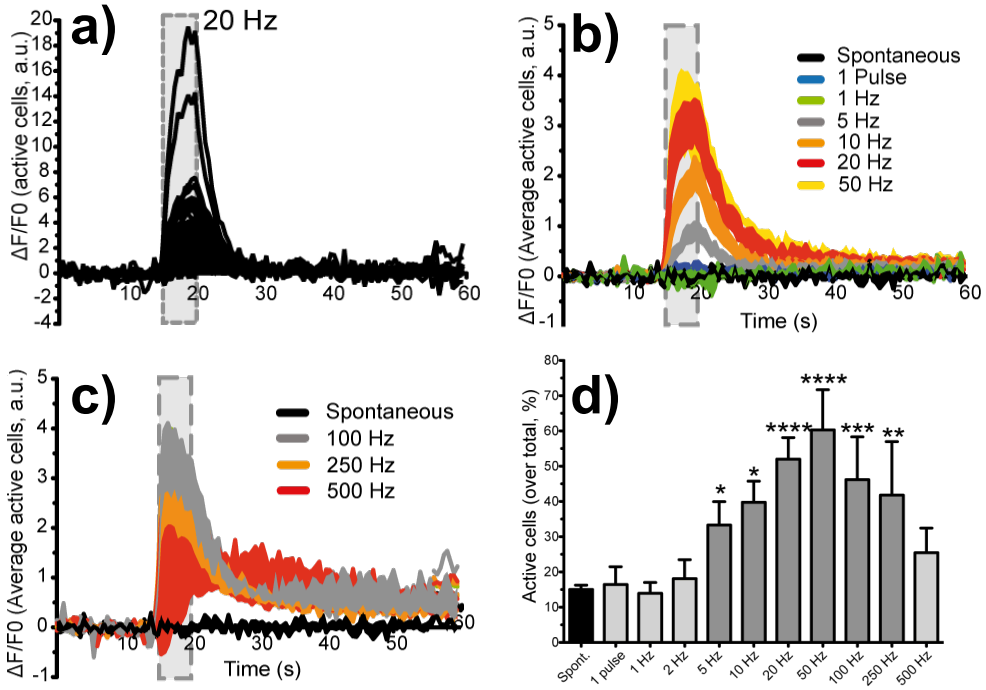

Figure 13 Effects of the ES frequencies onto neuronal network. **a)** reports fluorescence variations over the 60 seconds of optical recording at a current density of $1.6*10^{-3}$ $\mu A/\mu m^2$ at 20 Hz repetition frequency. The 5 seconds during the stimuli are highlighted as a grey area. **b)** and **c)** report $\Delta F/F0$ induced by injection current density of $1.6*10^{-3}$ $\mu A/\mu m^2$ at various repetition frequencies in two different regimes, respectively full and partial recovery. **d)** Number of cells responding to specific ES. Different bars colours highlights the different regimes. The darker grey area is considered the most efficient ES frequency range. Figures also reported in the PhD thesis of M. Donegà where specifications about the statistical analysis are given.

If the applied voltages are very high, electroporation mechanism is induced. Electroporation is a dynamic phenomenon that depends on the local transmembrane voltage that induces membrane rearrangement. Diffusion of ions and even larger bioactive molecules is enabled by the opening of nm-diameter holes in the lipid bilayer. This phenomenon is not selective and it is highly undesired. To demonstrate the calcium intake is mainly caused by VGCCs activation rather than electroporation, further experiments were performed. In particular, ES in standard condition ($1.6*10^{-3}$ μA/μm^2, 20 Hz) with OECTs is performed in presence of VGCCs blockers, ω-Conotoxin GVIA and Nimodipine. Their presence inhibits the activity of VGCCs. When ES is performed in the presence of blockers, the transients of calcium ions are strongly reduced, **Figure 14**. Then, washing out the blockers, the response is restored.

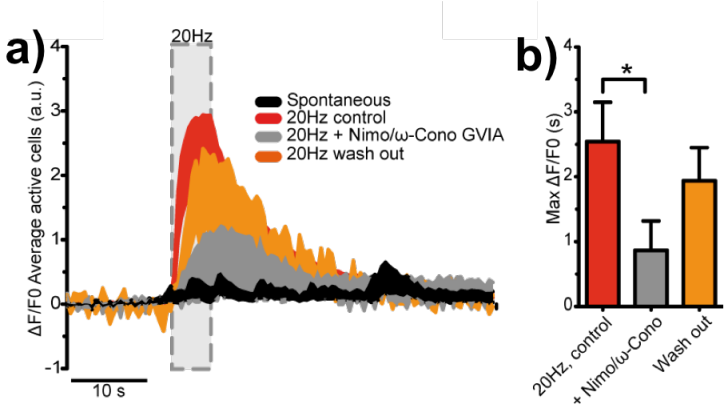

Figure 14 The comparative effect of ES in the presence and absence of blockers is reported in terms of **a)** fluorescence variation over time and **b)** maximum overall fluorescence variation. Figures also reported in the PhD thesis of M. Donegà where specifications about the statistical analysis are given.

The next question is: how long neural cells stand electrical stimulation? To answer this question, with the aim to determine the protocol safety, a new series of experiments is performed where the population is subjected to repeated stimulations (**Figure 15**). In particular, 10 successive bursts with the following protocol are applied: five seconds of electrical stimulation by injecting $1.6*10^{-3}$ μA/μm^2 at 20 Hz every 30 seconds. This experiment also is performed under

fluorescence microscope that allows the monitoring of repeated calcium transients.

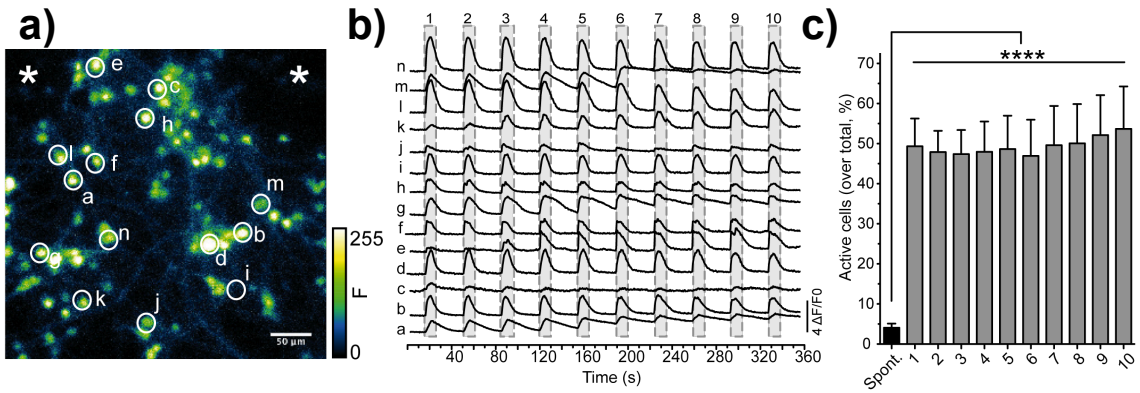

Figure 15 a) representative fluorescence optical microscopy frame of the neurons stimulated for 6 minutes at $1.6*10^{-3}$ µA/µm^2 at 20 Hz. Stars indicate electrodes positions. **b)** the fluorescence traces of single investigated cells marked with a letter in the first panel. **c)** General trend reporting the fraction of active cells in each series of stimuli. Figures also reported in the PhD thesis of M. Donegà.

Prolonged stimulations are then applied for one hour. The usage of patterned ES was already demonstrated more efficient than continuous stimulation (obtained either chemically or electrically) to promote BDNF, brain-derived neurotrophic factor (a protein related to nerve growth factor), release from neurons in vitro[6,7] and in the dorsal horn of the spinal cord[8]. For these reasons, each burst is composed of: five seconds of electrical stimulation by injecting $8.0*10^{-4}$ µA/µm^2, $1.6*10^{-3}$ µA/µm^2 or $4.0*10^{-3}$ µA/µm^2 at 20 Hz every 30 seconds. The effects onto the neuronal network, in terms of cell viability, of ES at different injected current densities are compared with non-stimulated cells onto devices used as control (**Figure 16**). Details of the results are not described in detail in this thesis, where a resume only is given, while they can be found in M. Donegà's thesis. The fraction of cells expressing neuronal marker is constant in all the conditions as well as the total number of cells in all the conditions investigated. The number of apoptotic cells (stained with cCASP3) does not change in different samples. On the contrary, the number of neuronal cells positive to propidium iodide (PI), which is a marker for necrosis, is sensitively

higher at the highest injected current density. This data, correlated with the shorter processes (dendrites) resulting from the more extreme stimulating conditions, suggesting strong detrimental effects of high injection current density stimulation.

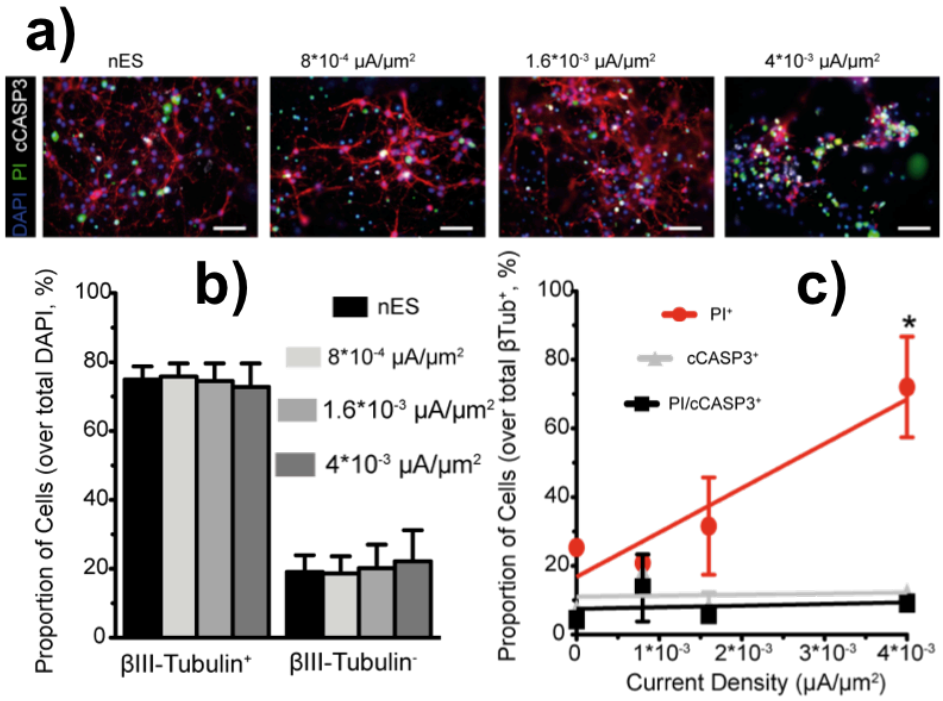

Figure 16 a) reports composite immunofluorescence images of neuronal cells stained for βIII-Tubulin (red), PI (green) and cCASP3 (grey) on the device at 24 h after 1 h electrical stimulation. **b)** Proportion of neuronal and non-neuronal cells for the different conditions. **c)** Proportion of neuronal cells positive to PI, cCASP and both PI and cCASP. Figures modified from the PhD thesis of M. Donegà, where specifications about the statistical analysis are given.

At the sampling speed of two fps, we observe a simultaneous response of the neural population in the optical field. The time resolution does not allow an investigation of the signal propagation onto the neural population that occurs in the milliseconds range. A direct investigation of the real role of the semiconductor into the electrical stimulation is not possible. Due to the adopted configuration, one can not exclude a faster response of the cells onto PEDOT:PSS which are closer to the gold electrode. Indeed, one hypothesis involves a contribution of signal transmission between neighbour cells that could induce a cascade effect

and a calcium wave propagation from the regions closer to metal leads towards PEDOT:PSS covered surface. In order to demonstrate the strong relevance of PEDOT:PSS, PLGA 5 µm thick devices are prepared where the semiconductor was not deposited and gold electrodes are exposed. ES is performed, with the same parameters, with gold electrodes (**Figure 17**). Immunofluorescence demonstrates that cell growth of these semiconductor-deprived devices and full OECTs is comparable. As expected, no low injection current density stimulation is achieved. On the contrary, to provoke a response the amplitude of the stimulation has to be increased of about one order of magnitude. The response, collectively delayed, is anomalous and suggests detrimental effects onto the neural population.

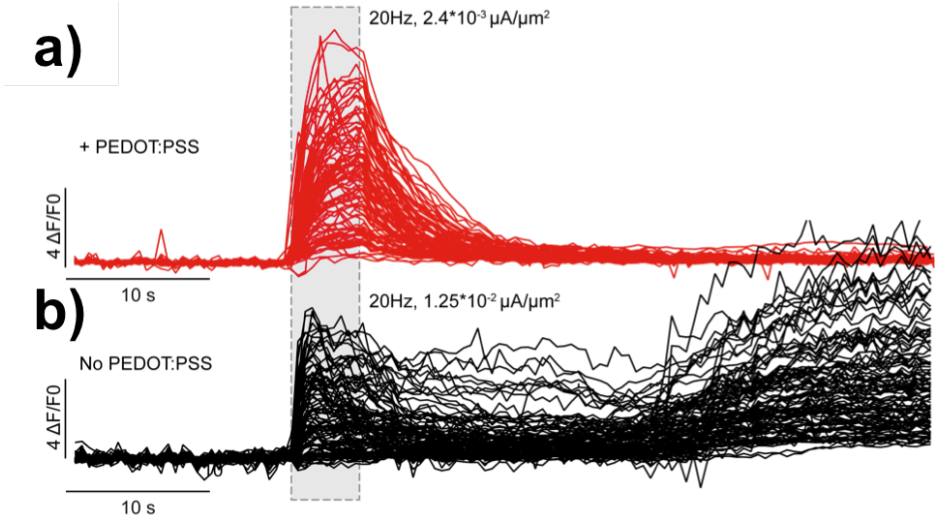

Figure 17 a) and **b)** reports a comparison of the effect, in terms of fluorescence variation, of ES performed with and without the PEDOT:PSS layer. Current density is calculated considering the effective stimulating area. In b) the effect of on of the most efficient ES without PEDOT:PSS, injected current density is higher and the response is anomalous. Figures also reported in the PhD thesis of M. Donegà.

5.3.3 Conclusions

OECTs dedicated to the electrical stimulation of neuronal network are designed and fabricated. The devices are composed of a layer of biodegradable

and biocompatible material, which represents the scaffold, that maintains optical transparency for the time needed for *in vitro* investigation. As active material a conductive polymer, PEDOT:PSS, connected with gold leads (S and D electrodes in OECT configuration), is used. The device is >99% mass biodegradable. The devices are operationally stable up to one month of continuous operation (they were not tested longer). A dedicated full set of components is designed and developed to perform real time monitoring of the calcium uptake (induced with the OECT stimulation) by using a standard inverted fluorescence microscope. The cell viability onto the device is demonstrated for rat cortical neurons that, at 7-9 DIV, are demonstrated able to fire APs.

In vitro electrical stimulation of mature central nervous system neuronal networks performed with the OECT devices is highly efficient. The high versatility of the system is demonstrated by the fact that a library of stimuli can be applied. Many different stimuli parameters were tested prior to find the best conditions. A short bipolar pulse is used to stimulate the neuronal population. Frequency, amplitude (intensity) and resting timing between bursts effects are tested and optimized to increase efficiency while decreasing detrimental effects. The principal evaluation parameters are the intracellular fluorescence variation induced by the stimuli, recovery time and the immunofluorescence staining. Highest stimulation efficiency occurs in specific injected current density ($8.0*10^{-4}$ - $2.4*10^{-3}$ $\mu A/\mu m^2$) and frequency (5-250 Hz) ranges. Within this range, the stimulation of APs, which induce the VGCC activation, is highly reliable and reproducible. Taking advantage of the high versatility of our setup, experiments are performed to exclude the involvement of electroporation as the cause of ES calcium ions intake. The usage of VGCCs blockers during ES demonstrates that when ion selective channels are disabled the calcium transients are strongly reduced.

The crucial relevance of the organic semiconductor is demonstrated as it reduces the injection current density threshold needed to achieve an efficient stimulation. The last is highly recommended to reduce the risk of detrimental reactions for cells and tissues and to avoid irreversible damages to electrodes.

Medium term (1 hour) stimulation is performed and it is demonstrated to be safe for the neuronal network, if below a certain threshold. These results allow us

to identify the best parameters that are used in the following *in vivo* experiments. Interestingly, the identified *in vitro* safe threshold is coherent with what reported in literature for *ex vivo* retinal preparation[9]. Even if the tissue nature is different, the ranges are comparable. They found a linear correlation between the timing of the pulse and the safe threshold. For 0.8 ms pulse duration, the extrapolated threshold (also found by PI staining) is 0.225 A/cm^2. Optimized stimulation proposed with the OECT is 1.6 μA/μm^2 that is (0.16 A/cm^2), actually below the threshold.

To conclude, the parameters found efficient and safe in these experiments, are used in the following *in vitro* (Section 5.4) and *in vivo* (Chapter 7) experiments.

5.4 ES Activity onto Reactive Macrophages

Electrical stimulation directly modulates the activity of excitable cells like neurons. Non-excitable cells are immersed in the electric field during the electrical stimulation and can be directly or indirectly affected. Indeed, glial and immune cells communicate with neurons both due to direct contact and trough the bioactive molecules in the fluids. For instance, glial cells express several specific receptors for ligands released by neurons during APs (e.g. GABA, serotonin, glutamate etc.) and calcium transients in glial cells were observed as a consequence of neural activity[10]. This could justify the hypothesis of indirectly induced phenotypical changes, mediated by intercellular signaling pathways, in glial cells as a consequence of electrical stimulation. Furthermore, a direct effect of electrical stimulation onto glial and immune cells cannot be excluded since the idea of “non-excitable” cell is recently strongly reconsidered. As an example, epithelial cells respond to electrical stimuli as effects in wound reseal are largely demonstrated and are considered to be related to the increased fibroblasts and epithelial cells proliferation[11]. The lasts two classes of cells up-regulate growth factors and cytokine release as consequence of electrical stimulation or static electric fields[12,13]. Several examples of changes induced onto non-neuronal cells by ES have been reported in the literature. Even if their mechanisms are still not fully understood, it is reasonable to hypothesize the presence of voltage sensitive channels and receptors on the surface of the cell membranes. Indeed, the

presence of VGICs in some classes of non-excitable cells is demonstrated[14,15] and the patch clamp experiments revealed the non-classical role of VGIC in various cells like astrocytes and microglia.

For all these reasons and more, becomes extremely interesting to investigate the effects of the electrical stimulation on non-neuronal cells. Since macrophages (MPs) infiltrate the SC soon after the injury (Chapter 1), and together with microglia, play an important role in the secondary phase of the SCI, the effect of ES onto MPs is investigated. Possible effects range from ions influx through cell membrane, the release of specific ligands and factors to the cytoskeletal mobility and cells migration. However, the most probable hypothesis is the direct influence of the ES trough the VGICs and a possible modulation of inflammatory activity.

In order to compare the effects of the ES onto MPs and primary neurons, the experimental conditions are the same reported in the previous sections. The ES is performed both on resting and on activated MPs. Pro inflammatory activation is chemically achieved by means of addition, to the cell culture medium, of Escherichia Coli lipopolysaccharides (LPS). Stimulation is followed by RNA extraction and microarray gene expression analysis as well as immunofluorescence staining and biochemical assay. MPs viability after stimulation is evaluated as well. Finally, blockers were used to investigate the stimulation mechanism pathway and to propose a specific interpretation.

Toward this goal, I fabricated the devices and provided full remote assistance for the electrical stimulation protocols and experimental setup, while the biological investigation was performed at the University of Cambridge.

5.4.1 Macrophages Culturing

Bone marrow-derives monocytes are isolated from adult C57BL/6 male mice. They are cultured and differentiated onto macrophages and then plated onto PLGA/OECTs at a density of 27000 cells/cm^2. The presence of VGIC is verified (**Figure 18**).

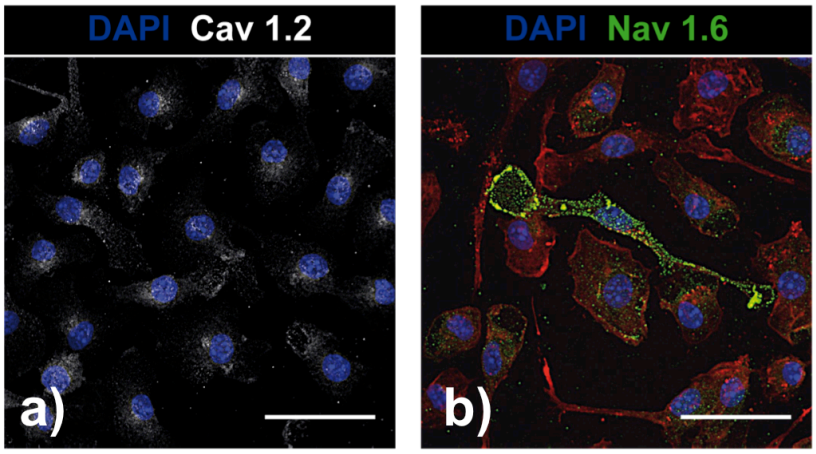

Figure 18 a) and **b)** report confocal images of resting mouse macrophages onto PLGA/OECTs. Cells are stained for Cav 1.2 (to indicate VGCCs) in white in **a)** and for Nav 1.6 (to indicate VGSCs) in green in **b)**. Staining for DAPI is in blue while in red is stained fluorescent conjugated Phalloidin to visualize F-actin (important in cell motility of division).

5.4.2 Results and Discussions

48 hours after cells plating, by placing the device inside the device holder (connected as in **Figure 4a**) the ES in performed. The stimulation protocol, one hour long, is composed of five seconds of 20 Hz bipolar cathodic first pulses at a current density of $1.6*10^{-3}$ $\mu A/\mu m^2$ every 90 s. It is applied to MPs both in resting conditions and pro-inflammatory activated while as controls samples are used non-ES equivalent samples. For sake of brevity, the full protocol that leads to the RNA extraction for microarray and/or qRT-PCR (reverse transcription-polymerase chain reaction, variant of PCR used to detect RNA expression) gene expression profiling analysis is not described in this thesis and can be found in M. Donegà's PhD thesis.

The up-regulation of 125 genes in the LPS-activated MPs with respect the resting MPs is shown by the microarray analysis reported in **Figure 19b**. On the contrary, the comparison of resting non-ES with resting ES does not show differences (**Figure 19c**). Volcano plot is not something chemists are familiar with. It is a scatter-plot used in statistics that is helpful in the representation of changes in large datasets of two compared conditions. The significance (on the Y-axis) is reported vs the fold-change (on the X-axis). A quick visualization of

those genes that display large changes (plotted in blue) that are statistically significant is enabled.

The very relevant result is the significant down-regulation of twelve genes found in the ES pro-inflammatory activated MPs respect the non-ES pro-inflammatory activated MPs (**Figure 19d**). These genes are within the 125 genes upregulated with the LPS activation. Furthermore, a general ES induced down-regulation is found in the remnant 113 genes upregulated with LPS.

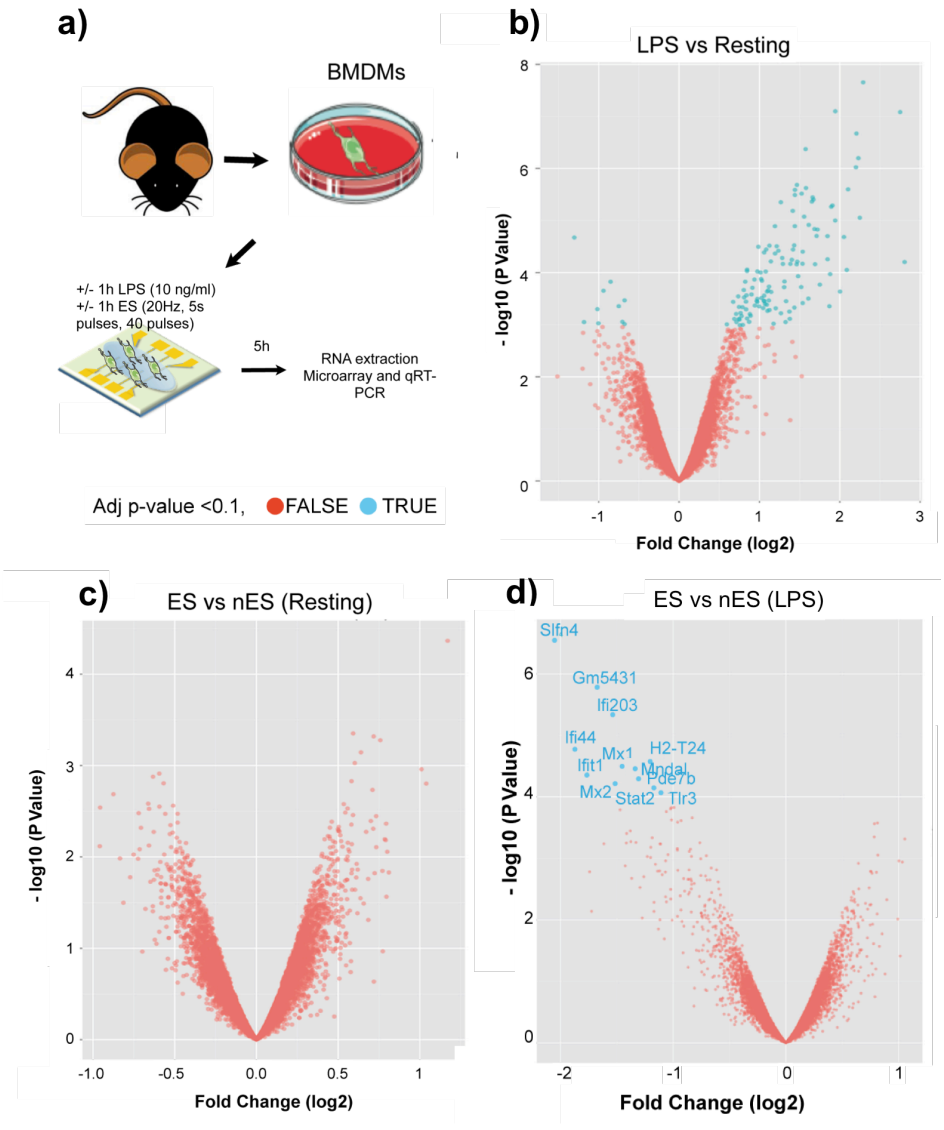

Figure 19 a) Scheme of *in vitro* experiments that shows MPs extracted from mouse, cultured and then seeded onto the device two days before ES in the presence or

absence of LPS activation. One hour after ES is concluded RNA extraction occurs. **b)**, **c)** and **d)** show the Volcano plots reporting the comparison of mRNA expression in the different conditions respectively: LPS vs resting, resting ES vs resting non-ES and LPS ES vs LPS non-ES. In Y-axis the p Value (-log10) is reported while in X-axis is expressed the Fold change (log2). The negative fold change is representative of a downregulation; on the contrary positive values indicate upregulation. Where the mRNA changes are significant, the spots are reported in blue. Graphs also reported in the PhD thesis of M. Donegà.

These results suggest an ES driven global reduction of pro-inflammatory activation induced by LPS treatment. Interestingly, ES does not affect the genes that are not activated by LPS. These results are also validated with qRT-PCR monitoring the regulation of the 12 genes found changed with microarray. The qRT-PCR confirms the general downregulation and finds it particularly significant for Il-6.

Cell viability of electrically stimulated MPs, both resting and LPS activated, is determined by quantifying the accumulation of lactate dehydrogenase (LDH) in the medium after 24 h. LDH is a biomarker for cytotoxicity and cytolysis (or osmotic lysis) and it is not found to be increased upon ES MPs. Immunofluorescence also doesn't show increasing in the number of cells positive to Propidium Iodide and/or cleaved Caspase 3 demonstrating the safety of the stimulation protocol.

In order to discriminate the role of VGICs in ES-induced downregulation of MPs reactivity, three different blockers (both for sodium and for calcium ions) are used. The effect of the presence of single or the group of blockers onto ES and non-ES LPS activated MPs is studied. From the results, a mechanism of VGIC mediation in downregulation of pro-inflammatory genes is given and it is not discussed in the current thesis while details can be found in M. Donegà's thesis.

5.4.3 Conclusions

PLGA/OECTs were used to investigate the effect of the ES onto macrophages. The powerful system that was built up for the investigation of ES onto primary neurons is demonstrated very efficient in stimulating macrophages

through VGICs. Surprisingly, PLGA/OECTs exhibit a clear effect in preventing pro-inflammatory activation of MPs. Within one hour of ES (5 seconds at 20 Hz, $1.6*10^{-3}$ μA/μm^2 cathodic first bipolar pulses every 90 seconds) the significant downregulation of 12 genes related to LPS-induced inflammation is proved. This is a very significant result also considered the viability of MPs is fully not affected by ES.

The usage of PLGA/OECTs devices and the whole setup also allowed collaborators in Cambridge to investigate the specific role of VGCCs in macrophages. In the presence of specific VGCCs blockers the ES was performed and the effects of ES in the regulation of the single genes allowed to make hypothesis about the mechanism, which is not discussed in the current thesis.

Furthermore, the proposed setup, composed of PLGA/OECTs and device holder coupled with an easy to drive ES paradigm, could be essential in further experiments towards the understanding of the possible effects of ES onto other classically non-excitable cells and could reveal possible mechanisms behind the pro-plasticity effect of ES.

Bibliography

(1) Minta, A.; Kao, J. P. Y.; Tsien, R. Y. Fluorescent Indicators for Cytosolic Calcium Based on Rhodamine and Fluorescein Chromophores. *J. Biol. Chem.* **1989**, *264*, 8171–8178.

(2) Merrill, D. R.; Bikson, M.; Jefferys, J. G. R. Electrical Stimulation of Excitable Tissue: Design of Efficacious and Safe Protocols. *J. Neurosci. Methods* **2005**, *141*, 171–198.

(3) Schoen, I.; Fromherz, P. Extracellular Stimulation of Mammalian Neurons Through Repetitive Activation of Na+ Channels by Weak Capacitive Currents on a Silicon Chip. *J. Neurophysiol.* **2008**, *100*, 346–357.

(4) Schoen, I.; Fromherz, P. The Mechanism of Extracellular Stimulation of Nerve Cells on an Electrolyte-Oxide-Semiconductor Capacitor. *Biophys. J.* **2007**, *92*, 1096–1111.

(5) Jacobs, J. M.; Meyer, T. Control of Action Potential-Induced Ca2+ Signaling in the Soma of Hippocampal Neurons by Ca2+ Release from Intracellular Stores. *J. Neurosci.* **1997**, *17*, 4129–4135.

(6) Balkowiec, A.; Katz, D. M. Cellular Mechanisms Regulating Activity-Dependent Release of Native Brain-Derived Neurotrophic Factor from

Hippocampal Neurons. *J. Neurosci.* **2002**, *22*, 10399–10407.

(7) Sandler, V. M.; Barbara, J. G. Calcium-Induced Calcium Release Contributes to Action Potential-Evoked Calcium Transients in Hippocampal CA1 Pyramidal Neurons. *J. Neurosci.* **1999**, *19*, 4325–4336.

(8) Lever, I. J.; Bradbury, E. J.; Cunningham, J. R.; Adelson, D. W.; Jones, M. G.; McMahon, S. B.; Marvizón, J. C.; Malcangio, M. Brain-Derived Neurotrophic Factor Is Released in the Dorsal Horn by Distinctive Patterns of Afferent Fiber Stimulation. *J. Neurosci.* **2001**, *21*, 4469–4477.

(9) Butterwick, A.; Vankov, A.; Huie, P.; Freyvert, Y.; Palanker, D. Tissue Damage by Pulsed Electrical Stimulation. *IEEE Trans. Biomed. Eng.* **2007**, *54*, 2261–2267.

(10) Kriegler, S.; Chiu, S. Y. Calcium Signaling of Glial Cells along Mammalian Axons. *J. Neurosci.* **1993**, *13*, 4229–4245.

(11) Feedar, J. a; Kloth, L. C.; Gentzkow, G. D. Chronic Dermal Ulcer Healing Enhanced with Monophasic Pulsed Electrical Stimulation. *Phys. Ther.* **1991**, *71*, 639–649.

(12) Zhao, M.; Bai, H.; Wang, E.; Forrester, J. V.; McCaig, C. D. Electrical Stimulation Directly Induces Pre-Angiogenic Responses in Vascular Endothelial Cells by Signaling through VEGF Receptors. *J Cell Sci.* **2004**, *117*, 397–405.

(13) Shi, G.; Zhang, Z.; Rouabhia, M. The Regulation of Cell Functions Electrically Using Biodegradable Polypyrrole-Polylactide Conductors. *Biomaterials* **2008**, *29*, 3792–3798.

(14) Thompson, D. M.; Koppes, A. N.; Hardy, J. G.; Schmidt, C. E. Electrical Stimuli in the Central Nervous System Microenvironment. *Annu. Rev. Biomed. Eng.* **2014**, *16*, 397–430.

(15) McCaig, C. D.; Rajnicek, A. M.; Song, B.; Zhao, M. Controlling Cell Behavior Electrically: Current Views and Future Potential. *Physiol. Rev.* **2005**, *85*, 943–978.

chapter 6

Fabrication and Characterization of the Implantable Device

An implantable, largely biodegradable and fully biocompatible, device is presented in this chapter. The device, termed AMID (active multifunctional implantable device), contains a microfluidic channel for the local delivery of fluid, as well as four transistors and electrodes for the delivery of electrical stimuli. Its dimensions and shape make the device specifically targeted for the treatment of spinal cord injury in mouse/rat animal models. However, its versatile fabrication strategy allows fast prototyping to be easily tailored to different medical needs.

6.1 Introduction

Implantable neuroprostheses are specifically designed objects to study and treat the injured nervous system. The field is rising both in terms of numbers of potential applications and in terms of the complexity of the developed devices. New technologies to design multimodal neural implants were recently developed and engineered. However, the upgrade of these sophisticated technologies into therapeutic devices has yet to be achieved. A recurring challenge towards the biointegration is the mechanical matching between soft neural tissues and the implants. The device has to minimize the invasiveness and to guarantee the operational stability for the time required for the therapy while being subject to strong mechanical stresses.

The device envisioned within the i-ONE project (AMID) is multifunctional since it integrates local delivery of fluids (e.g. drugs, growth factors, antibiotics and anti-inflammatory) together with electrical stimulation (ES). In Chapter 5, the efficacy of ES by means of OECTs onto primary neurons and macrophages was demonstrated but for *in vivo* implantation the requirements are different and more stringent. The device complexity is increased with respect to *in vitro* configuration. The active region is miniaturized and has to contain different devices as different sectors of the spinal cord (SC) needs to be stimulated in order to address motor neurons. Shape and dimensions are related to the targeted spinal cord segment and to the chosen animal model and must be viable for the implantation surgery technique. After implantation, the AMID has to be connected to external electronics. The preferred architecture would have power supply, front-end electronics and wireless communication system to avoid cables to the outside of the body. However, although few pioneering works appeared recently in scientific literature[1,2], the integrated technology in bioelectronics is not mature yet. Since AMID includes a microfluidic system, which implies inlet tubes used to inject drugs from the outside body, the easier strategy is to provide to the AMID also an

electrical connector to be easily plugged to the external control and power-supply system when needed. The device has to integrate highly sensitive transducers for the monitoring of the regeneration status and this is probably the most complicated technological step. As already reviewed, development of sensitive transducers of bioelectric signals are at the frontier of the research in bioelectronics and the vision of integrating them in an implantable multifunctional device is very ambitious. Devices, both for stimulation and for recording, have to be arranged onto a specific area and miniaturized. Last but not least, the device has to be made of highly biocompatible and possibly biodegradable materials. Biocompatibility is necessary since the adverse foreign body reaction (FBR) that a non-biocompatible material could generate will lead to device failure upon coating sheath created by cells of the immune system (Section 2.6). Biodegradability is highly desirable characteristic because of several reasons. It opens to transient electronics that stands and operates for the time targeted to the therapy only, thus reducing the possibility of inducing long-term FBR. Furthermore, with a biodegradable transient device, the surgery for the removal of the implant would not be necessary. Considering fragility of the spinal cord, this approach would be advantageous.

The resulting device is technologically an advanced product. Several layers and different materials with small patterned features are necessary. The device can be subjected to adjustments in order to address different spinal cord regions, different animal models, which implies different dimensions (the device for humans will be less stringent in terms of miniaturization requirements) and increasing or adapting the multiple existent functionalities. That is why a highly versatile fabrication strategy is among the desirable characteristics. This could allow changes that are inevitably necessary in the prototyping phase, without the need to change the fabrication strategy.

The fabrication strategy that led to the final AMID as used in the *in vivo* experiments is presented in this Chapter.

6.2 Experimental section

AMID is a complex multilayer device. The fabrication protocol is based on the inversed fabrication technique presented in Section 3.5. On a microscopy glass slide, a sacrificial water-soluble layer is deposited on which the fabrication is performed[3]. A thin gold layer is evaporated and patterned by means of an IR-laser marker and the poly(lactic-co-glycolic) acid (PLGA) is then casted atop. The microfluidic, also made of PLGA, is fabricated independently with replica molding technique. Then, it is sealed by means of a heating procedure to the PLGA scaffold. Up to three AMIDs can be fabricated on top of a single microscopy glass slide and the procedure can be further up-scaled. The release of the devices is induced by immersion of the whole slide inside a beaker containing pure water and it occurs within 12 hours. Then, an encapsulation PLGA layer is sealed on the surface in order to better confine the stimuli and to protect the gold leads. The PEDOT:PSS semiconductor is spun and it is then patterned with a soft lithographic technique. In the **Figure 1** a schematic of the experimental procedure is given.

The device is then shaped and a system to provide external electrical connections is fixed. Two different kinds of devices were supplied to the collaborators at University of Cambridge. The first implies the implantation of the biodegradable part of the device only with the elongated tail coming outside the skin to be bound to a rigid plastic connector. The second is more robust and implies the usage of a smaller connector to bind the AMID to an extension cable. The last (non-biodegradable) runs under the skin of the mouse' back. The cable comes out from a head helmet attached on the mouse skull. In close contact with the fragile spinal cord, the AMID biodegradability >99% is maintained. In this second case, a surgery to remove the connector is needed but its invasiveness is very low and the risks of inducing damages to the SC are prevented.

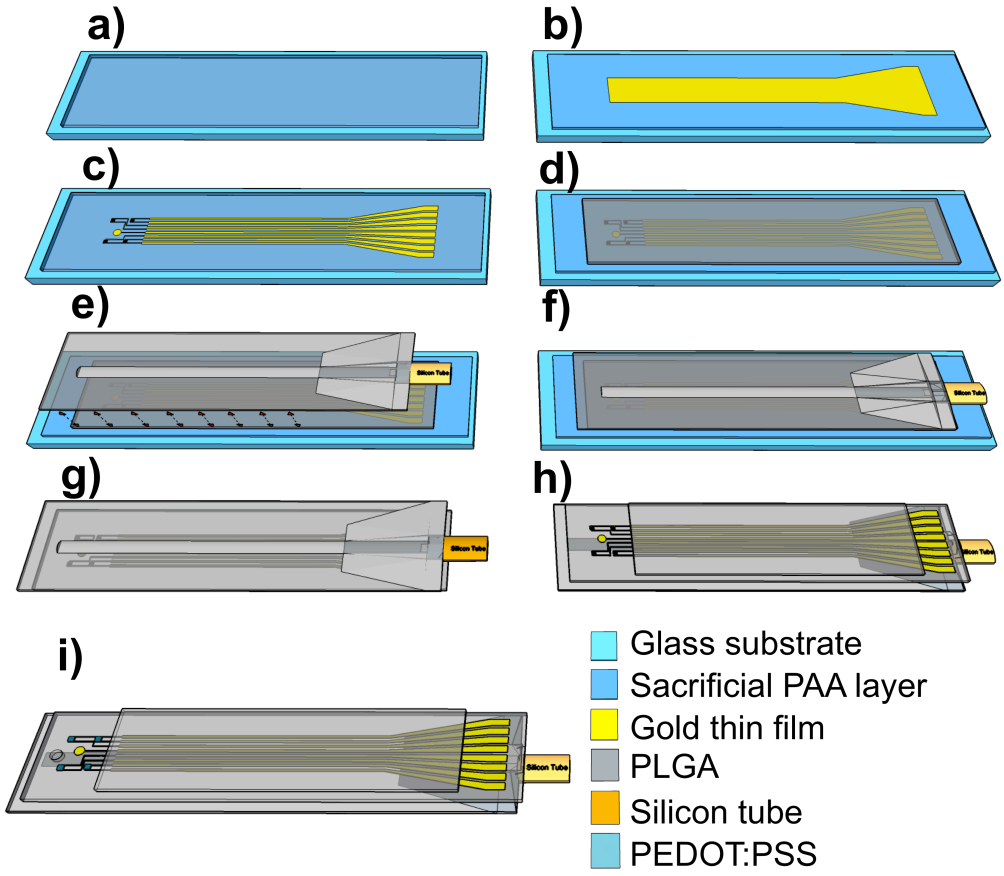

Figure 1 Schematic of AMID simplified fabrication strategy scheme. **a)** PAA sacrificial transparent layer deposited onto the microscopy glass slide. **b)** Gold is evaporated through a shadow mask and it is patterned by means of an IR-laser marker to obtain **c)**. The PLGA is then casted atop, **d)**. A microfluidic system, made of PLGA and fabricated separately, is sealed on the back of the casted PLGA (**e)**) to get **f)**. The release of the PLGA with the gold pattern attached is induced by immersion in water and the freestanding **g)** is obtained. Then, an encapsulation protective PLGA layer is sealed on the surface to cover the gold leads **h)**. In **i)** the microfluidic outlet is opened and the PEDOT:PSS patterned on top of the interdigitated electrodes. The shaping only is missing in this sketch. Several steps of this fabrication strategy can be swapped and the order changed.

The detailed fabrication strategy, step-by-step, is described below and the electrical characterization is given.

6.2.1 AMID fabrication strategy

Sacrificial layer fabrication:

Microscopy glass slides are sonicated in acetone (pure grade) and isopropanol (pure grade) for 8 minutes each and then are subsequently dried with N_2 stream. The glass slides are then functionalized by immersion in 1 mM (3-aminopropyl)-triethoxysilane (APTES, Sigma Aldrich, 99%) solution in ethanol for 45 minutes. A rinse with ethanol and drying with N_2 stream are the final steps prior to the controlled deposition of a PAA (Sigma Aldrich, 35 wt. % in H_2O, MW = 100 kDa) film. In particular PAA, 5%(v/v) in water, is spun with the following procedure: i) 500 rpm for 3 sec and ii) 2000 rpm for 20 sec. After a baking of 20 min at 140 °C, a second layer of neutralized PAA (by means of sodium hydroxide, NaOH, aliquots) 3% (v/v) is spun at 500 rpm for 3 sec and 1800 rpm for 20 sec. A final baking is performed for 20 min at 120 °C. The thickness of the sacrificial layers is around 500 nm.

Au deposition through the shadow mask:

Mask for Au deposition, termed shadow masks, are fabricated by means of laser cut. The MarKo 10P© laser marker (by LaserPoint) is used to cut a 100 μm thick aluminium foil following a computer assisted drawing (CAD). The microscopy glass slide coated with PAA is fixed on the mask and 75 nm of gold are evaporated in a high vacuum chamber at a pressure of 10^{-7} mbar and a rate of 1 Å/s. The mask shadowing during gold evaporation reduces the time of the ablation process needed to remove the metal excess.

Au patterning by laser-scan ablation:

A laser ablation procedure (already described in Chapter 3) is used to define gold pads, leads and electrodes. Ablation parameters are: power of 160 mW with pulse width of 10 ns and 22000 Hz frequencies. Thanks to

the high prototyping speed and versatility offered by the technique, different geometries were tested. Here is reported the optimized one. The overall geometry is elongated in order to separate the small active area (1x1 mm^2) that has to interface the injured region, from the pads to provide external electrical connection. 8 leads (about 2.5 cm long) connect the 4 interdigitated couples of source and drain electrodes plus a circular electrode placed in the centre of the active area with the pads (**Figure 2**). The circular electrode can be used as gate electrode of the organic transistor and/or as an independent electrode. The W/L of each pair of interdigitated electrodes is 150. On each microscopy glass slide, up to three identical patterns can be drawn. Each of them will be part of a single AMID. The alignment of the ablation pattern with the gold pattern previously achieved by masking is doable because of the camera focused onto the stage and connected to the computer.

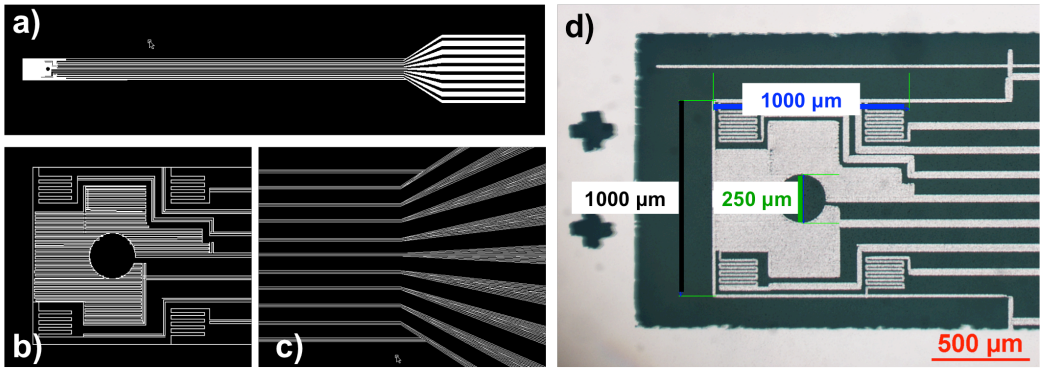

Figure 2 a), b) and **c)** details of the computer assisted drawing file to drive the motors of the ScibaR IR-laser marker. **d)** optical transmission microscopy image of the ablation onto PAA. Au film appears green. Channel length between the interdigitated couples of electrodes is 12 µm.

Substrate casting

A silicon pool (Sigma, coverslip for microscope glass slide, 2.2 cm x 5.0 cm) is fixed onto the microscopy glass slide coated with PAA and the gold pattern. 1 mL of 5% PLGA solution in dichloromethane (prior stirred for 30

min) is cast into the pool. The microscopy glass carrier is placed in the oven for 5 hours at 55 °C to let the solvent evaporate.

Pattern release

The whole sandwich is immersed into a petri dish with pure water to dissolve the sacrificial layer. A complete transfer and release of Au pattern from PAA to PLGA is achieved in about 12 hours of immersion. Residual PAA from the PLGA/Au film is removed by rinsing abundantly with pure water. The released structure is left in the oven at 35°C for 2 h.

Lamination of a protective layer

The protective layer is added to better confine electrical stimuli. It is prior fabricated by drop casting on a microscopy glass slide by confining 1 mL of 1% PLGA solution in dichloromethane into a PDMS pool (Sigma, coverslip for microscope glass slide, 2.2 cm x 5.0 cm) and heating for 5 hours at 55 °C to let the solvent evaporate. Its release is induced by immersion in pure water for less then 10 minutes. Then, it is positioned on top the gold patterned film under a stereoscope. The thin PLGA film is aligned to cover the gold leads from the edge with the interdigitated part to the larger back end, 2 mm far from the pads edge. It is sealed by heating on a hot plate (covered with paper) at 60 °C and pressing with flat-tip tweezers. Pressing 5 seconds in each zone is enough to stick the two layers. This is termed PLGA/Au/PLGA layer. This procedure is necessary to confine the stimuli delivered *in vivo* by exposing to liquid only the active area of the device.

PEDOT:PSS coating and patterning

The PLGA/Au/PLGA layer is adhered, with gold interdigitated electrodes exposed to air, to a glass slide by wetting the glass with a few droplets of water. PEDOT:PSS (Clevios™ P Jet N V2) suspension (5 µL as final

volume), with added 0.2% Silquest (3-glycidoxypropyltrimethoxysilane) and 5% DMSO, is spin coated on the interdigitated electrodes. Coating standard parameters are: 500 rpm for 3 sec and 2200 rpm for 20 sec. The samples are then dried in an oven at 45 °C for 24 h. Devices can be operated, without patterning of the semiconductor, with an external gate electrode. For a better and more independent operation, patterning of the semiconductor has to be performed as illustrated in **Figure 3**. The design of the procedure is a result of the collaboration between myself, Dr. T. Cramer, Dr. M. Murgia and Dr. D Gentili (expert in soft lithography). The technique is based on local oxidant-induced disruption of electrical conductivity of PEDOT:PSS[4]. The oxidation is performed with sodium hypochlorite (NaClO) and a stamp is used to absorb the chemical and to release it locally[5]. A photolithographic mask is fabricated onto commercial silver mirrors by laser-assisted marker using the MarKo 10P© or ScribaR**.** A standard photolithographic process is used to fabricate an SU-8 master onto a Si/SiO_x native substrate. The master consists of 4 SU-8 squares (400μm x 400μm), 10μm thick each. Agarose stamp is prepared as follows. A 3%($^{w}/_{w}$) dispersion of Agarose (D5 High gel strength, Condalab) in deionized water is heated at 120°C for 30 min in a falcon tube and shaken every 10 min. The resulting warm, clear and bubble-free solution is poured on the master in a closed petri dish. The stamp is left to cool and, when at room temperature, it is ready to be used. It can be cut in order to reduce the dimensions and facilitate the handing. It is very fragile and the usage of flat-tip tweezers is recommended to detach and manipulate the stamp that contains 4 dug cuboids with dimensions 400 x 400 x 10 μm^3. The agarose stamp is pasted on a glass slide with cyanoacrylate adhesive layer in order to facilitate the usage. The stamp is soaked in 1% NaClO aqueous solution for 5 minutes and gently then streamed with N_2 for 20 second. The stamp, still saturated, is pressed onto the PEDOT:PSS film for 10 seconds. Then it is removed and the substrate is washed abundantly with pure water. The precise positioning of the agarose stamp with respect the Au/PEDOT:PSS pattern is achieved

by a x-y-z stage. The sample is placed onto the stage (x-y fine movement controlled) while the stamp, face down, is attached on the second stage, controlled in z-axis. Thanks to the transparency, the alignment is performed manually. The position monitoring is achieved by means of an optical microscope fixed on the z-axis above the transparent stage.

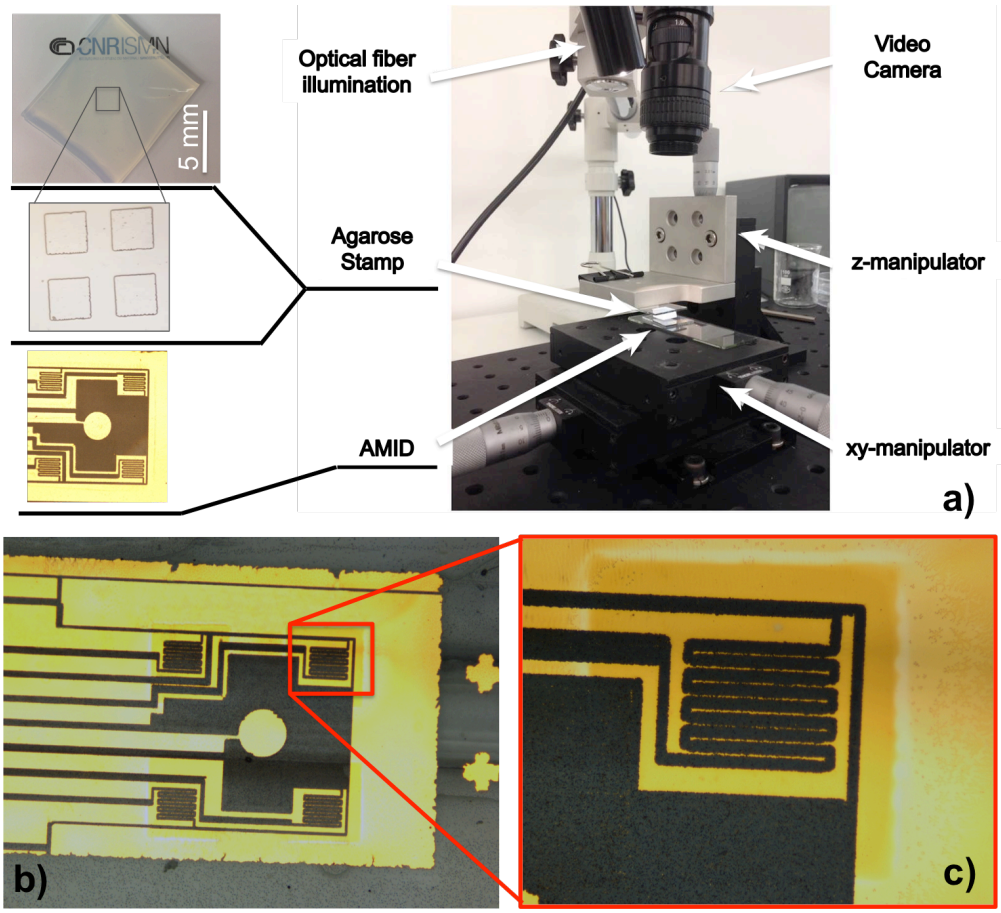

Figure 3 a) Reports the apparatus used for the patterning of PEDOT:PSS film spun onto the AMID. On the stage mounted onto an x-y manipulator, the AMID is placed. The agarose stamp (picture and optical microscopy image) reported on the top left is fixed, face down, onto the z manipulator. Dug cuboids have 400 μm long sides. **b)** and **c)** are optical images at different magnification of the patterned AMID. The darker yellow regions evidence the zones where PEDOT:PSS conductivity is preserved.

Microfluidics fabrication

The microfluidics system has been developed by Dr. Pierpaolo Greco, Dr. Giulia Foschi (both at Scriba Nanotecnologie Srl) and me. It is produced with a technique termed “replica molding”. A MarKo 10P© laser marker is used to engrave a stainless steel slide. The design is a 2.8 cm long and 350 μm large channel that ends with a larger entrance and an outer frame of 3.5 cm x 0.9 cm. The microfluidic master is then embossed on a polypropylene substrate by pressing at 160 psi (pound per square inch, around 11 kg/cm^2) at 90 °C for 4 minutes. This master is then covered with 0.5 mL of 5% PLGA solution in dichloromethane (prior stirred for 30 min) and then dried in the oven for 5 hours. With a pair of tweezers, the film, of a thickness of less then 100 μm, is removed. The microfluidic channel is about 100 μm wide and 60 μm high. Then, a second layer of thin PLGA is sealed on the upper part of the first and a silicon medical grade tube (internal diameter 300 μm) is embedded and trapped in it. The thickness of the second layer of PLGA is about 50 μm. It is obtained by performing the drop casting technique on a microscopy glass slide by confining the 1 mL of 2% PLGA solution in dichloromethane into a PDMS pool (Sigma, coverslip for microscope glass slide, 2.2 cm x 5.0 cm) and heating for 5 hours at 55 °C to let the solvent evaporate. The sealing procedure occurs by heating on a hot plate (or with a dedicated press with a thermal controller) at temperatures of 65 °C and by pressing locally where the two layers have to be adhered. Around the silicon tube, few microliters of PDMS (Sylgard® 184, purchased by Dow Corning, base:curing agent, 10:1) are gently spread in order to ensure higher adhesion between the external tube and the microfluidic system. Two days at room temperature are needed to complete the curing of PDMS. **Figure 4a** shows the positioning of the second transparent layer, which ensures independent inlet for the microfluidic in the final AMID.

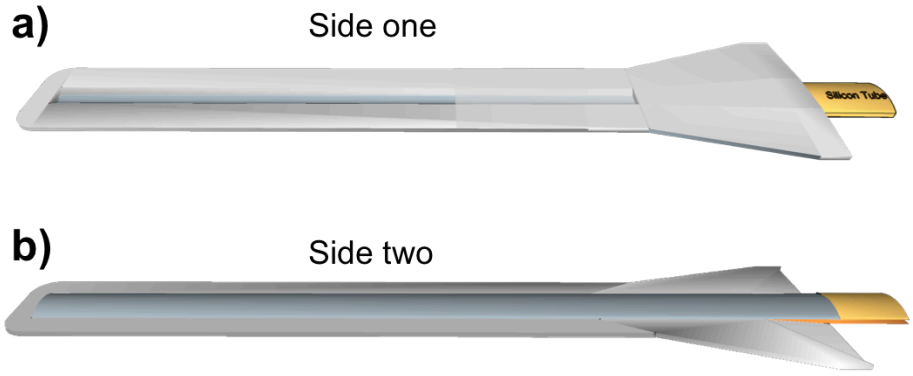

Figure 4 a) and **b)** report two views of the microfluidic channel made of PLGA. The side one, containing a concave channel, faces the back of the PLGA layer containing the gold pattern. The channel, on the side of the silicon tube, is partially covered and sealed by a thin PLGA film while the other part (the left one) at this step is fully opened. A protruding channel characterizes the side two in **b)**. For an easier interpretation, the microfluidic is already shaped like the final AMID in this scheme.

Microfluidics integration

Microfluidic integration occurs by sealing the microfluidic system with the PLGA/Au/PLGA layer. This is a critical step because of the alignment of the microfluidic with the gold pattern and because, in order to maintain separate back ends for independent microfluidic inlet and electrical connections, the sealing procedure involves one side only. In order to avoid the full sealing, a piece of white paper is temporary placed between the PLGA/Au layer and the microfluidic layer close to the end. Then, the alignment is performed under a stereoscope. The gold leads patterned on the first layer, have to be precisely aligned with the microfluidic layer. When the two layers are well overlapped, the sealing occurs onto the hot plate (covered with paper) at 60 °C by pressing with flat-tip tweezers on the edge, very close to the microfluidic channel. The full sealing takes around 2 minutes. If the temperature is well set, 5 seconds of pressing on each region are enough to stick together the two layers. During this

operation, having the gold pattern face down, while microfluidic back is faced up, is recommended. This avoids heat-induced channel collapse. Then, the outlet microfluidic is created. This procedure is performed manually by pressing, under the stereoscope, an insulin syringe needle onto the top PLGA layer, around 500 µm far from the interdigitated electrodes. The diameter of the formed outlet is about 200 µm.

Figure 5 reports an exploded scheme of the layer AMID is made of.

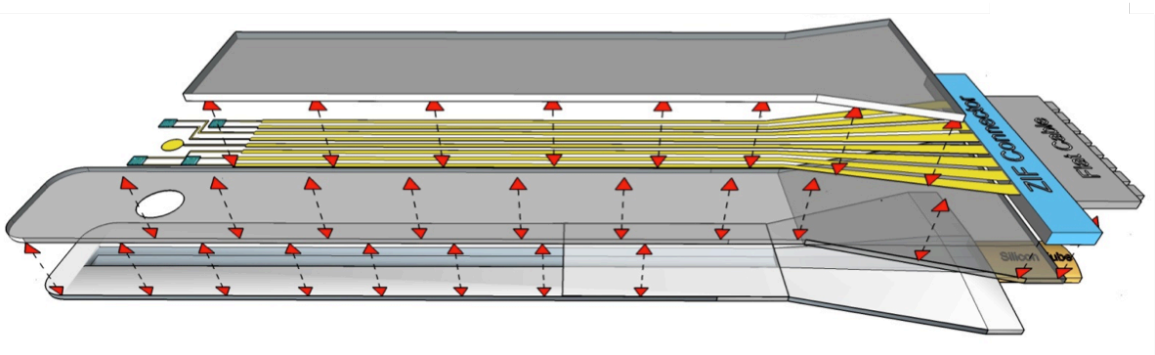

Figure 5 The single layers forming the AMID are exploded in this scheme. The red arrows indicate the regions where the layers are in contact or sealed. This figure put the evidence on the separation of the microfluidic PLGA layer and the gold patterned PLGA layer on the right side. This provides independent back ends and simplifies electrical connection.

Shaping the AMID

The AMID is finally cut into the desired shape. Several different dimensions and shapes were tested. The most suitable for the SCI treatment in rats is the one reported in the **Figure 5**, **6** and **7**. The PLGA layer is trimmed close to the sides of the gold pattern around the pads and the leads. The total length is 3.5 cm. The preferred cutting tool for the AMID are sharp small scissors. Two small wings are shaped close to the back end tail, one for each side that help the manipulation during the

surgical operations. The surgeon then cuts the wings during the implantation procedure, when they are not needed.

Electrical Connections

Electrical connection between the device and external SMU is critical. Generally, ZIF (zero insertion force) connectors are used to bind the pads of the device. On the other side of the ZIF, generally used for standard electronics, small pins have to be somehow connected to flat cable to provide flexibility where needed, then to coaxial cables and finally, with a BNC connector, to the SMU.

We shaped two AMID architectures, the first considers the implantation of thin part of the AMID only with the ZIF connector placed outside the mouse/rat back. The advantages of this configuration reside on the very high biodegradability of the whole implanted structure and on the absence of stringent limitation on the ZIF dimension. The drawback is the very high fragility when the mouse/rat moves. This configuration is used in this thesis for the electrophysiology in acute. The AMID is inserted and fixed into the ZIF, 1 cm wide. The pins of the opposite side of the ZIF are about 1 mm far one from the other and soldering them with the pins of a second ZIF of the same dimensions is possible. The last is then plugged upon needs to a flat cable converted into 8 coaxial cables to be plugged to the Multiplexer (MPX described in Section 5.2.3) or directly to the SMU.

The second approach implies the implantation of the ZIF and part of the flat cable as well. Obviously, only the biodegradable part with the active layers is placed to interface the injury under the dura mater. On the contrary, the non-biodegradable region (ZIF and flat cable) runs more dorsal, just under the skin level. This approach is extremely advantageous. Indeed, the device is less subject to torsional and mechanical stresses. Furthermore, the electrical connectors and microfluidics inlet can come out from the skull where a head connector is

secured. The discomfort for the animal is sensitively reduced. In this case, the ZIF has to be smaller, 0.5 cm wide. However, due to miniaturization, soldering ZIF pins on the flat cable has to be excluded. In order to circumvent this issue, a stratagem is used. The ZIF is used as a clip only to achieve connection between each of the pads on the AMID and each lead of a thin flat cable. Then, the small flat cable can be plugged upon needs with a dedicated connector to end with the 8 coaxial BNC cables. In detail the connection procedure consists of the following steps. The ZIF is opened and the device inserted with the gold contacts pads faced up. Then, the flat cable, with the metal leads faced down, is inserted and each of the 8 connections has to be perfectly aligned. Then, when the positioning is over, the ZIF is closed. At this point, the ZIF and the flat cable are one on top of the other, in a totally unsuitable position. To solve this, the flat cable, as closest as possible to the ZIF is bended resulting in a rotation of 180° in order to be along the same axis with the AMID. To fix the flat cable is this position cyanoacrylate adhesive is used. Few microliter are deposited on the ZIF, the flat cable placed and let it dry for 20 minutes with a crocodile clip in order to maintain the positioning.

Encapsulation of contacts

In the second approach, (i.e. small ZIF is intended to be implanted) one has to guarantee that metallic parts from the ZIF connector or the flat cable are not exposed to the liquid to prevent parasitic currents. When the electrical connection is closed, medical grade silicon (140 RTV COATING, Dow Corning) is spread with a spatula around the ZIF connector and around the first mm of the AMID to form a thin but tight encapsulation layer. This silicone is dedicated to this purpose and it allows stimuli confinement. In this way, the 1x1 mm^2 area, where the active devices are patterned, is the only non-insulated region exposed to electrophysiological environment. After 24 hours, upon proper sterilization, the AMID is ready to be implanted.

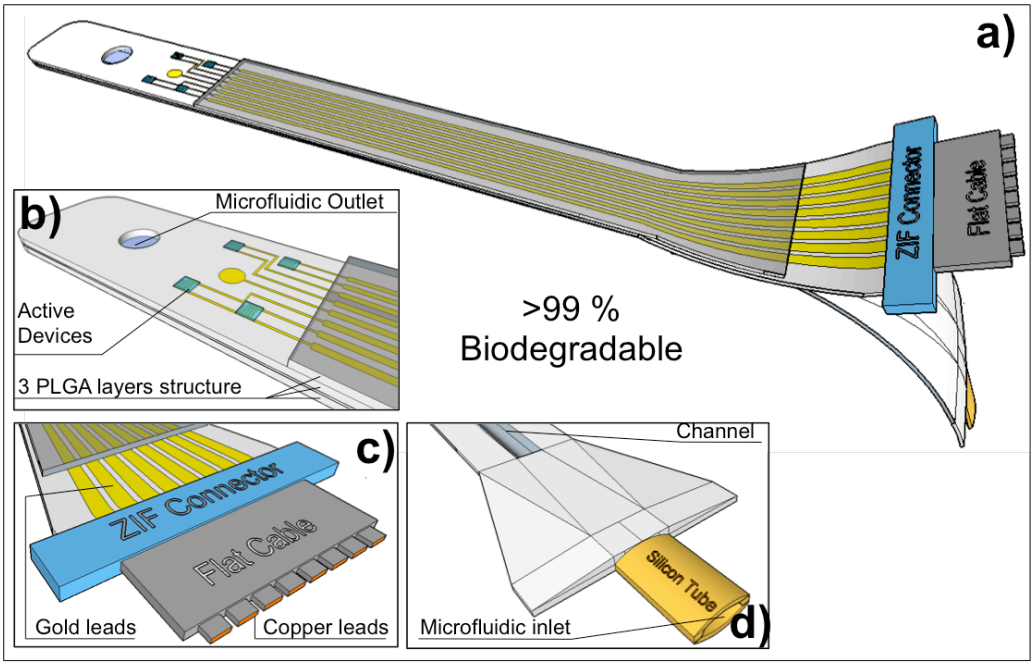

Figure 6 a) Full sketch of the final AMID with insets of the details: **a)** active region, **c)** ZIF connector and **d)** microfluidic inlet.

Many steps of the described fabrication can be swapped. Two examples are given: i) microfluidic sealing can occur before or after substrate release and ii) spinning and patterning of PEDOT:PSS can occur before or after application of the protective layer.

Software

The software to drive the AMID is the same already presented in Section 5.2.3.

Pictures of the final AMID are reported in **Figure 7**.

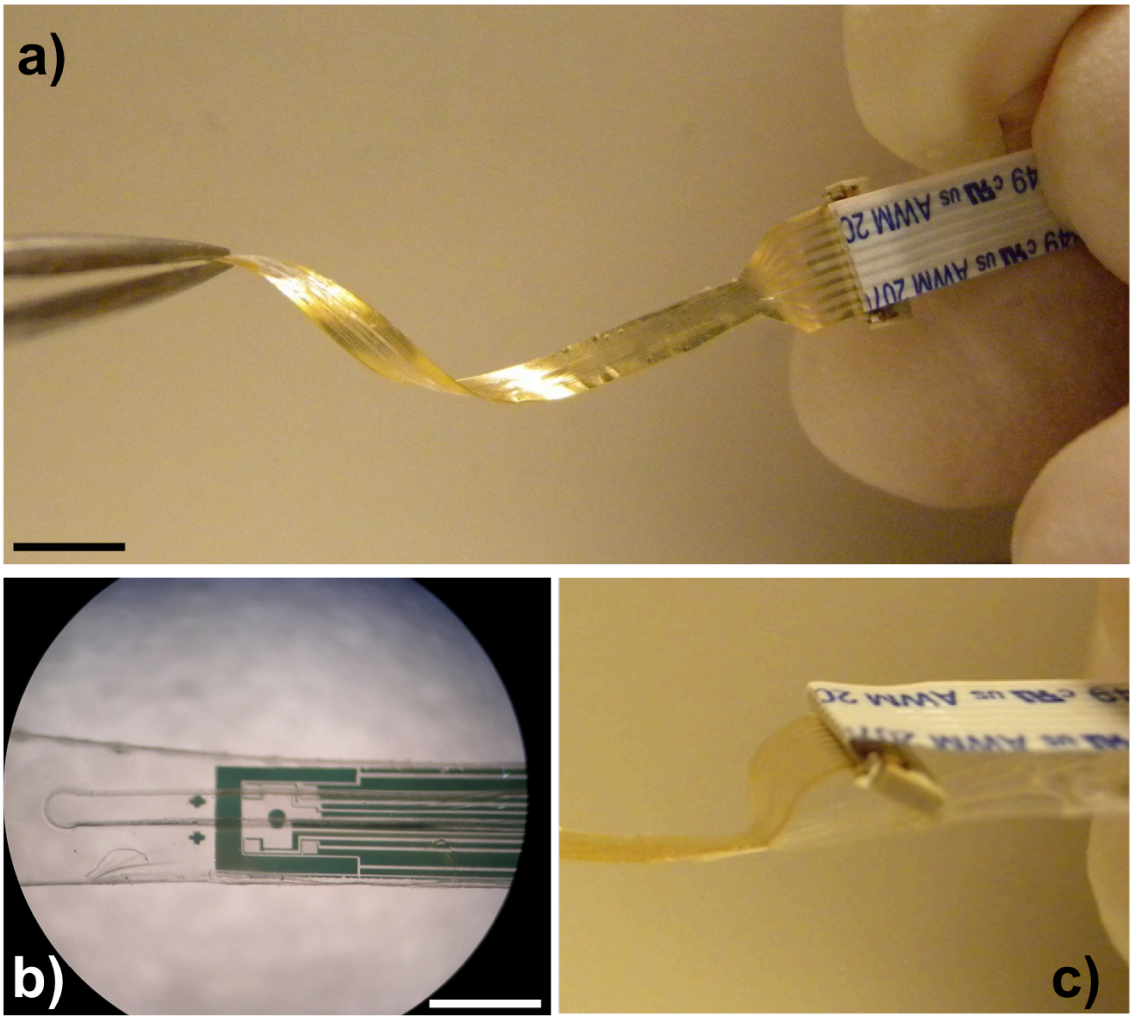

Figure 7 Pictures of a real AMID. In **a)** the scale bar is 5 mm while in **b)** it is 1 mm. In **c)** the separation of the back ends is emphasised.

6.2.2 AMID Electrical Characterization

Electrical performances of the AMID are presented. Characterization of each of OECTs before and after the patterning of the semiconductor is performed with an Ag/AgCl gate electrode immersed in a cell culture medium in the incubator at 37 °C. The **Figure 8 a**, **b** and **c** show the characterization of the non-patterned AMID. When PEDOT:PSS film is uniformly deposited all over the 1x1 mm^2 area where the 4 OECTs are patterned, the devices are extremely stable and the loss of

transconductance within six days of operation is negligible (1.5 mS vs 1.4 mS). The potentiometric sensitivity is about 100 µV.

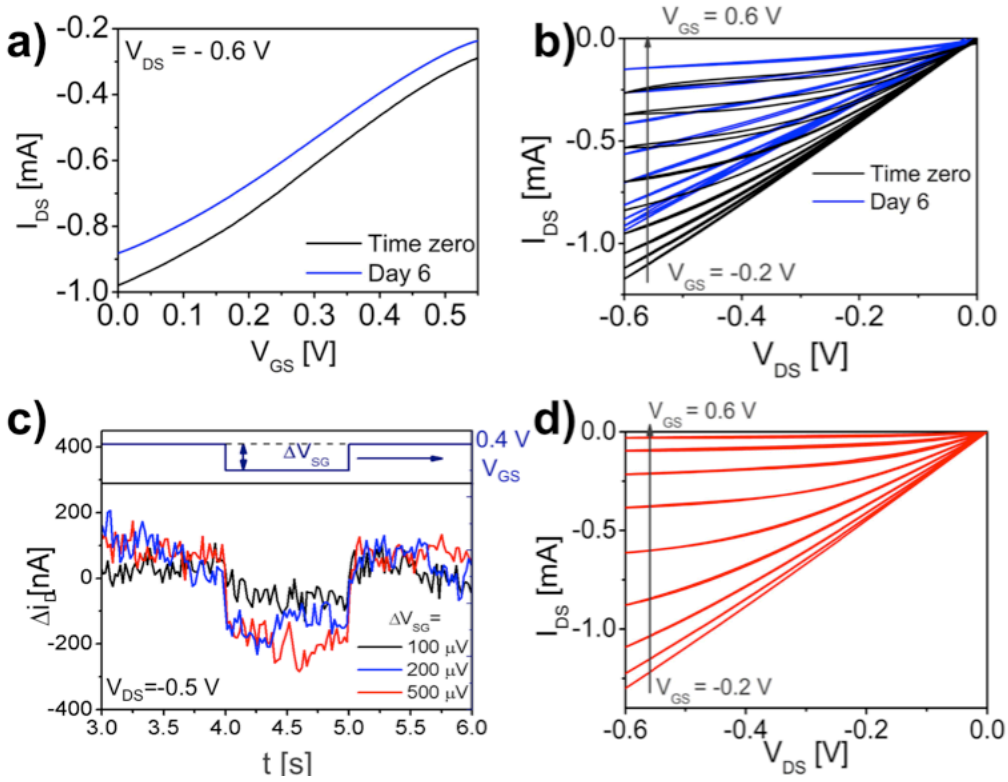

Figure 8 a) transfer curve, **b)** output curve and **c)** potentiometric sensitivity test (at time zero) of the non-patterned PEDOT:PSS based OECTs on the AMID. **d)** The output of a typical OECTs patterned onto the AMID.

On the other side, performances of the patterned OECTs, are very unstable and devices rapidly degrade when characterized either with an external gate electrode (Ag/AgCl or Pt) or by using as gate the circular central electrode or pairs of other electrodes on the surface. The source/drain current, during transistor characterization, diminishes (until being comparable with the leakage current) within minutes. However, the best performances both in terms of current saturation and in terms of off current of the patterned device are worth to be shown (**Figure 8d**). The nature of such unstable behaviour was not investigated, although it can be ascribed to delamination of the semiconductor when confined in smaller

area or difficulty in washing away the sodium hypochlorite used as oxidizers.

6.2.3 Stimulation Protocol

Due to instability issues of patterned semiconductor, electrical stimulations are performed by using AMID with chemically over-oxidised (deactivated) PEDOT:PSS layer. In this way, AMID thickness, shape, configuration and most of the materials are suitable for the implantation and even if the stability issues remain, this AMID allows us to start preliminary *in* vivo test while working in parallel on the semiconductor patterning. Electrical pulses shape, intensity and speed are based on the protocols developed *in vitro* and typical pulses are reported in **Figure 9**. Pulses are applied between pairs of electrodes on the surface by directly connecting the BNCs to SMU channel. Each electrode is numbered and the cathodic first pulse is applied to the electrode connected to the Hi channel of the SMU. Positioning of the electrodes enables to test different geometries during the stimulation and to verify the physiological effect of exciting different regions. The injected current density is calculated by extracting the exposed area of the biased electrodes considering the presence of the encapsulation PLGA layer.

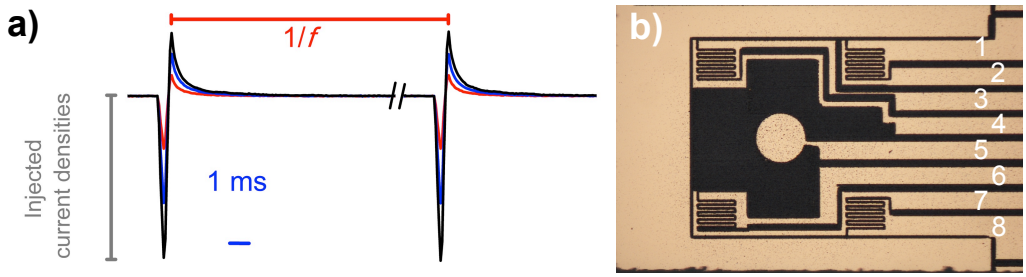

Figure 9 Shape of electrical stimuli of different intensities in physiological environment (**a**). The amount of injected and extracted charges is comparable. Stimuli are applied between couples of electrodes on the AMID (**b**).

In vivo different stimulation timings are investigated depending of the targeted experiment. Single pulses or 5 seconds bursts at higher frequency (up to 50 Hz) are used to find the threshold. Long-term stimulations are applied with the protocol adopted *in vitro*: one-hour with 40 bursts where each burst stands for 5 seconds at fix frequency.

6.3 Conclusions

A multifunctional implantable device (AMID) has been demonstrated. The device integrates a microfluidic channel specifically design for the local delivery of fluids onto the injured region of the spinal cord. The device contains four OECTs that, if characterized with an external gate electrode, exhibits good performances. The current modulation is high, hysteresis modest and the potentiometric sensitivity in the microvolt range is enabled. The stability of the device, upon continuous operation in cell culture medium, is high and within six days the performances only slightly decrease. For a sensing and stimulation of different regions by means of organic semiconductor, its patterning is needed. Even if we achieved the patterning, stability of patterned OECTs is not high enough to guarantee continuous operation *in vivo*. Therefore, current AMID configuration does not enable sensing by means of OECTs. Patterning of the semiconductor can be achieved by means of different strategies (e.g. ink-jet printing, laser patterning or other dry etching techniques) that could increase device stability. AMID allows continuous stable application of fast bipolar pulse stimuli with over oxidized PEDOT:PSS in physiological environment. The developed fabrication strategy leads to a complex multifunctional device, which is almost fully biodegradable (>99% in the active region in contact with the central nervous system) and fully biocompatible. Thanks to prototyping, other AMID shaping and electrodes geometries can be fabricated to meet both the requirements for a safe implantation and the electrophysiological needs. The fabrication is based on different steps to allow future researchers and developers to easily change step

characteristics and conditions in order to increase device functionality. The final platform is highly versatile and its application is presented in the Chapter 7.

Bibliography

(1) Zheng, Q.; Zou, Y.; Zhang, Y.; Liu, Z.; Shi, B.; Wang, X.; Jin, Y.; Ouyang, H.; Li, Z.; Wang, Z. L. Biodegradable Triboelectric Nanogenerator as a Life-Time Designed Implantable Power Source. *Sci. Adv.* **2016**, *2*, 1–10.

(2) Hwang, S.-W.; Tao, H.; Kim, D.-H.; Cheng, H.; Song, J.-K.; Rill, E.; Brenckle, M. a; Panilaitis, B.; Won, S. M.; Kim, Y.-S.; *et al.* A Physically Transient Form of Silicon Electronics. *Science (80-.).* **2012**, *337*, 1640–1644.

(3) Linder, V.; Gates, B. D.; Ryan, D.; Parviz, B. a; Whitesides, G. M. Water-Soluble Sacrificial Layers for Surface Micromachining. *Small* **2005**, *1*, 730–736.

(4) Oostra, a J.; van den Bos, K. H. W.; Blom, P. W. M.; Michels, J. J. Disruption of the Electrical Conductivity of Highly Conductive poly(3,4-Ethylenedioxythiophene):poly(styrene Sulfonate) by Hypochlorite. *J. Phys. Chem. B* **2013**, *117*, 10929–10935.

(5) Hansen, T. S.; West, K.; Hassager, O.; Larsen, N. B. Direct Fast Patterning of Conductive Polymers Using Agarose Stamping. *Adv. Mater.* **2007**, *19*, 3261–3265.

chapter 7

In vivo Acute Stimulation and Subacute AMID Integration

Preliminary *in vivo* experiments are reported. The epidural electrical stimulation is applied onto healthy and injured mouse and rats in order to demonstrate AMID efficacy in delivery electrical stimuli. Monitoring of the effects is performed both with standard electrophysiology and with investigation of early genes activation. The second part of the chapter is dedicated to the implantation of AMID onto rats SCI model towards the demonstration of device and implantation protocol safety.

Within this chapter are presented the experiments performed *in vivo*. Up to now, both a part in acute and in subacute are investigated. Epidural electrical stimulation (EES) in acute is performed both on mouse and on rats while subacute implantation onto healthy rats is a necessary step to investigate possible detrimental effects induced by the implant.

The investigation is not complete, however, interesting results emerged from the firsts experiments, which are worth to be shown.

7.1 *In* vivo Electrical Stimulation in Acute: an Introduction

As envisioned by the i-ONE project, the proposed therapy consists both on the local delivery of fluids (e.g. drugs, growth factors, antibiotics and anti-inflammatory) and on the electrical stimulation. Even if complicated from the point of view of the fabrication of the device, the local delivery of drugs is straightforward and no particular drawbacks or bottlenecks are expected. Differently, the ES is trickier and before its application in subacute SCI, several experiments have to be performed. In Chapter 5, the efficacy of ES by means of OECTs onto primary neurons and macrophages was demonstrated. However *in vivo* implantation sets different requirements. To be targeted are not specific cells cultured onto the devices but complex and not easy accessible living tissues. Furthermore, device complexity is increased since the AMID has to be implanted while stimulation driven from outside.

Firstly, the effective capability of the AMID to deliver physiologically relevant electrical stimuli to the interfaced tissues is tested. Then, finding the optimal stimulation protocol is necessary. Indeed, depending on the electrodes configuration, positioning and stimulation parameters, different structures and fibres of the SC are activated. When the intraspinal electrical stimulation (ISS) is performed, if stimuli are applied to the dorsolateral funiculus (DLF, 0.5-10 mm from the surface between L1 and L3)[1] or in the ventral horn of the lumbo-sacral grey matter (close to

laminae VII-IX)[2], stepping like movements are induced. On the contrary, no stepping is easily induced if the stimulation takes place in the dorsal-middle grey matter[3].

The usage of epidural or subdural electrodes involve all the tissues layers and structures above the spinal canal like vertebral bones, spinal cord, epidural fat etc. Conductance of the different tissues is different. Most of the structures have a very low conductance while CSF (cerebrospinal fluid) is a good conductor and most of the current flows in it [4,5]. If ISS directly stimulate soma or dendritic compartments of the cells, epidural electrical stimulation, EES, cannot induce direct excitation. However, if the pulses are repeated, the probability of stimulating long myelinated fibres increases and excitation occurs. Computational modelling helps in the prediction and analysis of electrical stimulation performed onto different regions and with different parameters[5–7]. It supports the hypothesis that fibres of the dorsal root that are large and highly myelinated are generally activated first, while higher amplitude stimulations are needed for the activation of smaller and less myelinated fibres. As a cascade effect, reflex mono or polysynaptic circuits are activated. Specific afferent fibres innervate proprioceptors (related to the sense of position in space) and mechanoreceptors. The cascade triggers ventral motoneurons (MNs). Action potentials (APs) propagate toward the effector muscle and, when lumbosacral EES is performed, three electromyography (EMG) signals are generated: i) early response (ER, 3-5 ms), ii) medium response (MR, 5-9 ms) and iii) late response (LR, 9-15 ms). For the activation of the different signals, different fibres have to be stimulated and different amplitude stimulation thresholds are set[8].

In **Figure 1** and its caption, the localization of the fibres involved in the stimulation of hind limb muscles like Gastrocnemius Medialis (GM, extensor) and Tibialis Anterior (TA, flexor) is given. For a precise description of the cascade effect of polysynaptic circuit activation, reading of Capogrosso and co-workers paper is recommended[5]. If the amplitude

of the stimuli is high, current penetrates the parenchyma and stimulate the dorsal and dorsolateral columns. Current penetration, which is estimated being modest, activates descending projections and local dorsal spinal interneuronal circuits. The activation of motor afferents varies on the rostro-caudal positioning and higher current density is generally required when the stimulation is performed in the rostral segments of the SC with respect to the stimulation of the caudal segments. This observation is reasonable since it is supposed to exist a distance effect that reduces the efficacy of stimulation when the distance between the electrode and the ventral roots is reduced due to anatomical caudal SC thinning. Specific effects on the stimulated muscles are also position dependant[9,10]. The EES applied rostral activates specifically the TA flexor muscle with respect the more collective activation of several fibres due to caudal stimulation. Different frequencies also induce different effects[11–13] from vibratory movements to stepping. Over-excitation induces strong non-controlled shaking.

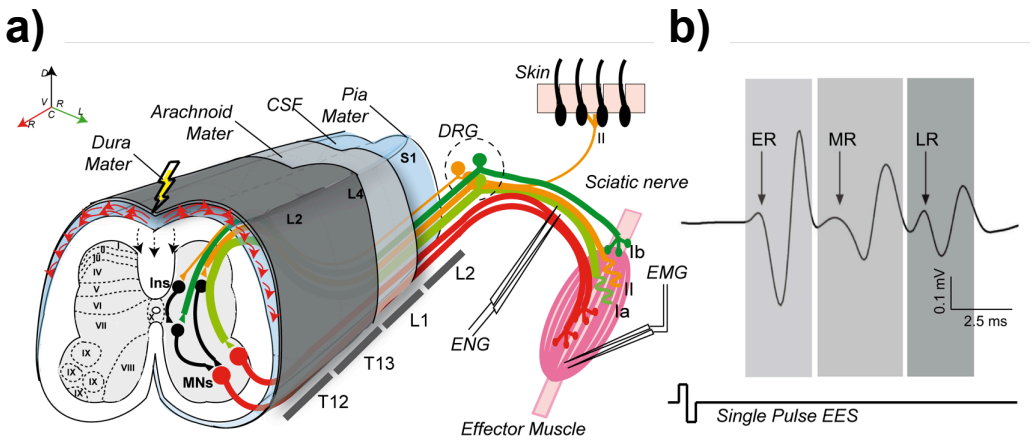

Group I (Aα): Ia and Ib, large, myelinated. **Proprioception.** Muscle spindle (Ia) and Golgi tendon organ (Ib).
Group II (Aβ): medium, myelinated. **Proprioception and mechanical pressure**.
Group III (Aδ): small, myelinated. **Pain**.
Group IV (C): small, unmelyenated. **Pain**.

Figure 1 a) illustrates the fibres involved in EES that innervate the different receptors. Red and black arrows indicate the current propagation in the CSF and in the parenchyma. ENG is performed using hooks positioned around the sciatic nerve (SN) while two electrodes in the Gastrocnemius Medialis, GM and Tibialis Anterior, TA serve the EMG recording. **b)** Representative EMG recording of

EES performed with a single pulse. Different time responses are reported. This figure is also reported in M. Donegà's PhD thesis.

In Chapter 4 I commented about the huge amount of different stimulation protocols that could be used *in vitro* and it is clear how *in vivo* the range is even expanded. In fact, the variable of the positioning of ES opens to a myriad of different protocols. However, choice is simplified since ventral EES is more appropriate in electrically enabled motor control (eEMC) while ISS onto the ventral horn is more appropriate for the functional ES (FES) and other less common configurations are also not recommended and have to be excluded. Since the aim of the i-ONE project is the promotion of plasticity of intraspinal circuits, the dorsal epidural or subdural stimulation is the most promising approach. However, precise indications of the effects towards SC increasing plasticity after injury are currently not available.

The implant described in Chapter 6, specifically designed for interfacing the spinal cord, fulfills several requirements both regarding the structural properties and about the functionality. In collaboration with the group of S. Pluchino, MD at University of Cambridge, AMID is tested. The functionality, both in healthy and injured anaesthetized adult mice and rats, is evaluated by changing stimulation position, amplitude and frequency. *In vivo* acute electrophysiology, a universally accepted method, is used to evaluate the stimuli efficacy. AMID activity is investigated at different time points after the injury. Device, at first stage, is placed onto the SC at the very moment of the stimulation. This excludes increasing of electrodes impedance due to foreign body reaction that could occur if AMID are implanted. Doing so, possible changing in the ES thresholds can be univocally ascribed to changes in the physiological response to the stimuli and one can exclude effects of affected device functionality. The last requires dedicated experiments to be tested over

the time of implantation that are not performed yet. Once thresholds are identified, one hour ES is applied below the injury level in order to evaluate the effects in acute and elucidate possible effects onto the biochemical tissue composition.

7.1.1 Stimulation of the Rat SC in Acute, Experimental Section

Toward the successful chronic implantation of the AMID, the demonstration of its efficacy in stimulating the SC in acute *in vivo* is a necessary step. Experiments are performed both on mice and on rats and the results are comparable. In this thesis most of the results are obtained on rats. Rat, on which we started to work later, is the preferred animal model. Indeed, rat electrophysiology is better known and bigger dimension reduces the device miniaturization requirements, facilitates AMID manipulation and allows an easier implantation protocol. The rat model is the C57BL/6 and animal experiments are performed at the University of Cambridge accordingly to the principles of laboratory animal care approved by the UK Office animals (scientific procedures) act 1986, under the Project license 80/2457 granted to Dr. S. Pluchino.

T11-L3 laminectomy to expose the lumbosacral segments (T13-S3) follows terminal anaesthesia. The proximal portion of the sciatic nerve (SN or Sn) of the hind limb is also exposed and the hooks for the electroneurography (ENG) are connected. Electromyography (EMG) requires bipolar electrodes inserted into the TA and GM muscles.

ES is performed through the AMID using the electrodes couple 1/5 or 8/5. The first approach is based on single pulse ES at increasing intensity. The upper threshold is identified with a muscle twitching. The device positioning is performed in order to obtain a stimulation of the SC at L4-L5 (T13 vertebral level). The ENG and EMG traces (**Figure 2a** and **b**) show a highly reproducible physiological response to five single stimuli

delivered through the AMID. The ENG compound is composed of a short latency response (slR) and a medium latency response (mlR) of respectively 2 ms and 6 ms. When stimuli repetition is performed, the ENG traces change. At frequency higher than 10 Hz, the mlR is inhibited and disappears after the very first 2 stimuli. This is a typical physiological response and the usage of frequency dependant stimulation is helpful in the identification of specific receptors involved. The most important information is that is highly probable motor pools are involved. It this thesis, no further details are given; for further discussions refer to M. Donegà's thesis.

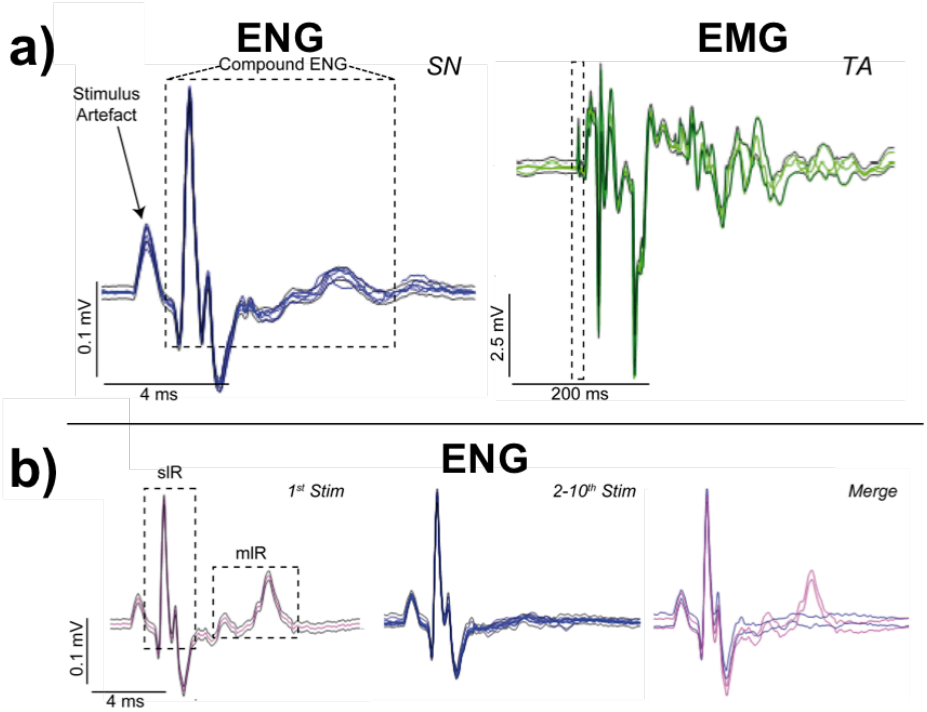

Figure 2 a) reports 5 overlapped ENG (SN) and EMG (TA) signals resulting from independent single pulses of EES applied with AMID. Grey lines mark the limits within the responses occur. The dashed frame on the left draws attention to the full ENG compound. On the right (EMG of TA), the dashed frame indicates the interval time within the early, medium and late responses (ER, MR and LR) occur. **b)** Typical ENG signals resulting from the multiple stimulations experiment at frequency higher than 10 Hz. On the left the response to the first stimulus is

reported while on the middle are reported the signals recorded after the second stimuli. On the right the superposition of the traces show the inhibition of the mIR at higher frequency where the sIR only survives.

In order to determine the optimal device localization and the specific current threshold needed to activate SC circuits, further experiments are performed. Injected current densities ranges from $7.5*10^{-4}$ μA/μm^2 to $2.0*10^{-2}$ μA/μm^2 and the stimulation is performed at different levels along the rostro-caudal axis.

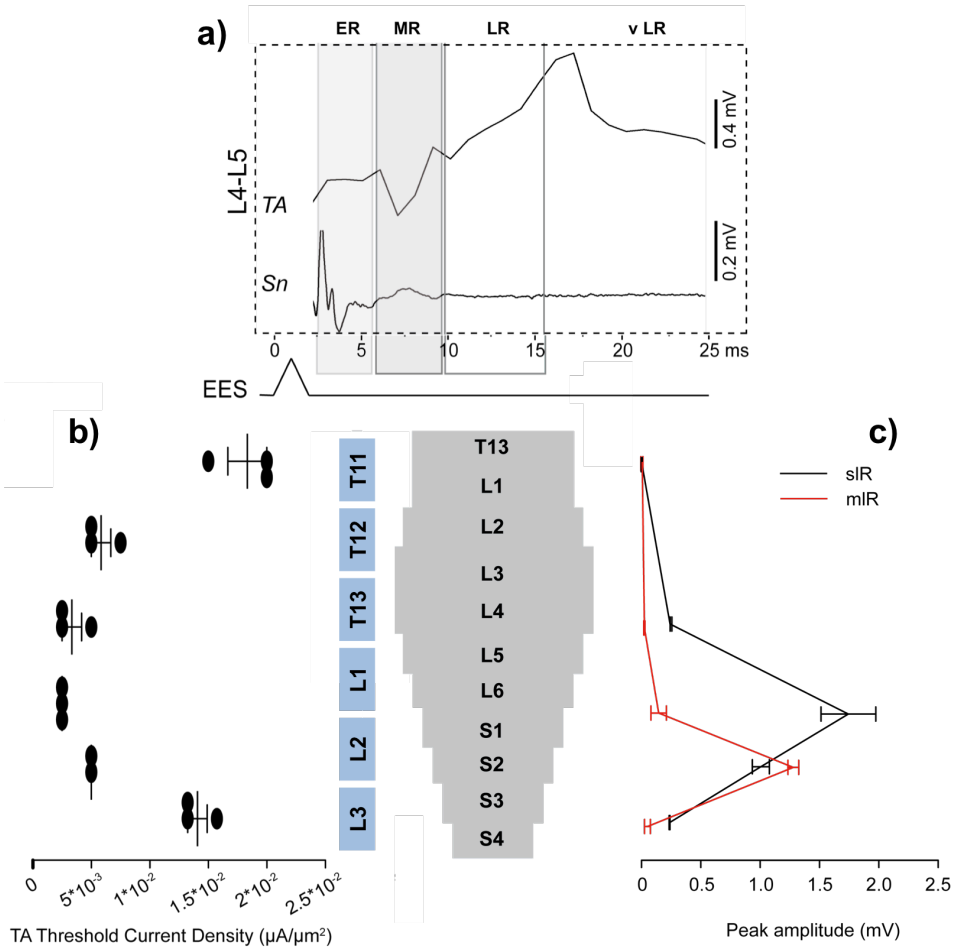

Figure 3 a) Representative traces of EMG from TA and ENG from the Sn stimulated with EES by means of AMID at 1 Hz at the level L4-L5 (putative localization of TA motoneurons). **b)** reports a graph that shows the average current density necessary to induce a TA twitching stimulating with a single pulse at different levels (that are indicated by the picture in the middle). **c)** ENG signals

amplitude from the Sn resulting from the stimulation with a single pulse at injecting current density of $7.5*10^{-3}$ $\mu A/\mu m^2$ at different SC levels. Both the slR and mlR peak amplitude are reported. Figures also reported in M. Donegà PhD thesis.

As expected, the effect onto the typical time dependent EMG signals varies on the stimulating electrode positioning. Typical EMG and ENG responses to stimuli applied at L4-L5 level are reported in **Figure 3a**. In **Figure 3b** are reported the thresholds, identified in terms of minimum current needed to induce muscular twitching, along the rostro-caudal axis. In the same figure, amplitudes of the relevant peaks in the ENG compound are reported (**Figure 3c**).

The stimulation effects are very position dependant. Lowest current density in order to induce hind limb muscle twitching is needed when stimulating within L3-S2 segments. Moving to more caudal segments increases the entity of the induced tail movements. Stimulating in the portion L3-S2 at different frequencies also generates different responses. If the frequency is lower than 20 Hz the stimulation induces vibratory movements in the hind limb while a full contraction is induced at frequencies up to 50 Hz. The current densities thresholds to obtain complete muscle contraction are not significantly frequency dependant.

Same stimulation experiments in acute are performed also on SC injured animal model. Even if recently the experiments are performed onto rats, the results in this thesis are from the preliminary series and are obtained with C57BL/6 mice. Stimulations effects onto rats and mice in the same conditions are comparable. Muscle twitching is induced with similar current but slightly lower threshold and slR and mlR are well resolved in the ENG compound. Evaluating the response peaks and relative timing (not shown in this thesis) one can demonstrate the circuits activated during the single and multiple pulses to the lumbar SC of anesthetized healthy rats and mice are the same. This demonstrates the reliability of

the comparison. The main difference is about the speed of the response, which is a bit shorter for mouse with respect rat due to smaller dimension.

The series of experiments onto injured SC are important to determine: i) the current threshold needed to efficiently stimulate the SC after injury and ii) the molecular effect of one-hour stimulation below the injury level.

A dorsal contusion induced at T12 vertebral level (L2-L3 SC segment) is the necessary step for having a reliable SCI animal model. It causes an incomplete lesion to the SC that results in chronic impairment of fine locomotor skills (i.e. paw placement and angle, toe clearance and mobility and tail position). The evaluation of the locomotors behaviour (**Figure 4a**) is performed according to the Basso Mouse Scale (BMS)[14,15] onto injured mice and the score compared to sham controls represented by mice onto which laminectomy only is performed.

EES is applied below the injury, at L4-L5 level (**Figure 4b**). The stimulation is performed at different time points indicated as days post injury (dpi): 1, 3, 7 and 21. One Hz frequency is set and stimulation is performed at increasing current densities. The lower threshold ($7.5*10^{-4}$ $\mu A/\mu m^2$) is identified as the amount of current density needed to elicit ENG compound in the sham control at the same L4-L5 level. In **Figure 4c** one can note the trend in the current density needed to elicit the ENG compound that increases up to 7 dpi and decreases at 21 dpi.

Then, one-hour stimulation is applied with an injected current density three times higher respect the thresholds for the activation of ENG compound but lower than the one needed for the activation of motor axon identified with EMG. The choice of a modest current injection density is supported by the fact that molecular changes are supposed to occur rapidly and the usage of strong perturbation is not needed. The stimulation protocol is the one already set for *in vitro* experiments onto neurons and macrophages that is: bipolar pulses at 20 Hz for five seconds repeated for a total of 40 times with a rest of about one minute between

the bursts. The AMID is positioned with active electrodes onto the L4-L5 segment of the SC. The RNA extraction, RT and Taqman qPCR are performed onto the SC segments. Fos and Jun are two early genes known to result upregulated upon activation of VGCCs during neuronal activity and also via activation of glutamate receptors. It is supposed that EES activates neuronal depolarization and activation of SC circuits. Therefore it is reasonable to suppose an upregulation of the early genes mentioned upon AMID operation.

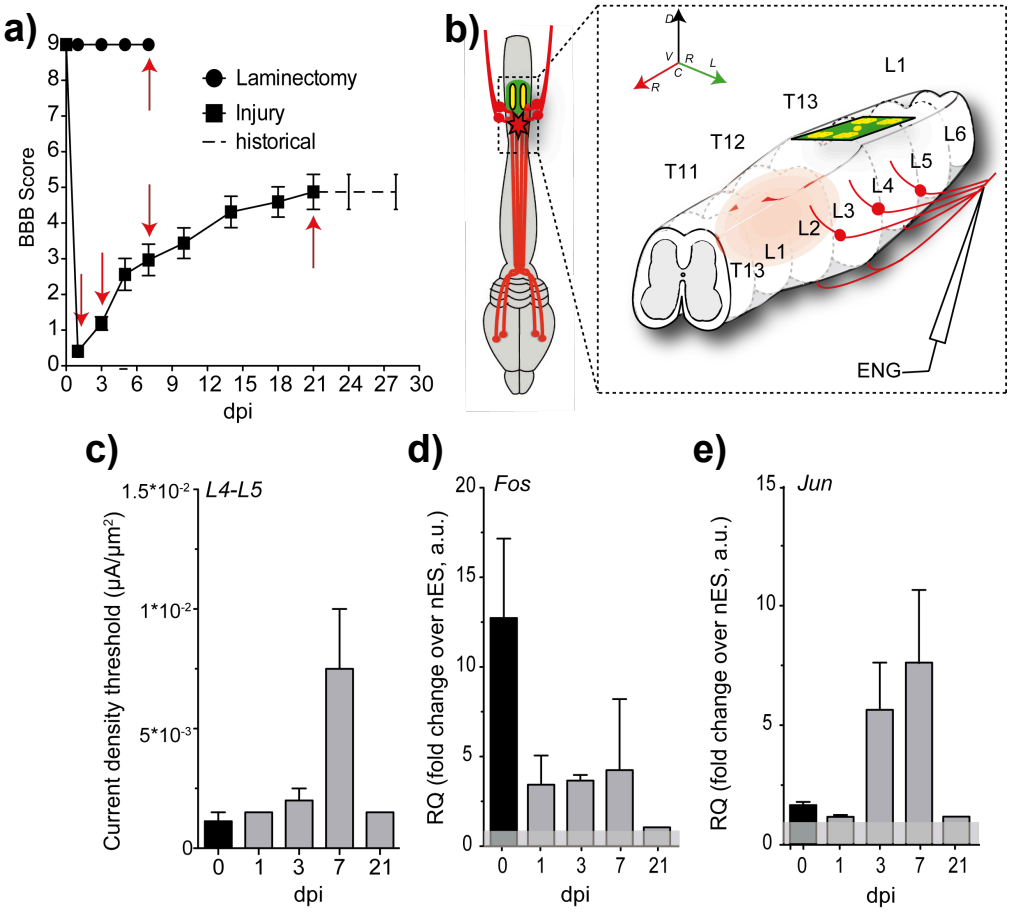

Figure 4 a) Basso Mouse Scale evaluating the locomotor abilities of mice (control and SCI) along the 21 days of follow up. The red arrows indicate the dpi of the electrophysiological experiments. **b)** Picture that shows the placement of the device at L4-L5 level that is more caudal with respect the injury (pale red area at L2-L3). **c)** Injected current density needed to induce a recordable ENG compound at different dpi. The graphs in **d)** and **e)** are representative of the

mRNA expression of Fos and Jun quantified by Taqman qPCR and expressed as fold change over the non-ES control.

Fos in L4-L5 segment is upregulated at all the time points but not at 21 dpi. It worth to be noted that the upregulation of Fos in stimulated control mice is higher then in stimulated injured mice. Jun gene is upregulated at 3 and 7 dpi only. In the **Figure 4d** and **e** the Fos and Jun upregulation is plotted. Other investigations are still under evaluation and the results are not ready to be presented.

7.1.2 Conclusions Part I

Biodegradable and biocompatible AMID is demonstrated capable to efficiently stimulate the SC. EES is applied along the various segments of the SC of anesthetized healthy rats and mice. The recording for the evaluation of the stimulation capability is done with *in vivo* electrophysiology (i.e. ENG and EMG). From the analysis of the responses, obtained at different frequencies, injected current densities and electrodes positioning, is possible to hypothesize that motor-evoked responses (i.e. vibration and contraction of hind limb and movement of the tail) are at least partially due to direct activation of motor axons. A clear dependence of the rostro-caudal ES position onto the specific activation of fibers suggests the importance of designing specific electrodes pattern and performing appropriate surgical AMID placement. The high excitability of the segments L4-S2 in healthy rat, already observed[12,13], is confirmed.

Importantly, the efficacy of EES through AMID is demonstrated onto mouse SCI model. The device is capable of stimulating afferent and efferent fibers above and below the injury level (L2-L3). Differences in the current threshold (i.e. lower for SCI mouse than for healthy rat) can be ascribed to the different animal dimensions. In order to verify possibility of promoting activity-dependent plasticity mechanisms, one-hour stimulation below the injury level (where lower current densities are needed) is

performed. The analysis of molecular changes within the stimulated segment at different time points shows that one hour of ES is enough to promote significant changes in two genes involved in the activation of VGCCs. This can be ascribed either to direct or indirect mechanisms that involve respectively the activation of propriospinal neurons or specific afferent fibers. The former preliminary results are interesting and demonstrate the positive outcome AMID could provide. However, the results we collected are partial and longer investigation in acute and in chronic on awake mouse/rat are necessary in order to demonstrate the efficacy of AMID in the treatment of the SCI.

Other ongoing investigations are related to the possible activation of pro-inflammatory early genes that could provide interesting data about the down regulation observed by us *in vitro*.

7.2 *In vivo* Subacute AMID Integration: an Introduction

Prior to test the therapeutic chronic efficacy of ES, other preliminary studies have to be performed. As already discussed in the Section2.6, AMID biointegration has to be demonstrated since device interfacing to SC can result detrimental both to the device and to the tissue and can cause failure of the overall therapy. Even if materials choice should guarantee safety and should prevent FBR, other factors could generate adverse molecular cascade. As discussed in the Chapter 1, G. Courtine, S. Lacour and co-workers developed the implantable PDMS-based *e-dura* device, which stimulates safety the SC[16]. They shown, on the contrary, a very similar device made of polyimide causes severe chronic FBR and induces compression and mechanical deformation of the SC that result in locomotors dysfunction in healthy rats[16]. The main difference between the two devices, that are both considered made of biocompatible material, stands on the flexibility, which the second misses. This demonstrates how *in vivo* evaluation is a necessary step since even if materials seem to fulfil all the requirements implant failure can occur.

In order to verify absence of inflammation and of chronic pain induced by the simple presence of the device, AMID implantation and medium term monitoring of mouse behavioural and electrophysiological activity is performed. This followed safety studies performed in collaboration between members of the i-ONE consortium to evaluate the FBR of MPs to PLGA *in vitro* and the possibility of reducing it by means of minocycline (a broad-spectrum antibiotic). For sake of brevity, I only report the main findings of *in vitro* research in the conclusions while I stress more about implantation protocol and biointegration results that I contributed to develop also by properly designing and shaping the device.

7.2.1 Subacute AMID Implantation on Rats, Experimental Section

The overall experiment for the investigation of the *in vivo* FBR induced by the AMID is characterized by different time points. Fully trained operators perform these experiments at the University of Cambridge. The parameters used to evaluate the behaviour of rats up to 28 dpi (days post implant) are the gross locomotors capability, gait parameters, fine locomotors skills and mechanical sensitivity. Proper tests are described in detail in literature and confidentially used by our collaborators. Rats are trained for 14 days prior the implant and behavioural tests are performed. Rats subjected to surgery without implantation represent the sham control. Electrophysiological tests are performed onto half of the group with implanted AMID (i.e. four rats) in order to evaluate muscular response to the external stimuli while the other half is sacrificed at 7 dpi in order to perform tissue-pathological analysis. Electrophysiological tests are performed by means of EMG electrodes implanted into the TA and GM of the hind limb.

Surgical procedure is well described by M. Donegà whom practiced it together with Dr. E. Giusto. While most of the implantable devices for SCI treatment are positioned above the dura mater, G. Courtine and S.

Lacour pioneered the sub-dura implantation. Starting from what they reported and adapting the device fabrication and final shape to optimize the implantation procedure, AMID is implanted below the dura. With respect a standard epidural implantation, this procedure is longer and more complicated but the AMID is in intimate contact with the targeted neural tissue. It allows i) lower current densities to be injected to achieve ES, ii) it enables an easier signal recording as well as iii) a more efficient drug delivery. The procedure is reported in **Figure 5**.

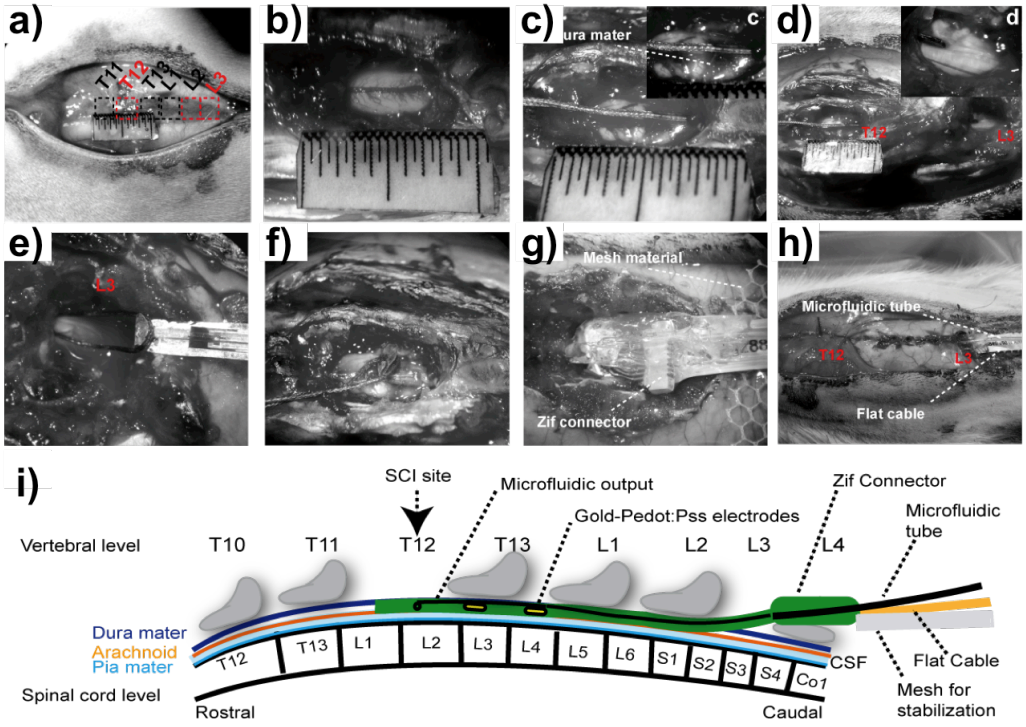

Figure 5 a-h) report the principal steps of the implantation surgery of an AMID onto a rat. **a)** and **b)** are pictures of the selection and exposition of the SC segments at T12 level. In **c)** and **d)** the dura mater is cut and a suture wire is inserted below and pushed till the L2 laminectomy site where a second aperture on the dura is performed. The reference meter has a total length of 1 cm. **e)** and **f)** are pictures of the device insertion from the hooking of the device with the suture wire loop at L2 level to the positioning underneath the dura mater. **g)** is a detail of the ZIF connector and microfluidic inlet tube coming out at L3-L4 levels and flat cable sutured to the lower back muscles. **h)** Tissues sutured. **i)** shows

the positioning of the AMID underneath the dura mater. Figure also reported in the PhD thesis of M. Donegà.

A double laminectomy at vertebral level T12 and L3 is performed in order to expose the dura mater. With a ruse the device is inserted and finely positioned underneath the dura. Thanks to AMID dimensionality, if the active devices interface the L2 segment of the SC, the small connector can be placed in the space created by removing the L4 spine process. The overall device results firmly positioned. The flat cable and the microfluidic outlet run above the vertebral bones towards the head where a printed connector (useful for ES and recording) is sealed.

After the anaesthesia, all the rats (both sham control and AMID implanted) recover quickly and are able to move without apparent deficits. General welfare is high for the all 28 days following the implants. This demonstrates the surgery is well tolerated. Surprisingly, the behavioural tests did not show any significant difference between the two groups of rats and between pre and post-surgery parameters, for the whole time of the follow-up. Last, the analysis of the locomotors skills and EMG were performed and again no differences were observed. SC compression, possibly induced by the AMID, could alter the mechanical pain threshold. The last is the parameter used to evaluate if it is the case. Even if all the rats from the two groups show significant differences respect pre-surgical values, no differences between the two groups are observed.

AMID biocompatibility is still under evaluation at two time points: 7 and 28 dpi. The SC is explanted and sectioned in order to monitor the FBR elicited by the implanted device. Cell adhesion and mechanical disruption of the cord represent the main evaluating parameters. The AMID positioning and degradation are also relevant information. No mechanical deformation of the SC of AMID implanted rats is found and the device always resulted well positioned. Above and below the device surface even at 28 dpi, a layer of matrix deposition was not found.

Collected pictures of the extracted cord at 7 dpi show the AMID implanted below the dura mater. AMID opacity and the tissue layer preclude a full visualization of the active layers. After 28 days of implant, some cracks appear on the AMID backside. AMID operational stability along the implantation is not performed yet.

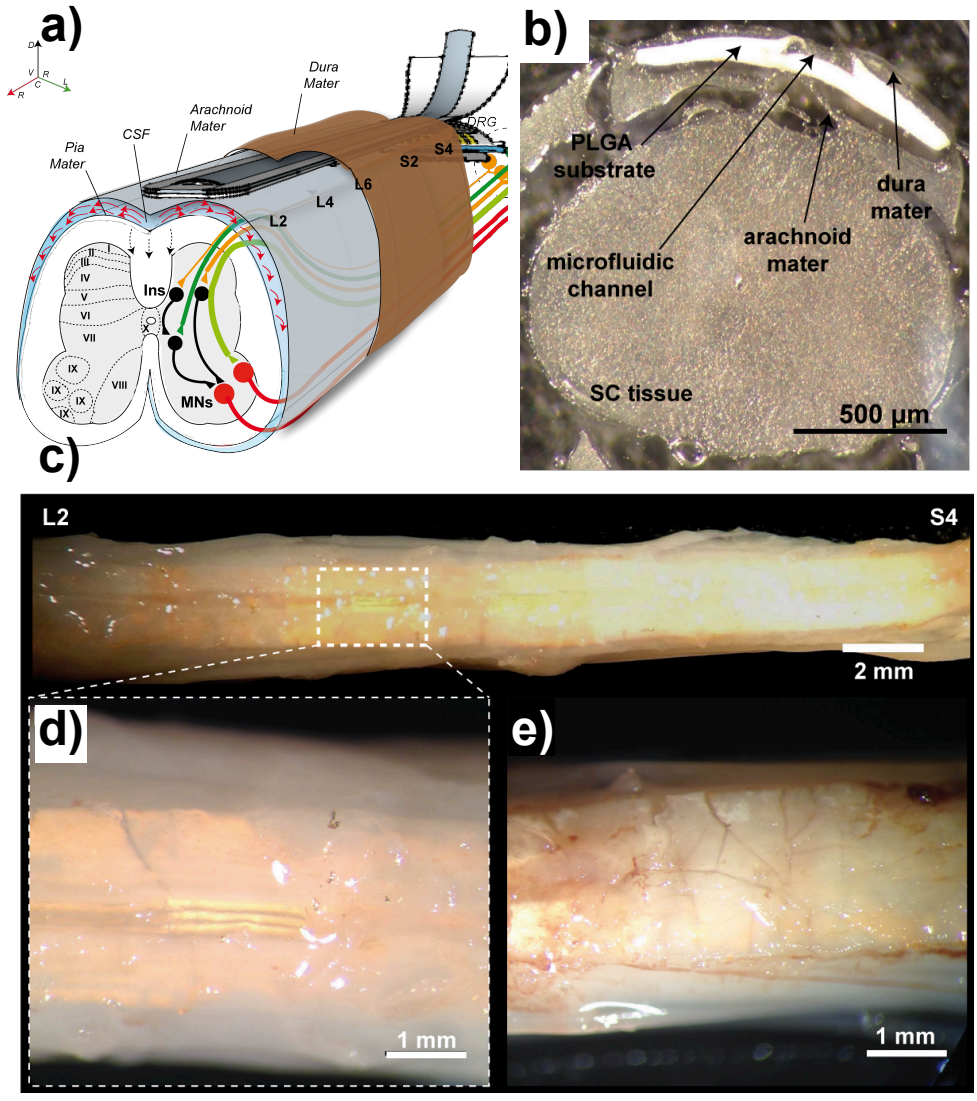

Figure 6 a) A scheme representing the AMID implantation below the dura along the L2-S4 with active devices interfacing the L4 segment is reported. **b)** It is a picture of the cross-section of the 28 dpi explanted SC with AMID well positioned between the arachnoid mater and dura mater. It is possible to note the SC anatomy is preserved. **c)** and **d)** report different magnification of an explanted SC after 7 dpi. **e)** reports detail of an AMID after 28 dpi. Device is opaque and

cracks appeared on the AMID back. Figure also reported in the PhD Thesis of M. Donegà.

7.2.2 Conclusions Part II

First round of tests about AMID implantation provided interesting outcomes. It is demonstrated that the AMID implantation procedure is safe and doesn't not induce significant behavioural changes. Furthermore, AMID doesn't compromise fine locomotors skills. This demonstrates its physical characteristics are safe. Long-term compression of the SC, as observed by Minev et al. with PI based implants, is not induced by AMID. PI and PLGA have similar physical properties and the strong differences in the induced SC compression can be variously explained. The alternative implantation surgery could better allow device adaptation thus contributing to reduce local stresses. Another explanation can be found in the different long-term material properties. Indeed PLGA Young's modulus decreases of few orders of magnitude within the first 14 days of immersion in cell culture medium, meaning PLGA softens with time[17]. Last, the cracks found on the devices back after 28 dpi could be associated with a reduced pressure on the tissue and higher device conformability onto the SC. The fractures have to be investigated in order to assess AMID integrity and its functionality upon time. This is a scheduled experiment that will be associated with the investigation of *in vivo* chronic ES. Evident fibrosis layers were not found onto the explanted AMIDs. However, tissue pathological analyses are needed in order to assess the real *in vivo* FBR. A pro-inflammatory activation of MPs cultured onto PLGA was observed *in vitro* with experiments performed by I-One consortium members. Cell adhesion and pro-inflammatory activation reduced by minocycline administration are encouraging results. If a pro-inflammatory activation is associated to AMID, administration by means of microfluidic system is highly promising as strategy to reduce FBR.

Bibliography

(1) Lavrov, I.; Musienko, P. E.; Selionov, V. A.; Zdunowski, S.; Roy, R. R.; Reggie Edgerton, V.; Gerasimenko, Y. Activation of Spinal Locomotor Circuits in the Decerebrated Cat by Spinal Epidural And/or Intraspinal Electrical Stimulation. *Brain Res.* **2015**, *1600*, 84–92.

(2) Guevremont, L.; Renzi, C. G.; Norton, J. A.; Kowalczewski, J.; Saigal, R.; Mushahwar, V. K. Locomotor-Related Networks in the Lumbosacral Enlargement of the Adult Spinal Cat: Activation through Intraspinal Microstimulation. *IEEE Trans. Neural Syst. Rehabil. Eng* **2006**, *14*, 266–272.

(3) Barthélemy, D.; Leblond, H.; Rossignol, S. Characteristics and Mechanisms of Locomotion Induced by Intraspinal Microstimulation and Dorsal Root Stimulation in Spinal Cats. *J. Neurophysiol.* **2007**, *97*, 1986–2000.

(4) Struijk, J. J.; Holsheimer, J.; Barolat, G.; He, J.; Boom, H. B. K. Paresthesia Thresholds in Spinal Cord Stimulation: A Comparison Of\ntheoretical Results with Clinical Data. *IEEE Trans. Rehabil. Eng.* **1993**, *1*, 101–108.

(5) Capogrosso, M.; Wenger, N.; Raspopovic, S.; Musienko, P.; Beauparlant, J.; Bassi Luciani, L.; Courtine, G.; Micera, S. A Computational Model for Epidural Electrical Stimulation of Spinal Sensorimotor Circuits. *J. Neurosci.* **2013**, *33*, 19326–19340.

(6) Rattay, F.; Minassian, K.; Dimitrijevic, M. Epidural Electrical Stimulation of Posterior Structures of the Human Lumbosacral Cord: 2. Quantitative Analysis by Computer Modeling. *Spinal Cord* **2000**, *38*, 473–489.

(7) Holsheimer, J. Which Neuronal Elements Are Activated Directly by Spinal Cord Stimulation. *Neuromodulation* **2002**, *5*, 25–31.

(8) Lavrov, I.; Dy, C.; Fong, A.; Gerasimenko, Y.; Courtine, G.; Zhong, H.; Roy, R.; Edgerton, V. R. Epidural Stimulation Induced Modulation of Spinal Locomotor Networks in Adult Spinal Rats. *J. Neurosci.* **2008**, *28*, 6022–6029.

(9) Holsheimer, J.; Barolat, G.; Struijk, J. J.; He, J. Significance of the Spinal Cord Position in Spinal Cord Stimulation. *Acta Neurochir. (Wien).* **1995**, *64*, 119–124.

(10) Gerasimenko, Y. P.; Lavrov, I. A.; Courtine, G.; Ichiyama, R. M.; Dy, C. J.; Zhong, H.; Roy, R. R.; Edgerton, V. R. Spinal Cord Reflexes Induced by Epidural Spinal Cord Stimulation in Normal Awake Rats. *J. Neurosci. Methods* **2006**, *157*, 253–263.

(11) Ichiyama, R. M.; Gerasimenko, Y. P.; Zhong, H.; Roy, R. R.; Edgerton, V. R. Hindlimb Stepping Movements in Complete Spinal Rats Induced by Epidural Spinal Cord Stimulation. *Neurosci. Lett.* **2005**, *383*, 339–344.

(12) Lavrov, I.; Gerasimenko, Y. P.; Ichiyama, R. M.; Courtine, G.; Zhong, H.; Roy, R. R.; Edgerton, V. R. Plasticity of Spinal Cord Reflexes After a Complete Transection in Adult Rats: Relationship to Stepping Ability. *J. Neurophysiol.* **2006**, *96*, 1699–1710.

(13) Gad, P.; Choe, J.; Nandra, M. S.; Zhong, H.; Roy, R. R.; Tai, Y.-C.; Edgerton, V. R. Development of a Multi-Electrode Array for Spinal Cord Epidural Stimulation to Facilitate Stepping and Standing after a Complete Spinal Cord Injury in Adult Rats. *J. Neuroeng. Rehabil.* **2013**, *10*, 1–17.

(14) Basso, D. M.; Beattie, M. S.; Bresnahan, J. C. A Sensitive and Reliable Locomotor Rating Scale for Open Field Testing in Rats. *J. Neurotrauma* **1995**, *12*, 1–21.

(15) Basso, D. M.; Fisher, L. C.; Anderson, A. J.; Jakeman, L. B. Y. N. B.; Tigue, D. M. M. C.; Popovich, P. G.; McTigue, D. M.; Popovich, P. G. Basso Mouse Scale for Locomotion Detects Differences in Recovery after Spinal Cord Injury in Five Common Mouse Strains. *J. Neurotrauma* **2006**, *23*, 635–659.

(16) Minev, I. R.; Musienko, P.; Hirsch, A.; Barraud, Q.; Milekovic, T.; Asboth, L.; Torres, R. F.; Vachicouras, N. Electronic Dura Mater for Long-Term Multimodal Neural Interfaces. *Science (80-.).* **2015**, 23–28.

(17) Dumitru, A. C.; Espinosa, F. M.; Garcia, R.; Foschi, G.; Tortorella, S.; Valle, F.; Dallavalle, M.; Zerbetto, F.; Biscarini, F. In Situ Nanomechanical Characterization of the Early Stages of Swelling and Degradation of a Biodegradable Polymer. *Nanoscale* **2015**, *7*, 5403–5410.

chapter 8

General conclusions

Neural plasticity after severe spinal cord injury (SCI) is promoted by activity stimulating treatments such as specific physiotherapeutic training, injection of pharmaceutical cues and electrical stimulation (ES). However, full or even partial recovery of neuronal functionality is difficult to be achieved in acute treatments and most of the experiments are performed implanting permanent invasive electrodes into the epidural space. Organic bioelectronics provides novel conformable and biocompatible electronic materials and employs them in innovative architectures for stimulation electrodes or devices with even more complex transduction functionalities to be exploited in neuroprostheses. Moreover, organic bioelectronics allows one to introduce bioresorbable materials and electronic devices made thereof. So-called transient neuroprostheses exploit the bioresportion as its degradation within the body after the regeneration process would make additional surgeries unnecessary.

In this thesis, an active multifunctional implantable device (AMID) is developed that is highly conformable and biodegradable while being fully biocompatible. AMID integrates a three-fold functionality crucial for future treatments of SCI: a microfluidic channel allows the precise administration of anti-inflammatory pharmaceuticals or plasticity inducing agents; patterned electrodes allow deliver electric stimuli promoting SC plasticity; organic electrochemical transistors could allow to transduce bioelectronic activity providing possible information about the regeneration status. As the design of neuroprostheses has to meet several constraints and requirements, a step-by-step approach was followed in this thesis to reach the final goal of introducing a novel platform of implantable, multifunctional implant for SCI treatments.

Firstly, a bioresorbable material, poly(lactic-co-glycolic) acid (PLGA), was chosen (among FDA approved list for implantable polymeric compounds) as scaffold. A protocol to fabricate thin films of PLGA with controlled low roughness was developed. Then, different electronic transducer architectures were screened in order to find the most adequate to be used for stimulation as well as recording of bioelectric signals, in physiological environment. The first is an electrolyte gated organic field effect transistor (EGOFET) fabricated with a strategy called laser ablation that is highly versatile and that allows patterning of thin electrodes with micrometric features on fragile bioresorbable scaffolds. The metal electrodes are part of the stimulating/sensing platform, the EGOFET, which is completed with a semiconducting material. Pentacene based EGOFETs with good electrical performances were demonstrated efficient in pure water and, upon some fabrication strategy adaptation, in physiological environment as well. Albeit performances enable extracellular sensing, pentacene-based EGOFETs on PLGA show limited stability over time. Since AMID operation has to be guaranteed for the whole time of the therapy, expected to be in the range of up to several weeks, further architectures were tested. Organic electrochemical transistors (OECTs) based on PEDOT:PSS were for the first time

fabricated on a biodegradable scaffold and performances are comparable to state of the art OECTs fabricated on glass. The potentiometric sensitivity is high and they were demonstrated efficient in the recording of a relevant bioelectric signal, the human electrocardiogram. OECTs fabricated on PLGA are highly conformable and stable upon bending. Electrical performances are stable in physiological environment for several weeks. Furthermore, PEDOT:PSS is known for its low electronic impedance at the solid/liquid interface making it an ideal candidate for the stimulation of cells and tissues. In collaboration with the group of S. Pluchino, at the University of Cambridge, *in vitro* experiments were performed in order to test the capability of eliciting action potentials (APs) on primary neurons cultured onto the device. A dedicated setup was prepared in order to combine real-time optical monitoring of calcium-ions transients with ES by means of biodegradable OECTs. Thanks to the optimized characteristics of both the device and the apparatus, demonstration of stimulating capability of our device was achieved. The usage of conducting polymers resulted, with respect bare gold electrodes, in a most efficient stimulation (i.e. less injected current density is needed in order to induce calcium transients) and safer response. The stimulation parameters were optimized in order to achieve the best neuronal response and a bipolar short pulse was found to be very efficient and safe (that means no damages for the electrodes and unaffected cell viability). The hypothesised mechanism relies on ions-induced membrane depolarization that elicits APs. Continuous stimulation for one hour induces repetitively APs within the neural population while doesn't affect the cells viability. The experimental configuration also allowed investigation of ES onto non-neuronal cells. Reactive macrophages cultured onto the biodegradable OECTs were electrically stimulated and an anti-inflammatory effect after one hour ES was observed (i.e. the transcription of pro-inflammatory genes is down-regulated). These highly relevant findings will be investigated in more detail but already suggest

possible applications of ES as alternative to pharmacological treatments in the modulation of the inflammatory response.

Once the validation of the basic functionalities of the AMID architecture was achieved in *in vitro* experiments, a strategy to fabricate implantable devices was developed. The strategy led to an AMID composed for more then 99% of its total mass of biodegradable PLGA. AMID is equipped with a microfluidic channel for the local delivery of pharmaceutical treatments and of active devices for electrical stimulation. Stimuli were applied along the dorsal aspect of the SC investigating the effect both on healthy and on SCI mice and rat models. Interestingly, the stimuli (i.e. shape, duration and current density) optimized *in vitro* onto primary neurons were demonstrated efficient to activate afferent fibers *in vivo*. This was demonstrated by stimulating anesthetized animals and performing electroneurography (ENG) and electromyography (EMG) from the sciatic nerve and hind limb muscles. These are important findings, which demonstrate AMID as promising architecture for the stimulation of neural plasticity after severe SCI. ES at lumbar level was repeated for one hour with a current threshold lower than the one necessary to induce direct activation of motor neuron. It caused repetitive neurons depolarization as demonstrated by upregulation of early genes (Fos and Jun). The hypothesis is that ES can somehow affect circuits if it is prolonged for days/weeks. Unfortunately, in this thesis results obtained in acute only are reported and no data about subacute and chronic could have been collected in terms of electrical and chemical stimulation.

However, stable subdural implantation of AMID in adult rats was achieved. Subacute effect up to 28 days was monitored and no functional impairment was observed. The explanted device after 7 days resulted transparent and apparently intact. On the contrary, after 28 days of implantation few fractures were observed. Investigation about the functionality of the device after long-term implantation and the FBR it induces are still under investigation. Stability of transistors fabricated onto

AMID needs to be increased in order to allow real time and low invasiveness monitoring of SC regeneration.

In conclusion, a novel platform for active, multifunctional, implantable devices (AMIDs) for SCI treatments based on organic electronics was developed in this thesis. Devices combine electrical stimulation and recording capabilities in the form of organic electrochemical transistors as well as microfluidics. 99% of the device total mass is bioresorbable PLGA allowing for transient neuroprostheses, which do not require additional surgeries for removal after treatment. The versatile fabrication strategy of AMID allows a fast prototyping and it can be exploited to modify electrodes shape, thickness of active and substrate material to tailor the specific therapeutic needs.

Clearly further crucial experiments are needed in order to demonstrate the therapeutic usefulness of AMID and to exploit the potentials of the combination of ES and drugs delivery. Detailed investigation of the AMID *in vivo* lifetime and its degradation will also be necessary.

Full list of publications

Peer reviewed:

1. *Title*: “Multiscale Sensing of Antibody - Antigen Interactions by Organic Transistors and Single-Molecule Force Spectroscopy”
   Authors: S. Casalini, Authors: A. C. Dumitru, F. Leonardi, C. A. Bortolotti, E. T. Herruzo, A. Campana, R. F. de Oliveira, T. Cramer, R. Garcia and F. Biscarini
   Journal: ACS Nano, 2015, 26; 9(5):5051-62
2. *T*itle: “Electrocardiographic Recording with Conformable Organic Electrochemical Transistor Fabricated on Resorbable Bioscaffold”
   Authors: A. Campana, T. Cramer, D. T. Simon, M. Berggren and F. Biscarini
   Journal: Advanced Materials, 26 (23), 3874-3878, 2014
3. *Title*: “Water-Gated Organic Field Effect Transistors – Opportunities for Biochemical Sensing and Extracellular Signal Transduction”
   Authors: T Cramer, A. Campana, F. Leonardi, S. Casalini, A. Kyndiah, M. Murgia and F. Biscarini
   Journal: Journal of Materials Chemistry B, 2013,1, 3728-3741
4. *Title*: “Facile maskless fabrication of organic field effect transistors on biodegradable substrates”
   Authors: A. Campana, T. Cramer, P. Greco, G. Foschi, M. Murgia and F. Biscarini;
   Journal: Applyed Physics Letters, 103, 073302, 2013
5. *Title*: “Sensitization of Nanocrystalline TiO_2 with Multibranched Organic Dyes and Co(III)/(II) Mediators: Strategies to Improve Charge Collection Efficiency”
   Authors: M. Mba, M. D’Acunzo, P. Salice, T. Carofiglio, M. Maggini, S. Caramori, A. Campana, A. Aliprandi, R. Argazzi, S. Carli, and C. A. Bignozzi
   Journal: Journal of Physical Chemistry C, 2013, 117 (39), 19885-96

Non-Peer reviewed:

1. *Title*: “Organic Electronics”
   Authors: F. Biscarini, M. Berto, A. Campana, M. Di Lauro
   Where: Enciclopedia italiana di scienze, lettere ed arti - IX Appendice, 2 vol, Istituto della Enciclopedia Italiana, Roma 2015. (ISBN 978-88-12-00557-4)
2. *Title*: “Bio-sensing based on Electrochemically-Gated Organic Field-Effect Transistors”

Authors: S. Casalini, F. Leonardi, T.Cramer, A. Campana and F. Biscarini,
Journal: La Chimica e L'industria, Giu/Lug, pag 78, 2013

Manuscripts in preparation:

1. pH-response of pentacene Electrolyte-Gated Organic Field Effect Transistor on quartz
2. Highly efficient stimulation of central nervous system neurons via implantable degradable organic electrochemical transistors
3. Inhibition of inflammatory innate responses via electrical stimulation

Acknowledgements

Quest'ultima tesi, non tanto per i contenuti quanto perché racconta tre anni di vita, merita dei ringraziamenti.

Ringrazio il Prof. Biscarini perché mi ha permesso di svolgere la tesi su un progetto stimolante ed ambizioso. Lo ringrazio soprattutto perché ha creduto in me molto più di quanto non lo abbia mai fatto io stessa.

Ringrazio Tobias perché è stato una grande guida. Mi ha insegnato tanto, dato fiducia e costante supporto. Grazie per la pazienza dimostrata.

Ringrazio Mauro perché mi ha insegnato a saldare e usare macchine da vuoto. Lo ringrazio anche perché ha apprezzato il mio approccio alla Mc Gyver senza deriderlo troppo.

A dirla tutta, avere avuto voi tre come supervisori non ha fatto troppo bene alla mia autostima.

Cristiano, Francesco, Massimiliano, Denis, Marco e anche un po' Eugenio: ciascuno di voi, per ragioni diverse, è stato importante.

Ai ragazzi tutti: intanto vi dico un grazie collettivo per le tante risate e per i bei momenti trascorsi assieme in lab, al parco o al pub.

Adri e Sil, si è tanto parlato di Wall-e in questi anni. Spero che l'amicizia che ci lega, nonostante la distanza, sia forte e duratura.

Fra, Giu e Mari, il chicken corner non si ossida. Non avete mai rifiutato una richiesta d'aiuto e ve ne sono molto grata. Siete delle persone fantastiche.

Casolo, grazie per l'aiuto e per il sostegno continuo.

Rafa, Michi, Marc, Chiodo e Barto: manzi! La vostra presenza ha mediato l'eccesso di estrogeni e rallegrato le giornate in laboratorio. Essenziali.

Ringrazio la grande famiglia i-ONE ed in particolare Matteo Donegà al quale auguro il meglio del meglio sia nella vita sia nel lavoro.

Alex: non sono una buona guida e mi spiace. Sappi che ho fatto del mio meglio (pensa un po'!).

Luca e Alessandro: grazie amici. Altri 10 cammini di Santiago, altri 100 compleanni di Ianiro festeggiati assieme, altre 1000 serate a Sagrantino.

Giorgia: tranquilla, anche se la tesi è finita, avremo modo di continuare a raccontarci ogni sera i nostri insuccessi lavorativi.

Genitori: grazie di tutto.

Mario, sono fortunata ad averti come fratello, sei un esempio. Un grazie anche a Dina e ad entrambi per Gloria, sono certa che farete un ottimo lavoro con lei.

Ale, grazie per avermi consolato quando piangevo, ascoltato quando volevo parlare, rispettato i miei silenzi quando non volevo raccontare nulla, grazie per esserti preso cura di me ma grazie soprattutto per avere condiviso con me le tantissime gioie di questi anni.

A tutti quelli elencati: chiedo sinceramente scusa per i tanti (troppi) lamenti quotidiani. Ho condiviso con voi tanti momenti bellissimi, grandi gioie e soddisfazioni e sono questi che ricordo. Siete stati meravigliosi.

Se ho dimenticato qualcuno, chiedo scusa, non me ne vogliate.